Robot-based Autonomous Neuro-registration and Neuronavigation for Neurosurgery

By

Abhishek Kaushik

ENGG01201404017

Bhabha Atomic Research Centre, Mumbai

A thesis submitted to the

Board of Studies in Engineering Sciences

In partial fulfilment of requirements

for the Degree of

DOCTOR OF PHILOSOPHY

of

HOMI BHABHA NATIONAL INSTITUTE

August, 2020

Homi Bhabha National Institute[1]

Recommendations of the Viva Voce Committee

As members of the Viva Voce Committee, we certify that we have read the dissertation prepared by *Abhishek Kaushik* entitled *Robot-based Autonomous Neuro-registration and Neuronavigation for Neurosurgery* and recommend that it may be accepted as fulfilling the thesis requirement for the award of Degree of Doctor of Philosophy.

Viva Voce Committee	Signature	Date
Chairman –Dr.B. K. Dutta	BK Dutta	**31/08/2020**
Guide / Convener - Dr.T. A. Dwarakanath		**27/08/2020**
Co-guide - Dr.Aliasgar Moiyadi		**28/08/2020**
Examiner –Dr. Ashish Dutta		**31/08/2020**
Member - Dr. J. Chattopadhyay	J. Chattopadhyay	**31/08/2020**
Member - Dr.R.Balasubramaniam		**31/08/2020**
Member - Dr.Imran Ali Khan	Imran Khan	**31/08/2020**
Tech. Advisor- Dr.Gaurav Bhutani	Gaurav	**27/08/2020**

Final approval and acceptance of this thesis is contingent upon the candidate's submission of the final copies of the thesis to HBNI.

I/We hereby certify that I/we have read this thesis prepared under my/our direction and recommend that it may be accepted as fulfilling the thesis requirement.

Date: 31/08/2020

Place: Mumbai.

Co-guide (if applicable) **Guide**

[1] This page is to be included only for final submission after successful completion of viva voce.

STATEMENT BY AUTHOR

This dissertation has been submitted in partial fulfilment of requirements for an advanced degree at Homi Bhabha National Institute (HBNI) and is deposited in the Library to be made available to borrowers under rules of the HBNI.

Brief quotations from this dissertation are allowable without special permission, provided that accurate acknowledgement of source is made. Requests for permission for extended quotation from or reproduction of this manuscript in whole or in part may be granted by the Competent Authority of HBNI when in his or her judgment the proposed use of the material is in the interests of scholarship. In all other instances, however, permission must be obtained from the author.

Abhishek Kaushik

DECLARATION

I, hereby declare that the investigation presented in the thesis has been carried out by me. The work is original and has not been submitted earlier as a whole or in part for a degree/diploma at this or any other Institution / University.

Abhishek Kaushik

List of Publications arising from the thesis

International Journals:

1. "Autonomous neuro-registration for robot-based neurosurgery", Kaushik A, Dwarakanath TA, Bhutani G. International Journal of Computer Assisted Radiology and Surgery, Springer. 2018. 13, 1807–1817.
2. "Robot-based Autonomous Neuro-registration and Neuronavigation *: Implementation and Case studies",* Kaushik A, Dwarakanath TA, Bhutani G, Dwarakanath S. World Neurosurgery, Elsevier, 2019, Volume 134, February 2020, Pages e256-e271.
3. "Validation of high precision robot-assisted methods for intracranial applications: Preliminary study", Kaushik A, Dwarakanath TA, Bhutani G, Moiyadi A., Chaudhari P, World Neurosurgery, Elsevier, 2019, Volume 137, May 2020, Pages 71-77.
4. **"**Robust Marker Detection and High Precision Measurement for Anatomical Registration using Taguchi Method", Kaushik A, Dwarakanath TA, Bhutani G**,** International Journal of Medical Robotics and Computer Assisted Surgery, Accepted (in production), Wiley.

Peer reviewed International Conferences and Book Chapters:

1. "Image-Based Data Preparation for Robot-Based Neurosurger*y,"* Kaushik A., Dwarakanath T.A., Bhutani G., Venkata P.P.K., Moiyadi A, In: Badodkar D., Dwarakanath T. (eds) Machines, Mechanism, and Robotics. Lecture Notes in Mechanical Engineering. Springer, Singapore, 2019, https://doi.org/10.1007/978-981-10-8597-0_3
2. Optimization of Rendering Data, Generation, and Isolation of ROI for Focused Neuronavigation, Krishna R. S, Dwarakanath S., Kaushik A., Bhutani G., P. P. K. Venkata, Dwarakanath T. A., Jain R. In: Badodkar D., Dwarakanath T. (eds) Machines, Mechanism and Robotics. Lecture Notes in Mechanical Engineering. Springer, Singapore, 2019, https://doi.org/10.1007/978-981-10-8597-0_7
3. Generalized Point Correspondence Algorithm for Neuro-Registration, Dwarakanath S., Bhutani G., Venkata P.P.K., Kaushik A In: Badodkar D., Dwarakanath T. (eds) Machines, Mechanism and Robotics. Lecture Notes in Mechanical Engineering. Springer, Singapore. 2019. https://doi.org/10.1007/978-981-10-8597-0_5

4. Image based Data Preparation for Neuronavigation, **Kaushik A**., Dwarakanath T.A., Bhutani G., Venkata P.P.K., Moiyadi A, 2nd International and 17th National Conference on Machines and Mechanisms (iNaCoMM15), 2015, IIT Kanpur, India. https://www.inacomm2015.ammindia.org/img/44.pdf

Abhishek Kaushik

Dedicated to Family, Teachers, and Friends

ACKNOWLEDGMENT

I would like to express my deepest gratitude to my supervisor **Dr. T. A. Dwarakanath,** for his valuable guidance, patience, encouragement, and the freedom given to me in carrying out research. Apart from the scientific knowledge, the discipline, which I learned from my supervisor, is indispensable to my growth as a Ph.D. student and as a person. I considered myself to be honored and fortunate to be associated with him.

Besides my Ph.D. guide, I would like to thank my co-guide Dr. Aliasgar Moiyadi (Chief of neurosurgery, Tata Memorial Centre, Mumbai). I would like to thank the rest of my doctoral committee members: Chairman of the committee, Dr. B. K. Dutta and members, Dr. J Chattopadhyay, Dr. R. Balasubramaniam, and Dr. Imran Ali Khan. Their insightful comments, encouragement, and their hard questions incented me to widen my research from various perspectives. I would like to express my deep gratitude to my technical advisor Dr. Gaurav Bhutani (DRHR, BARC), for his inspirational support and valuable and practical suggestions for the research work. I would like to thank Dr. Dwarakanath Srinivas of the National Institute of Mental Health and Neurosciences, Bangalore, for allowing and supporting me to conduct the experiments at NIMHANS Bangalore.

I would like to thank Shri K. Madhusoodanan, Head, DRHR, BARC for permitting me to conduct research work at DRHR.

I would like to thank Shri. S. K. Sinha, Shri. Hemantha Swain, Shri Rahul Jain, Shri Saurabh Gupta, Shri Kamal Sharma and Shri Patil for supporting me throughout my research work.

I would like to thank my friends and fellow graduate students, Dr. Ashish S., Dr. Rahul K., Dr. Sankarrao C., Alok D., Kartik K., Amit K., Dr. Vinod B., Dr. Tribeni R., Dr. Anuj S., for the many fruitful discussions and happy memories.

It was my parents who first instilled in me the motivation for learning and their hard work has prepared me for higher education. Special thank goes to my mother Smt. Abha Kaushik and my father Shri. Ashok Kaushik. It is impossible for me to finish this thesis without their support, encouragement and sacrifice. Thanks to my brothers Shri. Tarun Kaushik and Shri. Varun Kaushik, and my dear friends for their constant support, love and care. I would like to thank my entire family for supporting emotionally throughout this journey and my life in general.

ABSTRACT

Neurosurgery is one of the highly intricate tasks. To avoid the complications associated with craniotomy (open brain surgery), neurosurgeons prefer Minimally Invasive Surgery (MIS). In MIS, the neurosurgical task can be performed through a small burr hole drilled on the skull of the patient. The robot-based neurosurgery enhances the scope of the MIS by providing better accuracy, higher repeatability, detailed internal visualization through multiple cross-sectional images, 3D patient-specific model, and real-time tracking of the surgical tool. The real-time tracking of the surgical tool with respect to the patient's skull is also referred to as neuronavigation or stereotactic surgery. The neuro-registration is a prerequisite for neuronavigation. The neuro-registration relates the physical robot space to the medical image space (virtual space) by measuring the corresponding reference points in both the spaces. The frameless neuro-registration is steadily replacing frame-based stereotactic surgery. The accuracy of overall robot-based neurosurgery depends on many factors like robot accuracy, imaging accuracy, the measurement accuracy of reference points in medical image space as well as robots' space. Majorly, the neuro-registration method and practice play a vital role in achieving high accuracy neurosurgery.

The objective of this work is to achieve autonomous, highly accurate, and faster robot-based frameless stereotactic neurosurgery. The primary objective is to eliminate human errors and enhance the accuracy and reliability of robot-based neurosurgery. Line of sight is the straight line along which camera has unobstructed vision. In wall-mounted stereocamera system, navigation stops if somebody obstruct the line of sight of stereocamera. Further, the objective is to eliminate the line of sight problem associate with the frameless stereotactic neurosurgery and achieve quick neuro-registration and time-optimal neurosurgical procedures. To serve the objectives, the design of the algorithms operating in real-time and methods robust to the

varied ambiance of the operation theatre for conducting successful autonomous neuro-registration is considered. A 6 Degree of Freedom Parallel Kinematic Mechanism (6D-PKM) based robot is used for neuro-registration, neuronavigation and neurosurgery. It can be noted that there is no separate robot for the neuro-registration. The robot comprising of three translational, and three rotational DOF can approach a point in workspace from multiple directions. Also, the platform of the robot can be positioned in multiple posture at a point in the workspace. The 6D-PKM robot is a compact portable system, weighing 150 N, and it can manipulate a payload up to 200 N. The repeatability of the robot is 10 µm, and absolute accuracy is 60 µm. The algorithms related to neuro-registration and neuronavigation are implemented in python and C++.

Multimodality imaging compatible glass jar, glass skull, and PVC skull phantoms with artificial targets and bur holes are developed. The autonomous neuro-registration is conducted on the phantoms to establish performance characteristics in terms of repeatability, accuracy, and operative time. The performance characteristics are evaluated for many combinations of the patient pose, burr hole entry point, lesion’s target point, set of registration points, surface, and deep-rooted targets, and varied operation theatre ambiance. The validation of autonomous neuro-registration is presented through several case studies. The autonomous neuro-registration is also conducted and validated on a vegetable specimen with artificial targets, to simulate the tissue and needle interaction. All the experiments are repeated several times. In all the cases, the accuracy is found to be less than 1 mm. The robustness of the algorithms is tested for real-time detection and measurement of markers under the varied ambiance of the operation theatre. The execution time depends on the surgical task. The average execution time of the autonomous neuro-registration algorithm is found to be less than 5 minutes.

The frameless robot-based neurosurgical procedure is further enhanced in terms of autonomy, accuracy, and time. The algorithms are validated through case studies of phantoms and vegetable specimens. The case studies show the high capability of accessing deep-rooted, small-sized tumor with high accuracy. The results of robust real-time fiducial marker detection algorithm prove very high consistency despite variation in marker visual property and operation theatre ambiance. The robot-based neuro-registration eliminates the line of sight problem.

CONTENTS

LIST OF FIGURES

LIST OF TABLES

CHAPTER I
Introduction

1.1 Motivation

Brain ailments may have to be often treated with surgery. Neurosurgery demands special skills in terms of insight, accuracy, alertness, and navigation control. Though humans attain these qualities, there exist complications associated with open brain surgery or craniotomy. The option to isolate the problem region from the rest and execute minimum invasion will lessen the complications. In Minimally Invasive Surgery (MIS), the surgical task can be performed through a small burr hole drilled on the skull of the patient. Less risk, minimum invasion, reduced healing time, and fewer chances of the infection are some of the benefits of the MIS. In conjunction with these advantages, MIS has some downsides like narrowing of the field of view of the surgeon and difficulty in tool handling through a burr hole. MIS often coupled with stereotactic neurosurgery, where the 3D coordinate system is utilized to locate the problem region and to navigate the surgical tool within the brain. In frame-based stereotactic neurosurgery, a physical frame is fixed to the skull of the patient prior to the scanning. Later in the image, the localization of the problem region is made with respect to the frame. In frame-based stereotactic neurosurgery, a frame is mounted on the skull of the patient. The patient has to maintain the frame from the time of scanning till the end of the surgery. Wearing and maintaining the frame for longer duration is uncomfortable to the patient. In frame-less stereotactic neurosurgery, requirement of wearing the frame is eliminated. The radio-opaque fiducial markers are attached at the scalp of the patient prior to the CT/MRI scan (medical imaging). The markers would be visible in the medical image and are used as landmarks for localizing the problem region. Localizing the problem region within the brain and image guided real-time tracking of the surgical tool with respect to the patient skull is referred to as neuronavigation. The neuro-registration is a prerequisite for neuronavigation. It relates the physical brain space to the medical image space by measuring the corresponding reference points (fiducial markers) in both the spaces. The up-gradation of stereotactic neurosurgery from frame-based to the frameless method is possible through neuro-registration.

The accuracy of frame-based stereotactic neurosurgery is high compared to the frameless method but lacks in patient comfort. Generally, the frameless system works in combination with a stereo camera. The stereo camera, mounted at the Operation Theatre (OT), continuously tracks the surgical tool by computing the location of reflective markers attached to the tool. The reflective markers should always be visible to the stereo camera to avoid the line of sight problem.

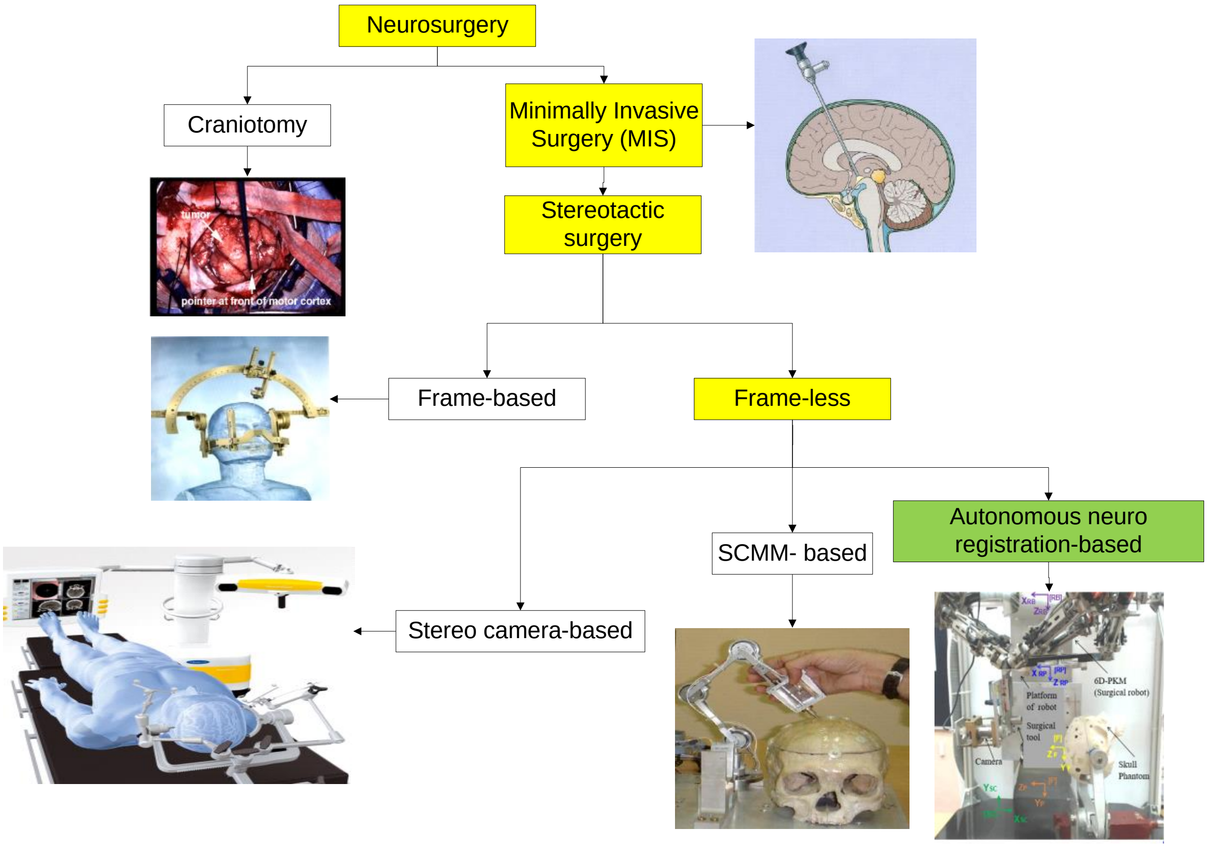

Figure 1.1: Evolution of methods in neurosurgery

The frameless robot-based neurosurgery is a stereotactic MIS. It takes care of patient comfort and enhances the possibilities of the MIS by providing detailed internal visualization through multiple cross-sectional images, 3D patient-specific model, and real-time tracking of the surgical tool. Further, it can achieve better accuracy, higher repeatability, tremor free operation, and highly focused miniature surgery. The overall accuracy of robot-based neurosurgery depends on many factors like robot accuracy, imaging accuracy, the measurement accuracy of reference points in medical image space as well as robots' space. Majorly the neuro-registration method and the practice play a vital role in achieving high accuracy in neurosurgery. Figure 1.1 shows the neurosurgery based on the techniques of localization. The motivation for the current research is to provide advantages of MIS along with enhanced accuracy, precision, patients comfort, minimal human intervention, and time optimization associated with robot-assisted surgery.

1.2 Objective of the work

The objective of this work is to minimize the manual intervention associated with the neuro-registration and to avoid human errors. Further, the objective is to develop and validate robot-based autonomous neuro-registration and neuronavigation for the neurosurgical procedure. The aim is to develop methods of autonomous neuro-registration and neuronavigation for the neurosurgical procedure, which functions in real-time and robust to the varied conditions of the OT. The overall research includes:

1. Development of algorithms to autonomously locate fiducial markers and to measure reference point at the markers in real-patient space.
2. To automate point correspondence between medical image and real-patient space.
3. To eliminate the line of sight problem associated with the frameless neuronavigation.
4. To enhance the accuracy and repeatability of neuro-registration and neuronavigation.

5. Development of real-time and robust marker detection and coordinate measurement algorithm.

6. To validate the autonomous neuro-registration by phantom and vegetable-based experiments

1.3 Organization of the thesis

The thesis is organized into 7 chapters. Figure 1.2 gives the sequence of the work. The highlight of each chapter is presented below:

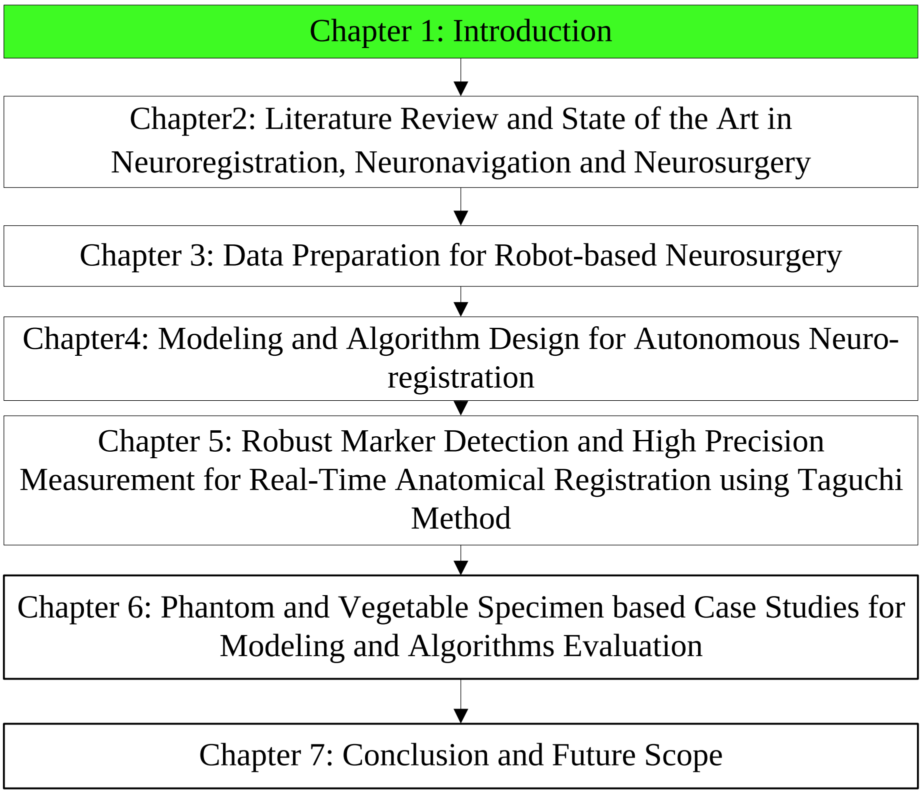

Figure 1.2: Organization of the work

Chapter 1: Introduction The ongoing chapter discuss the progression of MIS due to the risks of craniotomy and advantages of the MIS. The chapter describes stereotactic neurosurgery, neuro-registration, and neuronavigation. The advantages of the robot-based neurosurgery are stated. The sequence of procesess of robot-based neurosurgery and the sources of error associated with each process are discussed. The chapter describes the motivation behind the development of methods and algorithms related to the robot-based autonomous neuro-registration and neuronavigation for neurosurgery.

Chapter 2: Literature review and state of the art in neuro-registration, neuronavigation and neurosurgery

The evolution of stereotactic frame-based and frame-less neurosurgery has been presented. State of the art in neuro-registration, marker detection, and modern imaging modalities has been presented. The detailed application of robot-based neurosurgery is explored. The classifications of the registration errors like TRE, FRE, and FLE are discussed. The literature is reviewed for the methods to validate robot-based neurosurgery like phantoms with artificial targets, cadaver studies, vegetable experiments, and human trial runs. Advancements in practice, current research in the field of image fusion and registration is presented. The application of imaging, image processing, computer vision and optimization theory in the field of robot-based neurosurgery is discussed. Further, various open-source image processing libraries and DICOM-based software are explored. Based on the literature review, the progressive and gap area of research is presented.

Chapter 3: Data preparation for robot-based neurosurgery

This chapter discusses the data preparation based on a medical image from the scan for robot-based neurosurgery. Importance of medical image and data preparation for robot-based surgery has been considered. The DICOM standards are explored, and useful DICOM tags are listed and discussed in detail. The method to develop the data visualization, i.e., axial, coronal, sagittal, oblique views, and 3D model of the patient, is presented.

Chapter 4: Modeling and algorithm design for autonomous neuro-registration

This chapter discusses the overall conceptualization, modeling, and algorithm design of robot-based autonomous neuro-registration and neuronavigation for neurosurgery. The patient postures for the neurosurgery, imaging coordinate system, information from the DICOM tags, and its importance for the development of the algorithm are shown. The steps of autonomous neuro-registration, i.e., measurement of the markers in the medical image space, autonomous measurement of the markers in the real patient space, and mapping of markers between the spaces. The detailed analytical formulation of the algorithm for the localization and the precise measurement of the markers are presented.

Chapter 5: Robust Marker Detection and High Precision Measurement for Real-Time Anatomical Registration using Taguchi Method

The need for robust and real-time marker detection and coordinate measurement algorithm for autonomous neuro-registration is discussed. The influence of several noise factors on the marker detection and coordinate measurement are shown. The design and implementation of real-time and robust marker detection algorithm based on the Taguchi method are discussed. The proposed method is presented with three different case studies. Each study presents the real-time markers detection and coordinate measurement in the various realistic situations of the OT.

Chapter 6: Phantom and vegetable specimen based case studies for modeling and algorithm evaluation

In this chapter, the implementation of the method and algorithms developed for the robot-based autonomous neurosurgery is presented. The preparation of the phantoms for the purpose of validation is discussed briefly and shown. Detailed case studies of the validation of autonomous neuro-registration are presented on PVC skull phantom fixed in three different postures. The validation is also shown for glass jar and glass skull phantom. Further, the case study of autonomous neuro-registration conducted on the vegetable specimen is presented.

Chapter 7: Conclusion and future scope

Conclusions are drawn based on the methods that are developed for the purpose of autonomous neuro-registration and neuronavigation. Conclusions on the basis of results from case studies are listed. The summary of the work has been presented. The scope of the present work and progressive topics, wherein research interest being generated are also discussed.

1.4 Contribution of the work

The contribution of the thesis is in development and implementation of the robot-based autonomous neuro-registration and neuronavigation methods for neurosurgery. The method includes following features:

1. Autonomous neuro-registration and neuronavigation.
2. Single surgical robot is utilized to serve neuro-registration and neuronavigation for neurosurgery.
3. No line of sight problem.
4. No need to remember correspondence of the points between the both the spaces.
5. Real-time and robust marker detection and coordinate measurement algorithm.
6. Accuracy comparable to frame-based system without compromising the patient comfort
7. Overall error is less than 1 mm.
8. Method is tested for multiple phantoms and vegetable specimen

Following two main algorithms are implemented in the process of achieving the set of objectives.

1. Autonomous neuro-registration is the extensive algorithm comprising of features like autonomous pair point correspondence, elimination of line of sight problem and positioning of needle.
2. Robust fiducial marker detection and coordinate measurement in the real patient space.

CHAPTER II

Literature Review and State of Art in Neuro-registration, Neuronavigation and Neurosurgery

2.1 Introduction

This chapter reviews the literature leading to the state-of-the-art theory and practices in three important components of neurosurgery. The neuro-registration, neuronavigation and neurosurgery have individually attracted persistent attention and sequentially upgraded the surgical practice and operation. The technology and adaptation of technology has played a significant role. The frame-less procedures have provided new direction in research and development.

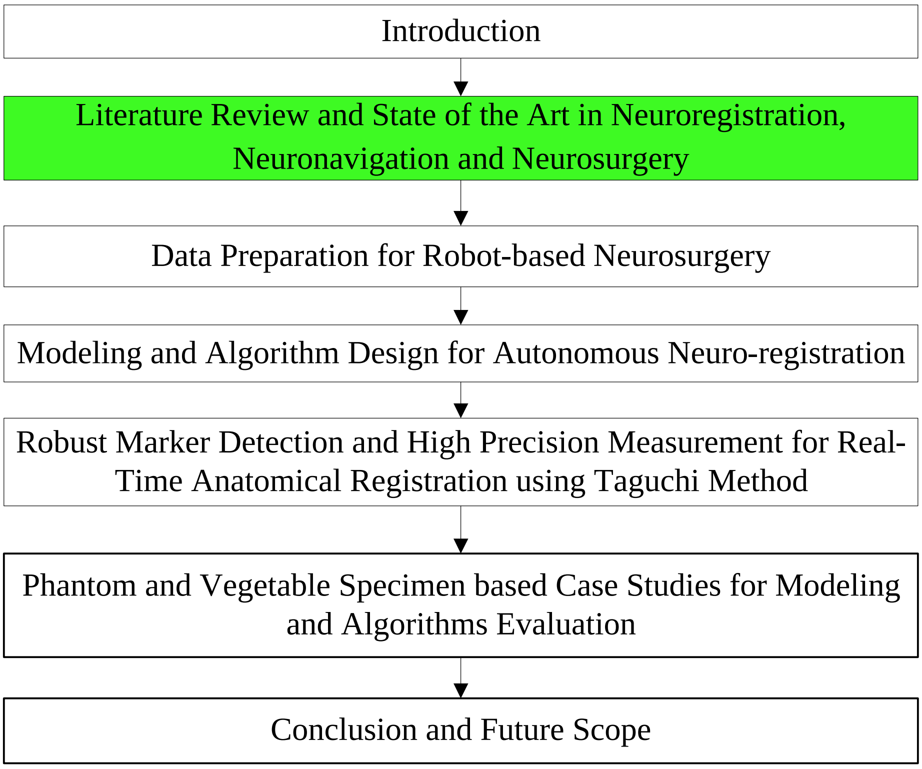

Figure 2.1: Flow of the chapters of the thesis

The constraints of frame-based surgery due to which, shift in research toward the frame-less surgery is seen. Image based planning, guidance and robotics are pioneering stages in neurosurgery. The contributions leading to image guided surgery from conventional surgery has been discussed. Figure 2.1 shows the flow of the chapters of the thesis in context with the present chapter.

2.2 Evolution of Stereotactic neurosurgery

Some of the neurological ailments like brain cancer, Parkinson's disease, epilepsy[1], brain stroke, brain clot, etc may require neurosurgery. Cancer[2] involves the abnormal growth of cells. The growth produces a lump of cells called tumor. The tumor can be benign or malignant. The benign tumor does not spread to other part of the body thus; it is considered as non-cancerous tumor. The malignant tumor spreads to other parts is a cancerous. The very first step is to diagnose the disease by means of medical imaging. MRI or CT scan is mostly used in case of brain imaging. After medical scanning, biopsy can be done, where a small sample of the target tissues are cut and extracted for the pathology test. There are several ways to treat the brain tumor, the most common methods are radiotherapy, chemotherapy and neurosurgery[2]. Parkinson's disease is generally caused by the loss of the neurons that are responsible for the production of chemical called dopamine. Dopamine act as a messenger in brain. Due to lack of dopamine brain starts working abnormally[3]. Deep Brain Stimulation (DBS) is one of the surgical treatments of Parkinson's disease. In DBS a pulse generator is placed inside the chest which sends electric signal to a thin wire placed at the brain through surgery[4].

The opening of the bigger portion of the skull for surgery is referred to as open brain surgery or **craniotomy**[5] (see figure 2.2). The craniotomy involves multiple risks to the patient, which, if feasible should be avoided by restricting the size of invasion of the skull.

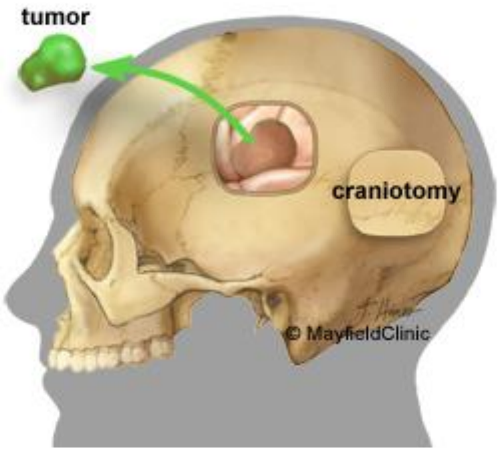

(a) Craniotomy
(iowaclinic.com)

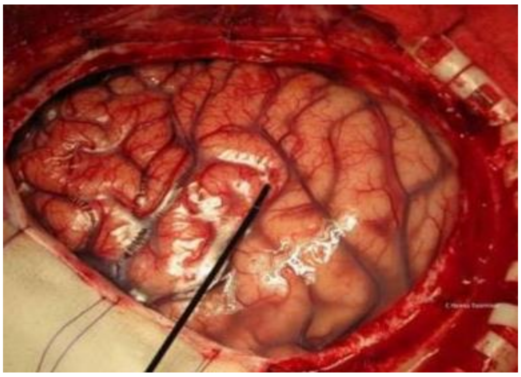

(b) Zoomed view of craniotomy
(wssfn.org)

Figure 2.2: Craniotomy or open brain surgery

Minimally Invasive Surgery (MIS) is a technique to operate within the brain through a tiny burr hole. The MIS reduces the healing time and trauma. The various risks associated with the craniotomy is also avoided by MIS. The technological advancement in medical imaging modalities and image visualisation also enhances reliability and capabilities of MIS[6].

The computation of position of target and tracking of surgical tool by utilising the 3D coordinate system for the application of surgery is known as stereotactic surgery. It is a kind of MIS. This section presents the history of stereotactic neurosurgery and the impact of technologies on development of robot-assisted neurosurgery. Figure 2.3 shows the year wise development of stereotactic neurosurgery apparatus along with the neurosurgical robots. The first stereotactic apparatus was developed by the Horseley and Clake[7] in 1908. The cartesian system was used by the apparatus for the localization of the targets within the brain. Horseley and Clake assumed that the cerebral targets have a rigid relationship between body structures thus, experience values combined into an atlas. The special relations provided by the atlas were having high variation and were not suitable for the human patient. The most successful frame-based stereotactic apparatus was developed by Prof. Leksell in 1947. The latest version of the Leksell stereotactic apparatus is in use till date. Originally, Leksell[8] apparatus was designed to work with the brain atlas. In 1970, Hounsfield and Cormack invented Computed Tomography (CT) imaging technique[9]. The CT was a revolution in the medical imaging. CT scan uses the X rays to create cross-sectional images of the body part. The cross-sectional images then can be processed to make a patient specific 3D model. In 1970, Magnetic Resonance Imaging[10] (MRI) technique was invented. The latest version of the Leksell stereotactic frame is compatible with the CT image and the MRI. A CT guided brain biopsy was performed in 1985 using Unimation's PUMA robot[11]. In 1992 integrated surgical systems introduced the ROBODOC[12] for hip replacement surgery. PUMA and ROBODOC both have serial mechanism architecture. Thus, have the advantage of huge workspace but suffers in terms of robot's accuracy. Intuitive surgical launched the da Vinci[13], [14] surgical system in 2000 for MIS through few small incisions on the stomach. It has a master console and a slave robot with multiple arm. Da Vinci is mostly used by surgeons for the urological and abdominal surgeries.

Table 2.1 shows development activity of neurosurgical robots in application space and their groups.

Table 2.1: Summary of active neurosurgical robots and groups

Surgical robots/Navigator	Region of approval	Working group	Task
CyberKnife	US, FDA,CE, ISO	Accuracy Inc. (USA)	Image-guided radiotherapy
NeuroArm	Health Canada	IMRIS & U of Calgary (Canada)	Stereotactic neurosurgery
Neurostar	No	Neurostar (Germany)	Stereotaxy
iSYS	CE, FDA	ARC Research (Austria)	CT & US-guided biopsies
ROSA	US FDA, CE	Medtech S.A (France)	Stereotactic neurosurgery
NeuroBlate	FDA, Health Canada	Montreris Medical (USA/Canada)	MRI-guided neuro tumor ablation
Renaissance/SpineAssist	CE, US FDA	Mazor Robotics (Israel)	Spinal and brain neurosurgery

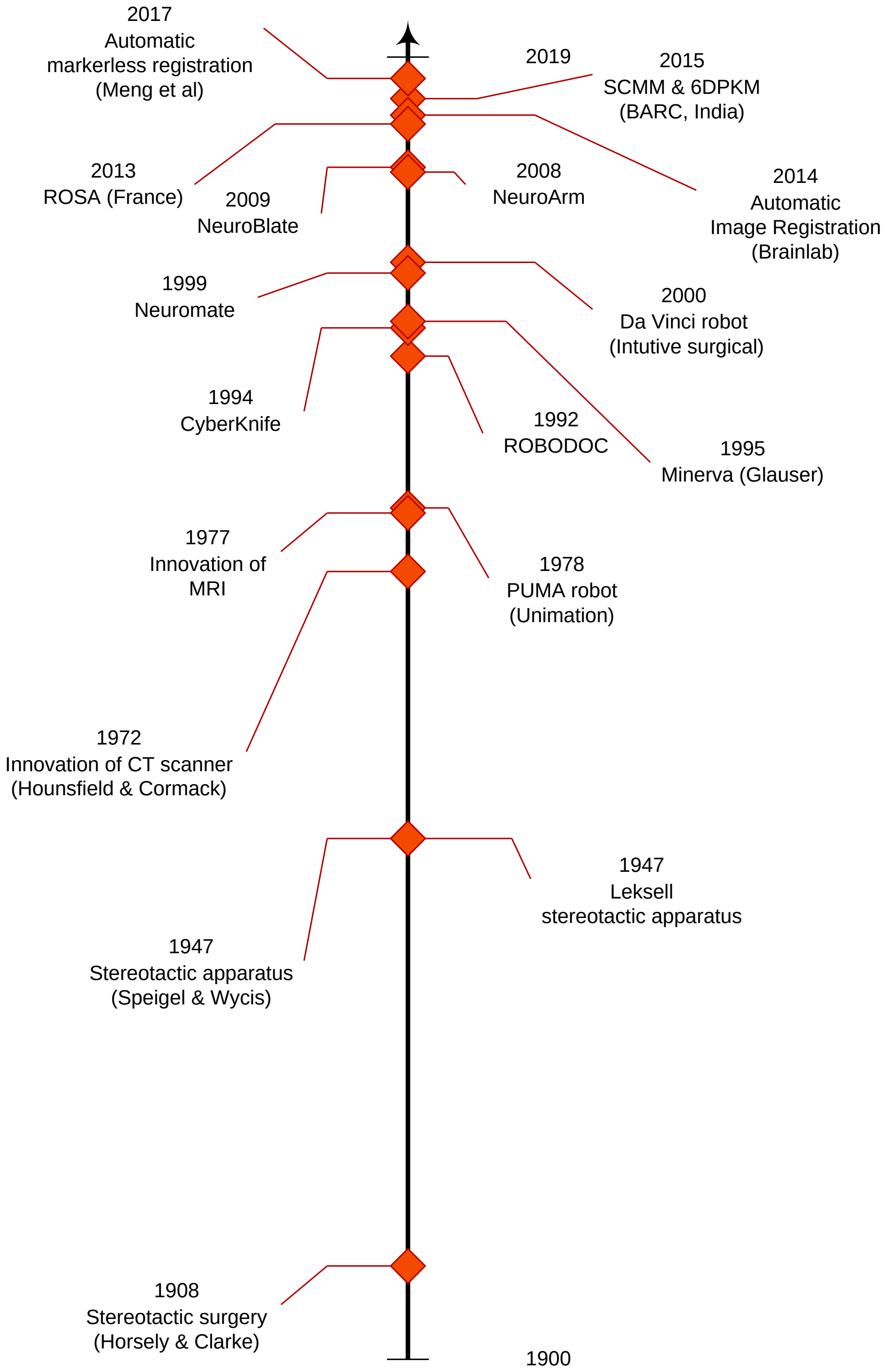

Figure 2.3: Timeline of stereotactic neurosurgery and relevant technologies

Frame based neurosurgical procedure: Stereotactic neurosurgery is also termed as Image Guided Surgery (IGS) or neuronavigation based on the context. Victor Horsley and Henry

Clarke[7] invented first stereotactic system in 1908. Prof. Lars Leksell[8] developed and successfully used a polar coordinate based frame-based stereotactic device to locate the target. The device came to known as Leksell frame, with several modifications over the decades is still being used. In frame-based stereotactic neurosurgery[7], [8], a frame is attached on the head of the patient and the medical scan (CT/MRI) is taken to find the relative position of Region of Interest (ROI) with respect to the frame. Figure 2.4 show the Leksell frame[8] setup. During imaging, only frame is attached. The wearer should take care that the frame does not get disturbed till the surgical procedure is complete. The scaled polar arch is fitted during the course of the surgery. The frame-based system is accurate but due to attached frame, they are not patient friendly.

Figure 2.4: Leksell stereotactic frame and arc (elekta.com)

Frameless systems for Image Guided Surgery (IGS): In frame-less stereotactic neurosurgery[15], [16], the location of the target region is found out based on either anatomical landmark, surface matching or attaching the radio-opaque multimodality fiducial markers. The prerequisite of stereotactic neurosurgery and neuronavigation is neuro-registration (contextually, also referred as registration). The meaning of neuro-registration in general from the literature[7-15] is the process of establishing the relationship between medical image space and real patient space. The real patient space refers to the 3D space of the patient, the surgical tool, navigation system and the robot (in case of robotic surgery). The medical image space refers to the 3D space of the image data acquired by the imaging modalities.

CT[17], MRI[10], [18], Ultrasound Imaging[19], Positron Emission Tomography PET[20], Single Photon Emission Computed Tomography, SPECT[21] are some of the widely used imaging modalities. As already discussed, the CT uses the X rays to form the cross-sectional images whereas the MRI uses the magnetic field to generate the images. The MRI provides better gradients at lower density range, like soft tissue and does not involve X-rays as compared to the CT imaging. Thus, MRI is preferred for the brain scan. Ultrasound imaging[18] utilizes sound waves to detect the tissues and produces the images of the body part. Ultrasound is widely used for soft tissue imaging and intraoperative imaging during the IGS. Syed et al.[22] presented the effect of merging intraoperative ultrasound data with the MRI data for neuronavigation for IGS of high grade gliomas. They demonstrated that Gross Total Resection (GTR) of tumor has improved from 31-36% to 74.3%. The fusion of preoperative images (CT/MRI) and intraoperative real-time ultrasound is mostly done to correct the brain shift or tissue shift[23] during the resection of tumor in IGS. However, merging of intraoperative ultrasound imaging data with the MRI/CT data requires advanced image fusion techniques[24], [25].

Most of the imaging modalities are compatible with the Digital Imaging and COmmunication in Medicine (DICOM)[26], [27]. It is an international standard to cover almost all aspects of imaging like image acquisition, store, transmit, imaging format, image display and print. Most of the software for medical image processing and computing also follows the guidelines of DICOM. 3D slicer[28]–[30] is one of such widely used open source software developed by funding support through National Institute of Health (USA). The software provides tools for image visualization of slices and 3D model, tools for mining image informatics and tools to conduct image processing. Other medical image processing software that are commonly used are Visualization Toolkit[31] (VTK), Insight Toolkit[32] (ITK), OsiriX[33] and RadiAnt[34] DICOM viewer. The VTK and ITK are the open source medical image processing and computing libraries and are compatible with most of the programming languages. It is always preferred to develop custom software basing on these open source libraries. AnuVi software was developed at BARC, India. A portion of medical image processing and image registration software is supplemented to AnuVi to suit the robot-based autonomous neuro-registration. The application of image processing and computer vision concepts have become essential component of any IGS. Lucio et al.[35] presents the human anatomy visualization and navigation system. They discussed the advantages of visualization of conventional medical images, 3D model, slicing and cropping of the images. Bowei et al.[36] developed an augmented reality visualization system for stereoelectroencephalograohy (SEEG) electrode implantation. The system can be used for visualization of internal structure of the patient in medical image space and real patient space. The localization of entry point and computation of the registration accuracy can also be found out using the system. This system is based on projector camera system. This development involves numerous image processing and computing functions. Several, like the image segmentation, image thresholding, cropping, morphological operations are used for image enhancement. While, circle and ellipse fitting to the contours, corner detection, image template matching and histogram equalization are used for acquiring geometrical attributes from the images. Many standard image processing algorithms are provided by open source imaging and computer vision libraries like OpenCV[37]–[39] and scikit-image[40]. These algorithms have several parameters to be tuned, which makes them sensitive to the parameters. The parameters have to be tuned for a certain task. Limited literature on the auto tuning of the parameters are available and none to optimize these parameters in real-time especially in the area of IGS. The design of robust algorithm to optimize the parameters of image processing functions is made in one of the chapters in the thesis. Further, detection and measurement of the fiducial markers for autonomous anatomical registration in real time is addressed. The Taguchi[41], [42] method is used to optimize the parameters of the image processing algorithms used in the sequence. It is one of the most versatile statistical technique used in robust design and quality engineering to improve the process or product by reducing the variance even in the presence of noise factors[42]. Several researchers have applied the Taguchi method in Engineering[43]–[47], Biotechnology[48]–[50] and Marketing[51]. All of the above research dealt with the offline processes wherein real-time was not a consideration. For robot-assisted surgery, the parameters have to be optimized in real-time to reduce the surgical time and to design robust process under the presence of several noises. Frame-less neuro-registration is practiced in multiple ways. The type of practices can be classified in to two broad categories, the development is discussed.

Point based registration: Pair point registration is the process of measurement of at least three points in medical image space and measurement of corresponding points in real patient space and one to one mapping of the corresponding points to find the homogenous transformation matrix to establish the relationship between the medical image space and real patient space.

Figure 2.5: Fiducial markers attached at the scalp

Marker-less pair point neuro-registration[16], [52]–[57] is also known as anatomical landmark-based pair point registration. There is no need to fix any external marker for the reference but this kind of registration suffers from low registration accuracy, due to weak geometric definition of reference point.

Marker-based pair point neuro-registration[15], [55], [58] can be non-invasive skin mounted and invasive bone implanted types. Non-invasive type involves the pasting of radio-opaque multimodal fiducial markers on the scalp of the patient. The invasive type involves the implantation of fiducial markers on to the bone of the patient before the medical scan. Figure 2.5 shows typical radio opaque fiducial markers pasted on the scalp. The brainlab's[59]–[61] pair-point-based neuronavigation system has wall-mounted stereo camera and reflectors. The reflectors are attached on the surgical tool and on the couch to establish the relationship between medical image space and real patient space. Hunsche et al.[54] conducted MRI guided stereotactic neurosurgery. They investigated the fiducial based (skin mounted marker-based) and anatomical landmark-based registration for their standard imaging protocol, including t2-weighted spin-echo as well as contrast enhanced t1-weighted gradient-echo imaging. Fiducial based method shows better result for t2-weighted spin-echo. Whereas for t1-weighted gradient-echo imaging, performance of anatomical based registration was found to be better.

The pair point-based registration depends on number of known corresponding points in both the spaces. Mathematically, three points are required to establish the relationship between two coordinate systems and obtain the close form solution[62]–[65]. In three point-based registration, the three non-collinear points should be measured in both medical image space and the real patient space. The image space is a virtual space whereas the real patient space apart from the patient may consist of the robot, and the other devices.

There are multiple factors that contribute to the error in measurement of fiducial points both in the image and in the real patient space. In image, the sources of errors are due to medical imaging modality, human error in manual measurement, image reconstruction, etc. Registration using more number of points is highly recommended[62], [63], [65]–[67]. Measurement of more than three points is an overdetermined system. Such kind of system can be solved by method of least square[62], [63], [68]–[71].

Most of the registration system for IGS gives some measure to check the accuracy of the registration. West and Fitzpatrick[66], [67], [72], [73] divided the error associated with the registration into 1) Fiducial Localization Error (FLE), which is the error in localization of the fiducial markers 2) Fiducial Registration Error (FRE), which is the distance between corresponding fiducial points after registration and 3) Target Registration Error (TRE), which is the distance between corresponding points other than points used for the registration. Later, West and Fitzpatrick[66], [67], [72], [73] concludes some of the critical aspect of pair point based registration to improve the target registration accuracy and to eliminate the potential dangers of the unsatisfactory practices in IGS. Some of their findings are given below.

1) Most of the commercially available neuronavigation system provides measure of error in terms of FRE., This only indicates the error in geometric alignment of points used in the registration. TRE is the true measure to check the accuracy to reach particular target after registration. TRE can be checked, after registration, by locating or pointing the surgical tool tip at the targets.
2) The accuracy of image guidance system depends on the number of fiducial points, accuracy of localization of fiducial markers points and geometrical configuration of the fiducial points used for the registration. The accuracy of the registration is independent of characteristics of the registered object. The FRE is independent of fiducial configuration and number of fiducials used for the registration whereas, TRE depends on them.
3) TRE can be minimized by using as many points as possible for the registration, avoiding near collinear fiducial configurations and by placing the fiducial markers such that the target is at or close to the centroid of the fiducial points.

Surface registration: The surface registration[74]–[77] involves the mapping of surfaces generated in medical image space and real patient space. This method avoids the use of markers but gives relatively lesser accuracy as compared to the pair point-based registration. In 2018, Fanle et al.[78] developed an autonomous marker less surface registration method. Most common surface registration method works on matching the surface landmarks in real patient space with the imaging space. Surface features can be captured only in supine position. Meng's[74] method automates the registration method and does not constraint the patient in supine position. The method works on extracting a mark on the head of the patient. The final registration is achieved by combination of course and fine registration.

Most of the image guided surgical system and surgical robots rely on non-invasive pair point-based registration technique. The accuracy of skin mounted non-invasive pair point based registration technique is better than surface registration and anatomical landmark based registration but less than bone implanted fiducial marker based registration[15], [79], [80].

Woerdeman et al.[15] compared the application accuracy of three patient-to-image registration methods using optical tracking system based on adhesive marker, anatomical landmarks and surface matching-based methods. The TRE was found to be 2.49 ± 1.07 mm using adhesive marker-based registration. The other two methods i.e. anatomical landmark and surface-based method, TRE was found to be 4.97 ± 2.29 mm and 5.03 ± 2.30 mm respectively. There results show adhesive marker-based registration is most accurate after bone implanted marker-based registration which is rarely used because of its invasive procedure of fixing the fiducial markers.

2.3 Robot-based neurosurgery

Robot-based systems for neurosurgery also makes use of same medical technologies like CT/MRI, image-guidance, neuro-registration, visualisation and neuronavigation. The overall accuracy of the robot-based neurosurgery not only depends on the individual accuracy of each technology but also depends on the accuracy of transformation from one space to the other[81]–[83]. The robot-based neurosurgery enhances the capabilities of the MIS by linking several technologies. In addition, it gives better accuracy, rigidity, reliability and dexterity. In 1997, Integrated Surgical Systems commercialized first image guided, computer-controlled robot for stereotactic functional neurosurgery called Neuromate. Currently Neuromate is owned by Renishaw[84]. It includes the 5 Degree of freedom robotic system and positioning and visualization software (refer figure 2.6).

Figure 2.6: Neuromate robot with phantom skull (renishaw.com)

Figure 2.7: Da Vinci master slave surgical robot (intuitive.com)

Figure 2.8: ROSA surgical robot (zimmerbiomet.com)

Figure 2.7 shows the da Vinci[13], [14] surgical robot. This robot has multiple arms and can be controlled by a remote console. It is by far most used and highly sophisticated surgical robot and mostly used for the abdominal and urological surgeries. Since da Vinci is a Master-Slave manipulator thus it cannot be used for the autonomous surgeries.

Figure 2.9: PathFinder neurosurgical robot with reflective markers [96].

Zimmer Biomet Robotics, a French company, developed ROSA[85] technology for various cranial and spine interventions. As seen in figure 2.8, ROSA is a serial 6 DOF robotic arm and dedicated visualization and image processing software. ROSA is being used in various parts of the world. The device can be used for the frameless stereotactic procedures[86]with high accuracy and less operative time. SEEG, endoscopic procedures, resection of brain tumor and DBS are primary applications of ROSA.

Another robot designed for the neurosurgery is PathFinder[87]. The PathFinder (see figure 2.9) is a mobile robot and can be move in and out of the operating room. The base of the robot can be fixed to the Mayfield clamp. The robotic arm has 6 DOF. The major difference between PathFinder and other neurosurgical robots is localization of the fiducial markers. The PathFinder system comes with the unique radio-opaque and reflective material coated fiducial markers.

Figure 2.10: Parallel mechanism and SCMM based neuro-registration and neuronavigation[88]

The fiducial markers have to be attached at the patient's skull. The markers would be seen in CT and MRI images and can be detected by camera attached at the end effector of the robot. Bhutani[88] (see figure 2.10) developed the surgical coordinate measuring mechanism

(SCMM)[88]–[90] based neuro-registration method and parallel mechanism-based surgical robot [88]. The SCMM is used for the anatomical registration. The coordinates recorded by SCMM is transformed to the 6D-PKM surgical robot through rigid transformation matrix. The use of SCMM eliminates the line of sight problem and SCMM can also be used as a standalone neuronavigation device.

Methods to validate robot-based neurosurgery: Robot-based neurosurgery has the potential to be highly accurate and reliable. The robotic neurosurgical suite is subjected to rigorous tests for validation of safety, accuracy and practicability before operating on human patient. The validation involves stage-wise progressive tests starting from simulation study[91]–[94], experiments on multiple phantoms[95]–[98], experiments on fruit/vegetables[99], [100] to mimic the material density and tissue interaction, animals[101], [102] and cadavers [103]–[106]. Georgi et al.[107] (2017) developed novel miniature robotic guidance device for stereotactic neurosurgical interventions. To compare the accuracy of needle positioning to the target, between robotic and manual method, a preclinical phantom trial and cadaver biopsies was conducted by them. Later, tumor biopsies and intracranial catheter placements were also conducted to check the feasibility and accuracy. The literature related to the preclinical phantom and cadaver studies are available but no published literature is available to mimic the real tissue. This thesis presents the case studies of validation of robot-assisted methods for intracranial application using a vegetable specimen. Each newly developed IGS system, algorithms, methods and surgical robotic system has to undergo rigorous tests for validation of safety, accuracy and practicability before operating on human patient. This thesis also presents the preclinical phantom and vegetable specimen tests.

Efforts to eliminate the human errors and to improve the quality of robot assisted surgery through automation: Robot-based neurosurgery largely rely on multiple techniques like medical scanning, image reconstruction and visualization of medical data, image to patient registration (pair point based or surface based) and robots. All of these techniques are progressively evolving because of technology enhancement and continue to present scope for improvement. The overall quality of robot-based neurosurgery is outcome of quality and reliability of each technique. The quality of robot-based neurosurgery can be improved by reducing the human[108]–[110] errors and improving the accuracy of each technology. In pair point-based registration, the measurement of fiducial markers in medical image space and corresponding markers in real patient space is one of the sources of error. In 2009, Manning et al.[111] developed an algorithm to autonomously locate the centre of the fiducial markers in medical (CT/MRI) image space. The algorithm compares the model of the markers with the surface patches obtain from the medical images. Giovanni et al.[112], in 2012, implemented a novel method based on surface processing and geometric prior knowledge to autonomously locate the fiducial markers. Suligoj et al.[113] developed an autonomous markers localization in planning phase in real patient space. The algorithm works with specially designed retro-reflective spheres attached physically at the cranial bone. The sphere is visible in both medical image and real patient space.

2.4 Gap areas, Progressive areas and scope of work

Modern frame-less, stereo-camera-based neuronavigation[82], [88], [114], [115] and neurosurgical practice largely replaced the frame-based stereotactic neurosurgery[88]. The research and practice are now steadily shifting toward frameless, visualization-based research and practice. The objective of the thesis is to address the following novel and progressive work towards frameless stereotactic neurosurgery.

1. To enhance the accuracy and precision of frame-less stereotactic neurosurgery.

2. To automate the manual procedures associated with the frame-less stereotactic neurosurgery for elimination of human errors and utilize the high precision capabilities of the technology.
3. To eliminate the line of the sight problem associated with the wall-mounted stereo camera.
4. To achieve quick neuro-registration and time optimal neurosurgical procedure

CHAPTER III

Data Preparation for Robot-based Neurosurgery[†]

3.1 Introduction

The robot-based neurosurgery utilizes inputs from the medical images to design algorithms, generate cross-sectional views like axial, coronal, sagittal, oblique view (perpendicular to the tip of the surgical tool) and 3D patient specific models. Further the processed images are used to identify entry point, target point and compute robot tool-tip path. This chapter presents the preparation of data from the medical images and forms the basis for proposed objectives of the thesis. The image-based data preparation in the workflow chart shown in figure 3.1. As can be seen this chapter builds the foundation for robot-based neurosurgery. The cross-sectional images and 3D models will aid in neuro-registration, neuronavigation and overall robot-based neurosurgery.

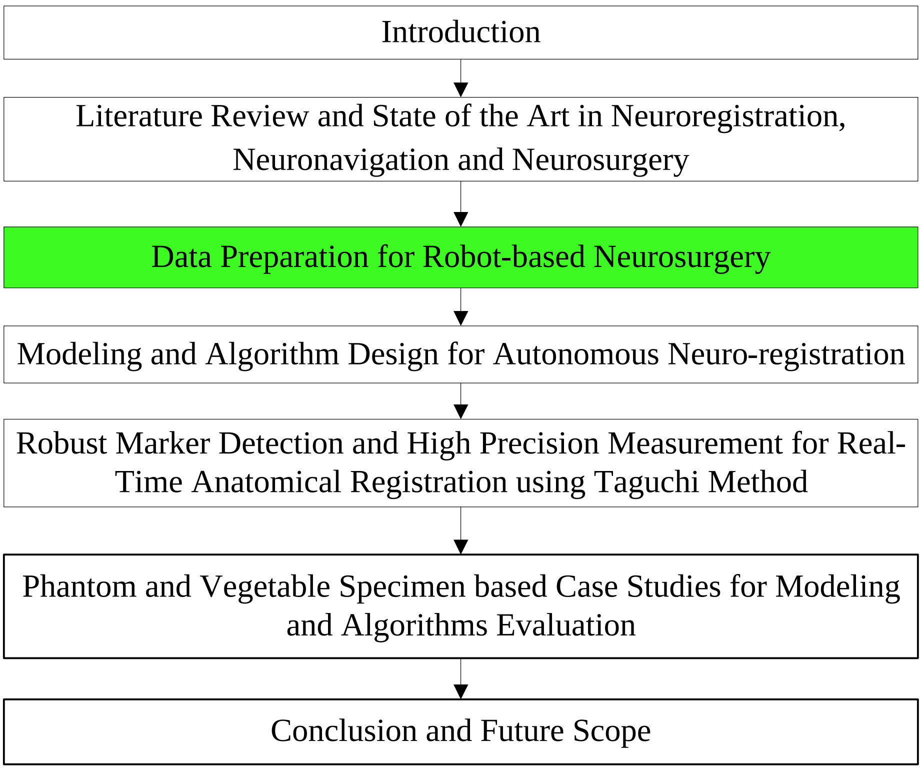

Figure 3.1: Data preparation in context of the workflow.

† "Image-Based Data Preparation for Robot-Based Neurosurgery", Kaushik A., Dwarakanath T.A., Bhutani G., Venkata P.P.K., Moiyadi A, In: Badodkar D., Dwarakanath T. (eds) Machines, Mechanism and Robotics. Lecture Notes in Mechanical Engineering. Springer, Singapore, 2019. https://doi.org/10.1007/978-981-10-8597-0_3

3.2 Patient preparation and medical scanning

The first step toward the robot-based neurosurgery is patient preparation. The fiducial marker-based registration (skin mounted pair point-based registration) involves the pasting of radio-opaque multimodality fiducial markers on the shaved head of the patient. After pasting the markers, the patient would undergo the medical scan i.e. Computed Tomography (CT) or Magnetic Resonance Imaging (MRI) based on the imaging resolution as suggested by the neurosurgeon. The markers should be kept intact till the time of surgery. These fiducial markers would be visible in the medical images along with the other details of the head like bones, vanes, arteries and problem region. The fiducial markers should encompass the region of interest and is validated in chapter 6. The higher neuro-registration accuracy can be achieved for the target close to the centroid of the volume created by the reference points at the fiducial markers[116]. The cross-sectional views and 3D model generated from medical scan would be used for neuro-registration and neuranavigation.

3.3 Preparation of medical data for robot-based neurosurgery

The medical data generated by the medical imaging modalities follows the Digital Imaging and Communication in Medicine (DICOM) standards. DICOM is a set of standards formulated to maintain the standardization among the various stack of images, data types and the communication between various modalities, workstations and other devices. It records image-related parameters such as patient 3D position, sizes and orientations, slice thickness, modality used, information related to the patient, the doctor and the hospital [26], [27]. All these information makes patient information unique throughout the globe and is stored in DICOM data tags. The DICOM data tags are meticulously identified and utilized for various aspects of robot-based neurosurgery. A software module is developed to performs the following operations:

1. The segregation of images based on DICOM tags.
2. The placement of images at appropriate location.
3. The generation of 3D model and oblique view from the 2D slices.
4. Isolation of ROI (Region of Interest) in transparent patient specific skull based on MR or CT images.

Most of the features are independently developed in the institute. Some features of the software are developed by modifying and customizing the open source medical image processing libraries like: VTK, ITK and OpenCV.

3.3.1 Visualisation of cross-section images and 3D model of the patient

The cross-sectional images obtained from CT/MRI scan has to be arranged appropriately. The images are segregated based on the DICOM Unique Identifiers (UIDs). As can be seen from the figure 3.2, a patient can have multiple scans like multiple MRI scan of the neck or separate CT scan of the head. In DICOM compatible imaging modalities and software, all scans of the patient come under one unique patient ID (UID). The patient can have multiple studies and allotted different study instance UIDs (0020, 000D) which is unique for each study. Further, study can have multiple series based on directions like axial, coronal and sagittal or based on a scan with contrast medium or without a contrast medium. In DICOM, each series is assigned with series instance UIDs (0020, 000E) which is unique for each series. Each series may have multiple images and each image has a unique Service-Object Pair (SOP) instance UID (0008, 0018).

A software module based on the given classification is developed to read the UIDs of the images and arrange them in their pre-designated locations in the series and study. Generally, images belonging to a particular series have the same orientation. Basically, a 3D coordinate space in medical image space [I] is used in the acquisition of 2D medical images. Note that the terminologies like medical image space, patient coordinate system, anatomical coordinate system and DICOM coordinate system are all same 3D space with a coordinate system and in the rest of the text, the term, medical image space [I] will be used. The medical image space is fixed and fully defined by the lying posture of the patient on the image scanner couch. The medical scanner generates a regular rectangular array of images. From this array, the axial, coronal and sagittal views can be generated.

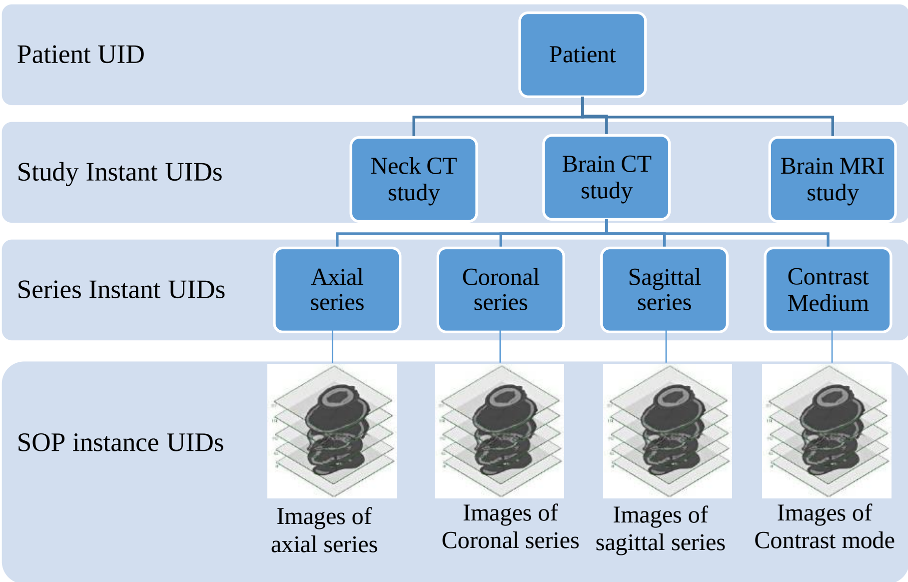

Figure 3.2: Segregation of medical images based on UIDs

Images acquired by the scanner are in 2D and it is required to map the position and orientation of these 2D images with reference to the medical image space [I]. For this, the procedure given in the DICOM standard 3.0[27] is adopted. The image plane and the pixel spacing attributes of the DICOM standards, mentioned below are used to map the position and orientation of the 2D images with respect to [I]. The important DICOM tags are discussed below:

I. Image Position DICOM Tag (0020, 0032): This tag provides the coordinates (S_x, S_y, S_z) of the centre of the first voxel (at the top left corner of the image) with respect to the [I].

II. Image Orientation DICOM Tag (0020, 0037): This tag provides the direction cosines of horizontal (X_x, X_y, X_z) and vertical (Y_x, Y_y, Y_z) axes of the 2D images with respect to the [I].

III. Pixel Spacing DICOM Tag (0028, 0030): This tag provides the column and row pixel spacing (Δi, Δj) in mm.

IV. Slice Thickness DICOM Tag (0018,0050): This tag provides the nominal slice thickness, in mm.

V. Slice Location DICOM Tag (0020,1041): Relative position of the image plane expressed in mm with respect to [I]

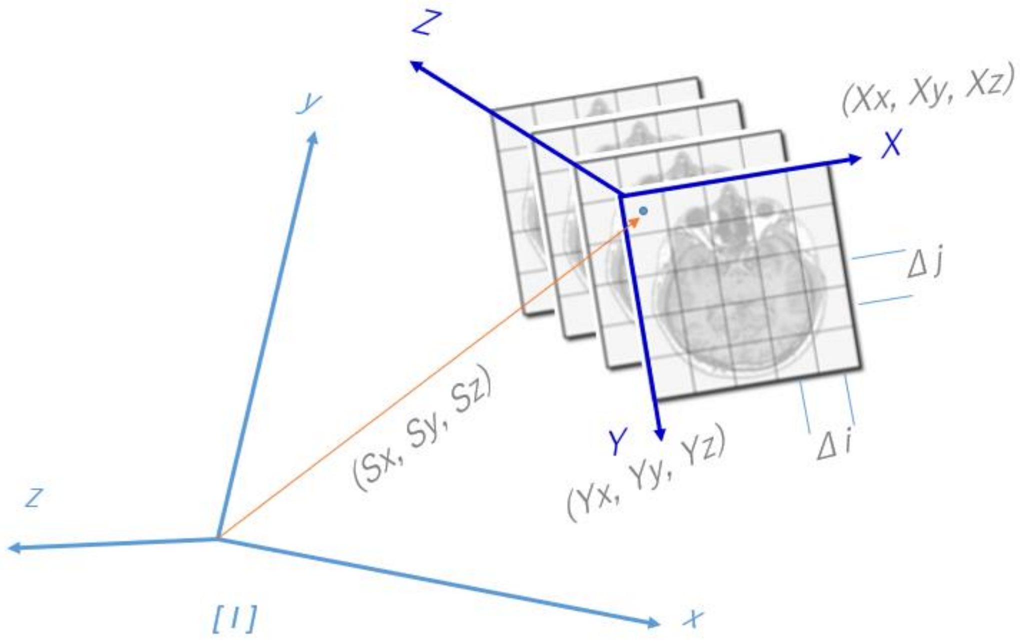

Figure 3.3: Mapping of position and orientation of stack of 2D image with respect to Medical Image Space [I]

The coordinates of the voxel (i, j) in the image plane with respect to the [I] (in mm) is given as:

$$P_x(i,j) = X_x.\Delta i.i \ + Y_x.\Delta j.j + S_x \qquad 3.1$$

$$P_y(i,j) = X_y.\Delta i.i \ + Y_y.\Delta j.j + S_y \qquad 3.2$$

$$P_z(i,j) = X_z.\Delta i.i \ + Y_z.\Delta j.j + S_z \qquad 3.3$$

Where i, j are the column and row index to the image plane. The DICOM tags, structure of voxels and slices are used to develop the medical image visualization software module for neuronavigation. Figure 3.3 shows the mapping of position and orientation of the 2D images with respect to the 3D Image coordinate system [I] in medial image space. In figure 3.3, the Cartesian coordinates (X, Y, Z) of the medical image space is a 3-dimensional orthogonal coordinate system, The axes are the coordinate axes of medical image space [I]. The 2D images are obtained from the CT/MR scanning and mapped to the 3D coordinate system in the medical image space. The DICOM tags, described above, are used to map the images. Figure 3.4, figure 3.5 and figure 3.6 shows the implementation of above mention procedure to develop three cross-sectional views, oblique view, 3D model and isolated skull surface with the highlighted tumor respectively. Along with the three standard views, an oblique view is also generated. The section at the tip and perpendicular to the axis of the surgical tool is the oblique view. The oblique view is a real-time image and changes as the surgical tool progresses. As the surgeon moves the tool, the oblique view generates the image perpendicular to the tool at the tip. Thus, the oblique angle is not constant. During the surgery, the view normal to the surgical tool provides critical feedback about the right localization to the surgeon. In figure 3.4, the oblique view shows the cross-sectional images perpendicular to the tip of the surgical tool pointing.

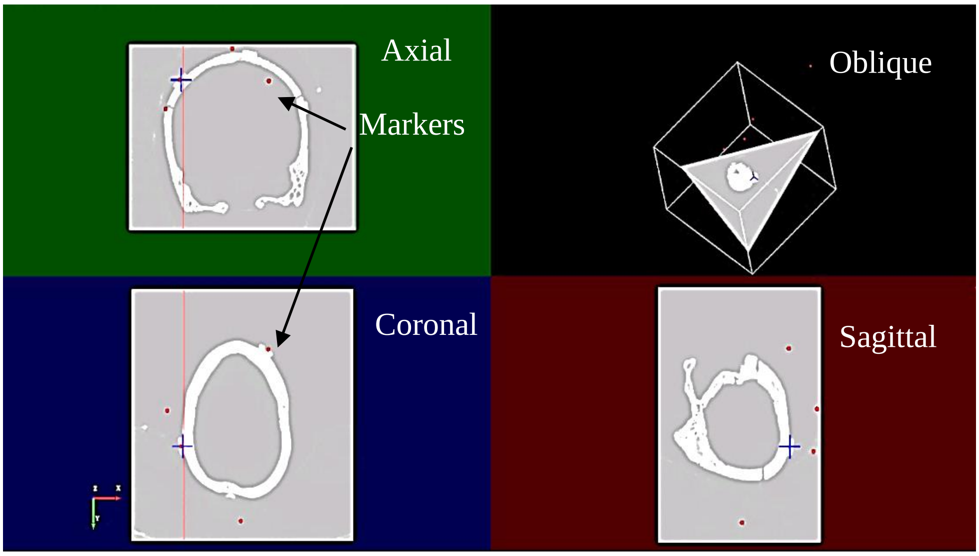

Figure 3.4: Axial, coronal, sagittal and oblique views generated from the medical imaging data (red dot indicates the measured reference points at the markers)

The cross-sectional views and 3D model (see figure 3.5 and figure 3.6) would be used to measure the coordinates of the markers with respect to the Medical image space [I]. After selecting the markers in the 3D model, the precise measurement can be done by fine-tuning the measurement in the cross-sectional views. Figure 3.6 shows the isolated visualization of the region of interest along with the skull surface for the reference. The views can be rotated and magnified to ease the measurement.

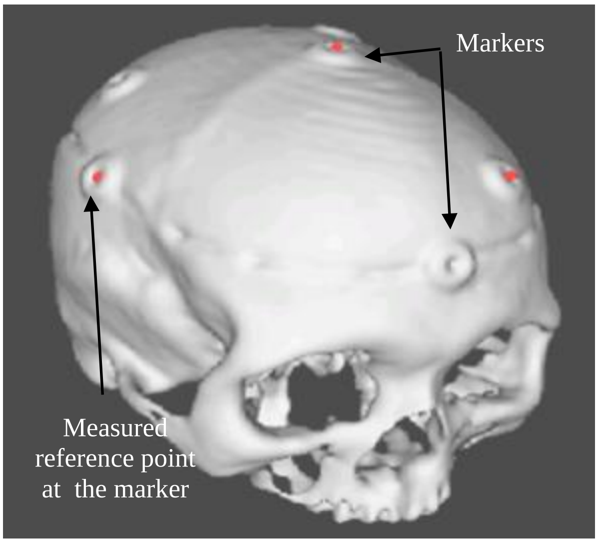

Figure 3.5: 3D model generated from the medical imaging data

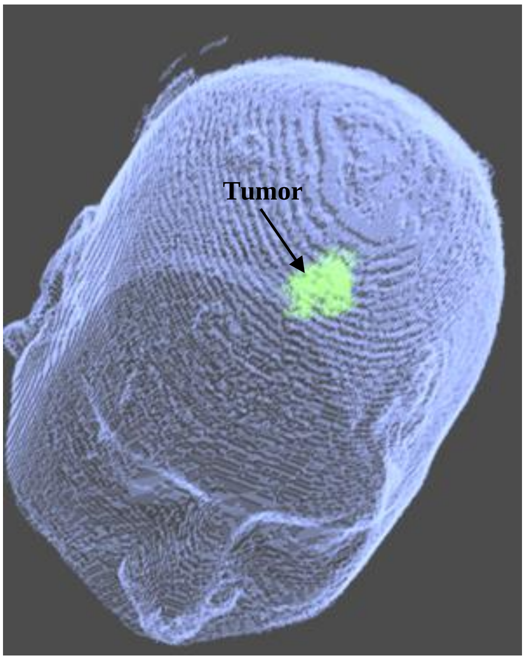

Figure 3.6: Isolated tumor and skull surface model

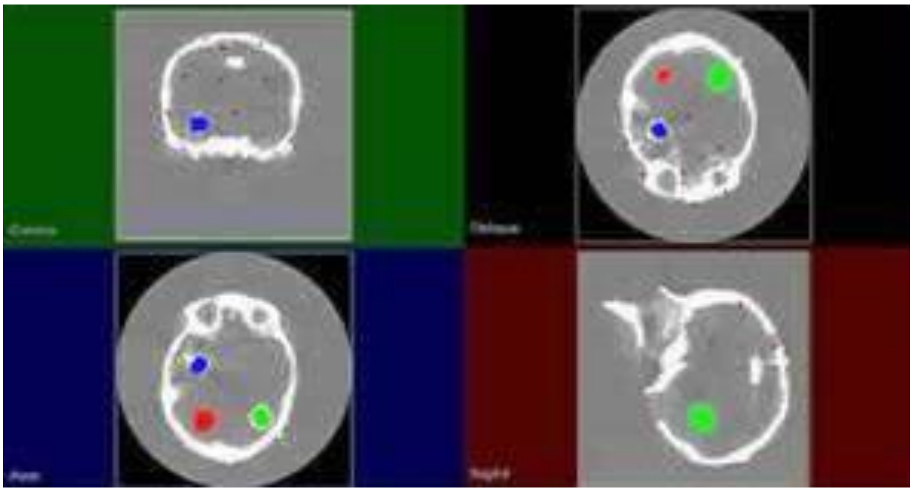

Figure 3.7: The multiple ROI marked in the generated image

The cross-section views shown in figure 3.4 and 3.7 will be useful to measure the markers, Region Of Interest (ROI), entry point and target points. All the views and 3D models will be useful for the neuro-registration and neuronavigation (discussed in subsequent chapters).

3.4 Conclusions

The importance of patient preparation for robot-based neurosurgery is lies largely on image assessment. The acquisition of medical images with fiducial markers is a basic step towards frameless stereotaxy. The DICOM standard is explored. The DICOM tags are meticulously identified and utilised to build the visualization module of the software to support the further aspects of the robot-based neurosurgery.

CHAPTER IV

Modeling and Algorithm Design for Autonomous Neuro-registration[†]

4.1 Introduction

Robot-based neurosurgery involves integration of various tools and devices to locate, visualize and operate at the problem area within the confines of the brain. The convergence of robots, medical imaging and visualization has led to highly enhanced and newer practices in neurosurgery. This chapter presents a novel method for autonomous neuro-registration and neuronavigation. The image-based data, i.e. cross-sectional views and 3D models would be extensively used in the algorithm presented in this chapter. The modeling and algorithm design for autonomous neuro-registration in the workflow (shown in figure 4.1) is one of the core objectives of the thesis.

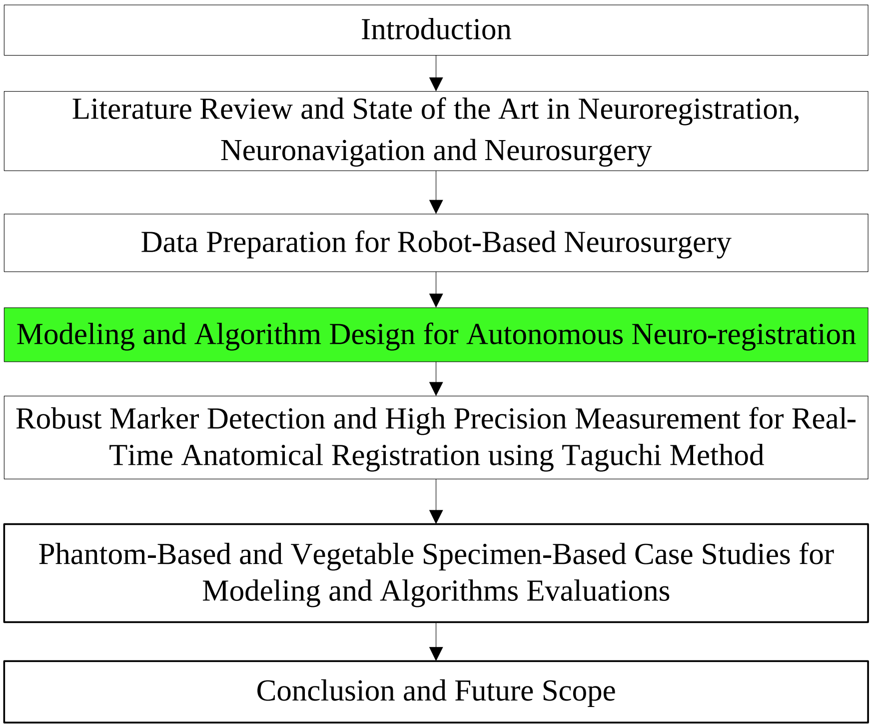

Figure 4.1: Connectivity of Modeling and algorithm design for robot-based neurosurgery in context of the workflow in the thesis.

[†]“Autonomous neuro-registration for robot-based neurosurgery”, Kaushik A, Dwarakanath TA, Bhutani G. International Journal of Computer Assisted Radiology and Surgery, Springer. 2018. 13, 1807–1817https://doi.org/10.1007/s11548-018-1826-3

The method automates the neuro-registration process to enhance the overall accuracy of the robot-based neurosurgery. The algorithms in the method deals with the robot-based autonomous measurement of fiducial markers in the real patient space. The algorithm autonomously locates the markers. The coordinates of the reference center points on the markers are autonomously measured using the images captured by the camera and inverse kinematic solution of the robot configuration. Correspondence with the same points on the medical image is autonomously applied to obtain the mapping of the image points with respect to the robot for high accuracy registration in the shortest time. The method improves registration accuracy, eliminates line of sight problems and results in faster registration.

4.2 Methodology

A 6 Degree of Freedom Parallel Kinematic Mechanism (6D-PKM) robot is used for neuro-registration, neuronavigation and neurosurgery; the robot in surgical mode is shown in figure 4.2. It can be noted that there is no separate robot for the neuro-registration. The 6D-PKM robot is a compact portable system weighing 150 N, and it can support and manipulate a payload of 200 N. The repeatability of the robot is 10 µm, and absolute accuracy is 60 µm. It has a three translational, and three rotational DOF, which can approach a point in its workspace from multiple directions or in other words the end platform of the robot can be positioned and oriented at the desired posture. The detailed workplace, work volume, synthesis and sensitivity analysis is given in the thesis[89] of the earlier researcher from the same institute.

The neuro-registration is a multi-thronged process (1) Measurement to determine the coordinates of the markers, the centre point of Region Of Interest (ROI) and the feasible entry points in the medical image space. (2) Measurement in the real patient space to determine the coordinates of the physical markers with respect to a physical space (in this case with respect to the robot). (3) One to one mapping of the points in the medical image space to the real patient space to establish the correspondence between the medical image and the real patient space.

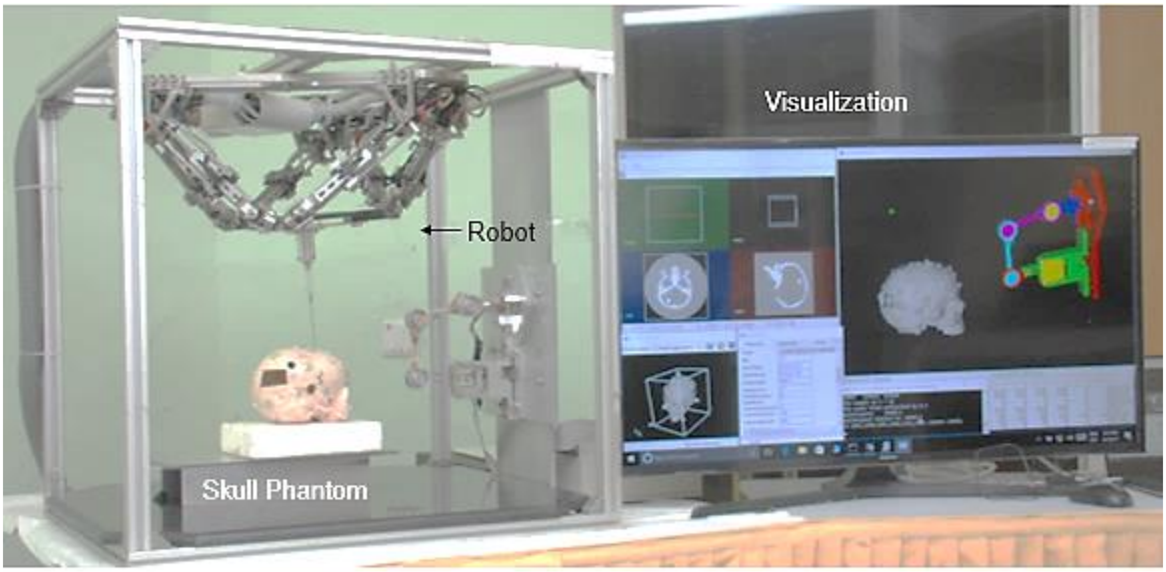

Figure 4.2: Neurosurgical robot along with visualization for neuronavigation

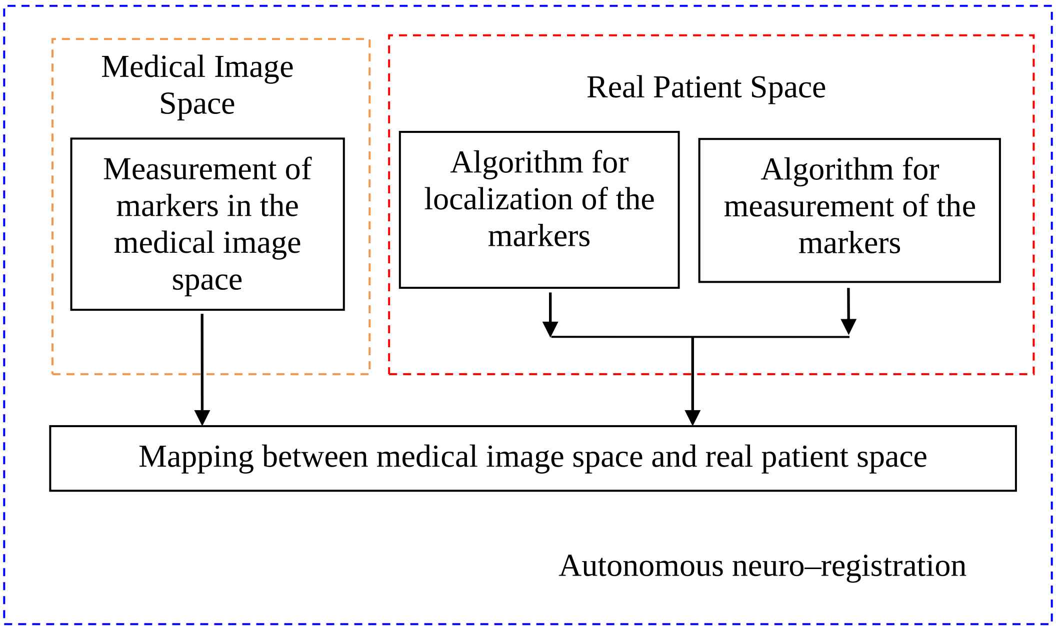

Figure 4.3: Flowchart of neuro-registration process

Figure 4.4: CT scan of skull phantom in supine posture

Thus, any action in the real patient space can be shown in the medical image space with identical correspondence. Various virtual reference frames are established, and relationships are developed during the physically disconnected process of (1) and (2). The steps of autonomous neuro-registration are shown in figure 4.3, and the stepwise procedure is described below. The description of case studies is based on the CT scan data, and the method is independent of imaging modality.

4.2.1 Medical Scanning:

The CT scan of the skull phantom has been taken in the supine posture (see figure 4.4) with CT parameters of 0.625 mm slice thickness, Head First Supine (HFS) position and axial mode. Optima CT 540, CT machine of General Electric Medical Systems has been used (the method is independent of the machine type). The CT data has been stored in the DICOM format.

4.2.2 Measurement of coordinates of the markers, entry and target points in medical image space [I]:

The Patient CT data has been loaded in the neuronavigation software developed at the author's laboratory (as discussed in the chapter 3). The software module is used to measure the coordinates of the centre of the markers in the medical image space [I]. Figure 4.2 presents the snapshot of the neuronavigation software utility, which provides standard three views, viz, axial, the coronal, the sagittal. Additionally, the oblique view along with a patient 3D model generated from the CT data is provided. The centres of the markers can be selected by browsing the slices from any of the views or 3D model, the selection can be verified in multiple views, and then the coordinates can be recorded. An isolated ROI is available (as shown in figure 3.6) to visualise the location, region of spread for selection of target points and to plan the possible entry points.

4.2.3 Measurement of coordinates of the markers in the real patient space:

Apart from measurement of markers in the [I], the other process is to measure the coordinates of the markers in the real patient space [RB]. A high-resolution digital camera and a surgical tool are mounted on a platform of the robot (see figure 4.5). A digital camera (Dino-Lite Edge AM7115MZTL) of size 10.5 cm (Height) x 3.2 cm (Diameter) has been used in the present work. The resolution is 5 MP, the working distance is 150 mm, and the field of view is 19.6 mm x 15.6 mm. The phantom is locked in the place using a Mayfield clamp for measurement of the markers. In the real patient space, the markers are measured autonomously by the robot in two stages: Initial localization, for the gross localization of the markers and then the precise measurement of the coordinates of the reference points on the markers.

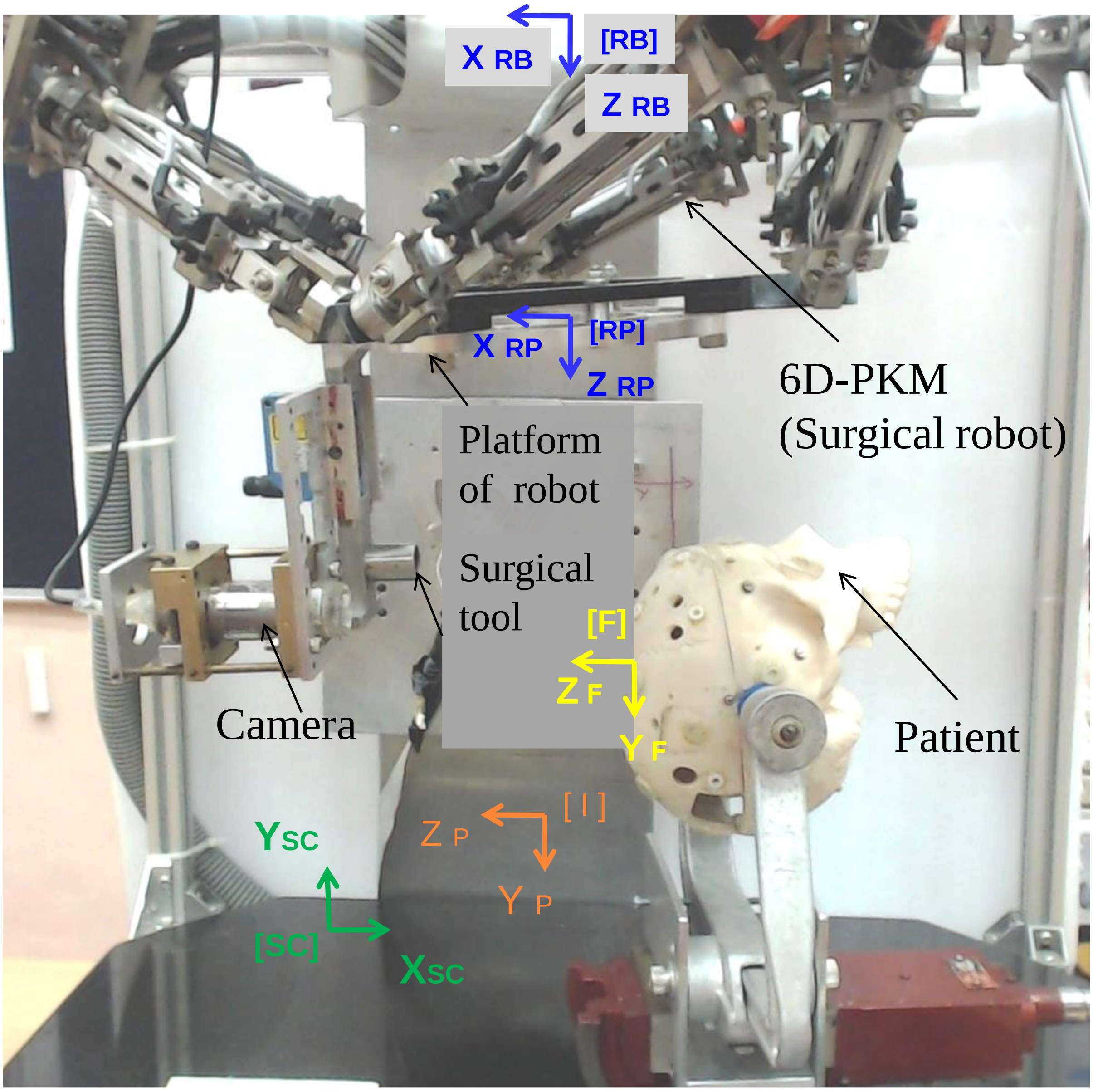

Figure 4.5: Surgical robot with tool and camera, skull phantom placed in HFS pose, [RB], [RP], [F], [I], [SC] representsthe Robot Base, Robot Platform, Fiducial, Image and Surgical Couch Coordinate System respectively

Algorithm for the localization of the markers (Initial localization):

The algorithm for the localization of the markers is developed to locate the markers in the real patient space, with respect to the robot base coordinate system [RB] before precise coordinate measurement, the markers are localized on the basis of the pre-surgical information as stated in the following steps:

I. Coordinates of the centre of the markers are known with respect to the medical image space [I].

As discussed in section 4.2.2, the coordinates of the centre of the markers in medical image space [I], are already measured.

II. Posture of the patient during neurosurgery is known.

Patient positioning for neurosurgery and the majority of spine procedures begins with positioning of the head. Special attention is paid to the skeletal fixation of the head with the pins fixation device, providing both immobility of the head and surgical convenience. The head can be safely rotated between 0 and 45° lateral to the left and right from the body's sagittal axis[117]. Next is positioning of body of the patient. There are five basic body positions utilized in neurological surgery: (1) supine, (2) lateral, (3) prone, (4) sitting, and three-quarters[117], [118]. Thus, positioning of the head and body of the patient will be decided as a part of the pre-surgical planning and would be known before neuro-registration and neurosurgery. Figures 4.6 and 4.7 show the patient is lying in the supine and lateral positions respectively and figure 4.8 shows the patient in the sitting position.

III. Orientation of [I] is known with respect to the Surgical Couch coordinate system [SC].

A coordinate system is attached at some suitable location on the surgical couch and is referred as the surgical couch coordinate system [SC]. As already discussed, the medical scan of the patient was taken in DICOM standard. The stack of 2D images was arranged in the 3D coordinate system of the medical image space [I]. The definition (position of origin and orientation of axes) of [I] is based on the patient posture (listed above) and the guidelines of DICOM 3.0 standards[26], [27].

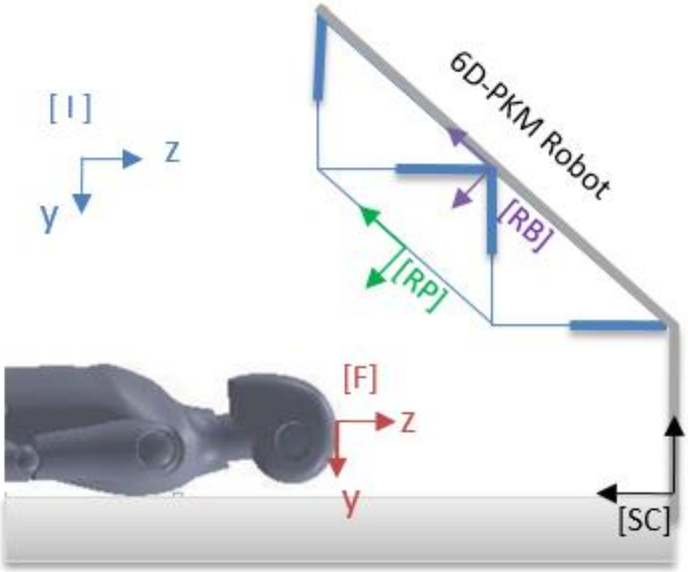

Figure 4.6: Patient lying in supine position

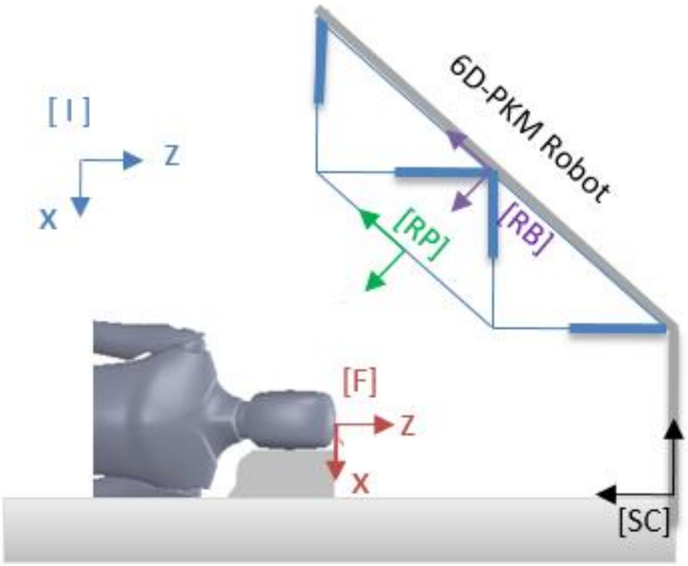

Figure 4.7: Patient lying in lateral position

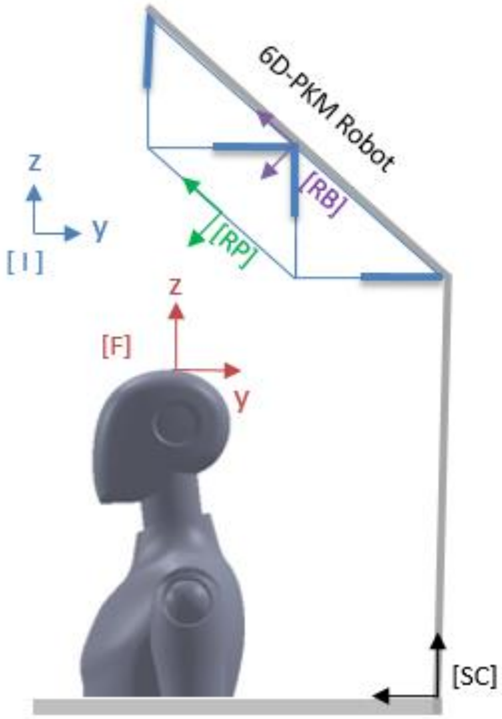

Figure 4.8: Patient in sitting position

As per the DICOM standards, the X axis is defined from right to left hand side of the patient, while the, Y axis is defined from the anterior to posterior of the patient, and Z axis from the inferior (foot) to the superior (Head) of the patient. Hence the orientation of [I] is approximately known with respect to [SC]. Figure 4.6, figure 4.7 and figure 4.8 show the orientation of [I] in supine, lateral and sitting postures respectively during robot-based neurosurgery.

IV. Posture of Fiducial coordinate system [F] is approximately known with respect to [SC]

A coordinate system with identical orientation as that of the coordinate system of medical image space [I] is attached to the centre of one of the fiducial markers. This coordinate system is referred as the fiducial coordinate system [F]. As described earlier, the coordinate system attached on the surgical couch is referred as [SC]. The marker whose position can be easily measured with respect to [SC] will be selected for fixing the coordinate system [F].

The position of one of the markers for fixing the [F] with respect to [SC] is approximately measured using a graduated scale on the surgical couch. Accurate measurement of the position and orientation of [F] with respect to [SC] is not necessary. The orientation of [F] with respect to [SC] is already known because [F] is parallel to [I] and orientation of [I] is known with respect to the orientation of [SC] (as discussed in step III). Thus, the patient posture during neurosurgery decides the orientation of [I] as per the standards and as a consequence decides the orientation of [F]. Figure 4.6, figure 4.7 and figure 4.8 show change in orientation of [F] due to change in [I].

V. Posture of the Robot Base coordinate system [RB] is known with respect to the Robot Platform coordinate system [RP]

Since the 6D PKM robot is already installed, posture of [RB] is known with respect to [RP]. Also [RB] is known with respect to [SC] as they are fixtures in the OT.

The mathematical relationships formulated based on the above knowledge and data is represented in Equations 4.1, 4.2 and 4.3. Thus, if the coordinates of any point are known in [I], its coordinates can be calculated (approximately) with respect to [RB]. Equation 4.1 is being used to calculate the coordinates of markers with respect to [RB]. In this chapter, all **P** represent the position vectors and all **T** represent the homogenous transformation matrices.

$$\boldsymbol{P}^{RB}_{i_{approx}} = \boldsymbol{T}^{RB}_{SC}\, \boldsymbol{T}^{SC}_{F_{approx}}\, \boldsymbol{T}^{F}_{I}\, \boldsymbol{P_i}^{I} \tag{4.1}$$

$$\boldsymbol{T}^{RB}_{i_{approx}} = \boldsymbol{T}^{RB}_{SC}\, \boldsymbol{T}^{SC}_{F_{approx}}\, \boldsymbol{T}^{F}_{I} \tag{4.2}$$

$$\boldsymbol{T}^{F}_{I} = [\boldsymbol{T}^{I}_{F}]^{-1} \tag{4.3}$$

Where,

$\boldsymbol{P}_i{}^I$ are the coordinates of the i^{th} selected marker point with respect to the medical image space [I]

$\boldsymbol{T}_{I}^{F}$ is the transformation of [I] with respect to [F]

$\boldsymbol{T}_{F}^{SC}$ is the transformation of [F] with respect to [SC]

$\boldsymbol{T}_{SC}^{RB}$ is the transformation of [SC] with respect to [RB]

$\boldsymbol{P}_{i_{approx}}^{RB}$ are the approximate coordinates of the selected marker point, *i*, with respect to the robot base coordinate system [RB].

Thus, the above algorithm utilizes the equation 4.1 (mentioned above) to locate the markers. The purpose of the initial localization is for the coarse localization of the markers. The idea is to get each marker (one by one) within the field of view of the camera attached to the robot when moved to the approximated points. Thus, the input need not be very accurate and can be a coarse estimate without any measurement. Since the input of Equation 4.1 is the coordinates of the markers, in certain sequence, with respect to the [I]. Thus, the robot will also follow the same sequence and establish the correspondence automatically. Figure 4.9 shows the validation of initial localization algorithm (equation 4.1). The robot has reached the markers one by one.

Marker1 Marker2 Marker3 Marker4

Figure 4.9: Markers within the viewing window of the digital microscope. The field of view of the camera is 19.6 mm x 15.6 mm

Algorithm for the Measurement of the coordinates of the markers (Precise measurement):

The initial localization is conducted to ensure that the robot can be autonomously navigated close to the marker, both in position and orientation in order to facilitate high precision camera measurement. Once the marker is found to be in the field of view of the camera and within the pre-determined range of position and orientation, the precise measurement is carried out using this algorithm. The emphasis of the algorithm is to determine the 3D coordinates of the reference points on the markers using the camera with high precision.

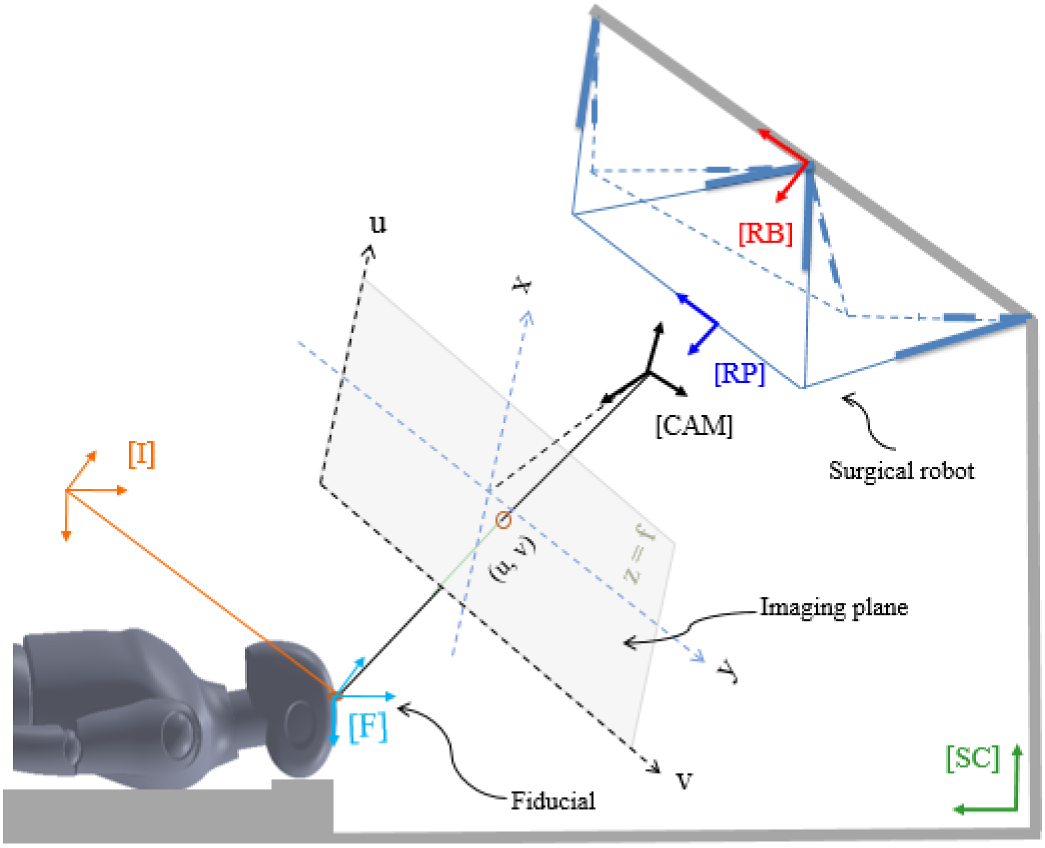

Figure 4.10: Coordinates of one of the markers is precisely measured by the camera mounted at the platform of the surgical robot. [I], [F], [CAM], [RP] and [RB] are the patient, fiducial, camera, robot platform and robot base coordinate system, respectively

The algorithm sets the robot to traverse in both position and orientation, such that the field of view of the camera would reach the first marker based on the initial localization algorithm (refer equation 4.1). After reaching the first marker the robot will pause, and the precise measurement algorithm will initiate the capturing and processing of the images (captured by the camera) from the set position and orientation. The images are processed to match and fit a contour identical to the size of the marker within a minimal pre-set error. If a match is found, it is interpreted as the marker, and the two coordinates of the centre of the circle or ellipse (contour) of the marker in the camera imaging plane (normal to the Z-axis of the camera coordinate system) are determined. The illustration of determining two coordinates of the centre of the marker in the camera imaging plane is shown in Figure 4.10. It can also be seen from figure 4.10; that the camera has a 3D coordinate system called camera coordinate system [CAM]. The projection of circular marker would be ellipse on the imaging plane of the camera. After fitting the ellipse at the imaging plane, the centre of the ellipse is computed with respect to the imaging plane. Equations 4.4 and 4.5 are used to find the x_i^{CAM} and y_i^{CAM}coordinates of the *i*th marker as a function of the distance of marker from the origin of the camera coordinate system (z_i^{CAM}).

$$x_i^{CAM} = \frac{(u_i - C_x).z_i^{CAM}}{f_x} \qquad 4.4$$

$$y_i^{CAM} = \frac{(v_i - C_y).z_i^{CAM}}{f_y} \qquad 4.5$$

Where

Subscript *i* is the counter of markers used for the registration (*maximum of 4 is used*),

u_i and v_i are the coordinates of the centre of the fitted circle/ellipse (based on the orientation of the marker) on the markers in the camera image plane coordinate system (in pixels).

x_i^{CAM} , y_i^{CAM} and z_i^{CAM} are the coordinates of the centre of the markers with respect to the camera coordinate system [CAM].

The values of C_x, C_y, f_x and f_y are intrinsic parameters of the camera, C_x and C_y are the principal points and f_x and f_y are the focal lengths expressed in pixel units. These intrinsic parameters are determined by one-time calibration of the camera using checkerboard. The intrinsic camera calibration error is 0.03702 mm. The camera is calibrated using algorithm provides in OpenCV (open-source computer vision library)[39], [119], [120].

After measuring the two coordinates of the first marker, the robot is released by the algorithm to traverse to the next marker in the sequence and measure its two coordinates using equations 4.4 and 4.5. The steps are repeated until the last marker's image is captured by the camera and processed by the algorithm. It can be noted that the robot moves to each of the four markers in a sequence using initial localization algorithm. The sequence of measurement is the same as that of the sequence followed in conducting the medical image measurement. A supplementary DICOM tag pertaining to the sequence is generated. It stores the order of the markers measured in the [I] and will serve as the traversing sequence for the robot in the autonomous real patient registration. Thus, chances of mismatching of the markers between the two spaces is eliminated.

After completing the measurement of two coordinates of the centre of each participating marker, the next step is to measure the third coordinate of the centre of each marker. Since real patient (phantom, in this case) is in three-dimensional space, the centre of the marker in the 3D camera coordinate system is referred to as position vector, $\boldsymbol{P}_i^{CAM}$. x_i^{CAM}, y_i^{CAM} and z_i^{CAM} are the coordinates of the position vector given in equation 4.6. Note that, x_i^{CAM} and y_i^{CAM} are obtained in terms of z_i^{CAM} (refer equation 4.4 and 4.5).

$$\boldsymbol{P_i}^{CAM} = [x_i{}^{CAM}, y_i{}^{CAM}, z_i{}^{CAM}, 1]^T \quad 4.6$$

Equation 4.7 is extended to transform the position vector of the centre of the marker from [CAM] with respect to [RB].

$\boldsymbol{P}_{\boldsymbol{i}_{exact}}^{\boldsymbol{RB}}$ is computed for all the four (i=1,..,4) markers. Note that, in vector, $\boldsymbol{P}_{\boldsymbol{i}_{exact}}^{\boldsymbol{RB}}$, $z_i{}^{CAM}$ is still unknown and $x_i{}^{\mathrm{CAM}}$ and $y_i{}^{\mathrm{CAM}}$ are functions of $z_i{}^{CAM}$.

$$\boldsymbol{P}_{\boldsymbol{i}_{exact}}^{\boldsymbol{RB}} = \boldsymbol{T}_{\boldsymbol{RP}}^{\boldsymbol{RB}} \ \boldsymbol{T}_{\boldsymbol{CAM}}^{\boldsymbol{RP}} \boldsymbol{P_i}^{\boldsymbol{CAM}} \quad 4.7$$

Where:

$\boldsymbol{T}_{\boldsymbol{CAM}}^{\boldsymbol{RP}}$ is the transformation matrix of [CAM] w.r.t robot platform coordinate system, [RP] attached at the platform of the robot.

$\boldsymbol{T}_{\boldsymbol{RP}}^{\boldsymbol{RB}}$ is the transformation matrix between [RP] and [RB]

$\boldsymbol{P}_{\boldsymbol{i}_{exact}}^{\boldsymbol{RB}}$ is a position vector representing the exact coordinates of the centre of the marker, *i* with respect to [RB]. Unlike equation 4.1, equation 4.7 will give the exact coordinates of the markers with respect to [RB] after finding the values of $\mathrm{z}_i{}^{\mathrm{CAM}}$.

For measurement of each marker, there is a unique transformation matrix. i.e. $\boldsymbol{T}_{\boldsymbol{RP}}^{\boldsymbol{RB}}$ which is an Inverse Kinematic Solution of the robot.

Transformation of [CAM] with respect to [RP], $\mathbf{T}_{\mathbf{CAM}}^{\mathbf{RP}}$, is a rigid transformation since the camera is rigidly mounted on the platform of the robot. Thus, establishing $\boldsymbol{T}_{\boldsymbol{CAM}}^{\boldsymbol{RP}}$ is a one-time procedure (discussed later). The coordinates of the centre of all the four markers with respect to [RB] are obtained using equation 4.7. However, the vector $\boldsymbol{P}_{\boldsymbol{i}_{exact}}^{\boldsymbol{RB}}$ is in terms of $z_i{}^{\mathrm{CAM}}$ which is unknown. The invariant marker distances are utilised to calculate $z_i{}^{\mathrm{CAM}}$. The distances between markers are already measured in the image space. By equating the norms

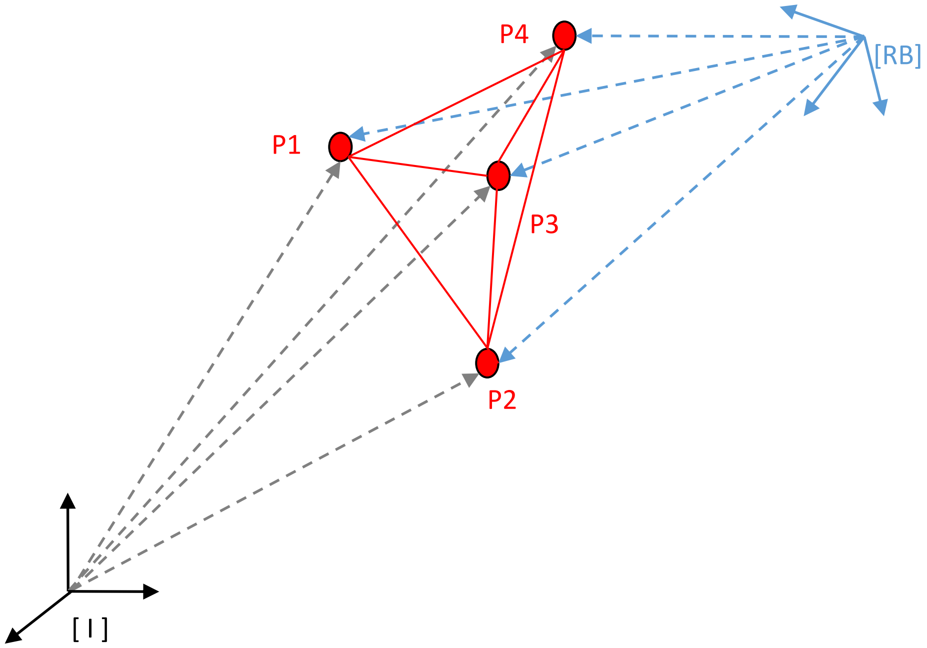

Figure 4.11: Equating the distance between corresponding markers to find the depth of the markers

of corresponding vectors in the [I] and the real patient space [RB], values of $z_i{}^{CAM}$ are determined (refer figure 4.11 and equation 4.8). The depth of one of the markers is also required to fully solve the set of equations 4.8 thus, it is measured using laser sensor attached at the platform of the robot

$$\left\| \boldsymbol{P}_{i\,exact}^{RB} - \boldsymbol{P}_{j\,exact}^{RB} \right\| = \left\| \boldsymbol{P_i}^{\prime} - \boldsymbol{P_j}^{\prime} \right\| \; for\ [(i\ ,j) = (1, 2), (2, 3), (3, 4), (4, 1)] \qquad 4.8$$

Where, $\boldsymbol{P}_{i\,exact}^{RB}$ and $\boldsymbol{P_i}^{\prime}$are the position vectors of the centre of the i^{th} markers with respect to [RB] and [I] respectively.

$\boldsymbol{P}_{j\,exact}^{RB}$and $\boldsymbol{P_j}^{\prime}$are the position vector of the centre of the j^{th} markers with respect to [RB] and [I] respectively. The set of Equations 4.8 are solved to obtain $z_i{}^{CAM}$.

Note that, the position of vectors of the centre of the four markers are measured in the [I], $\boldsymbol{P_i}^{\boldsymbol{I}}$.The order in which the markers are selected and measured in the [I] is imitated by the robot to localize and measure the corresponding markers in the real patient space. Thus, the correspondence between the markers is established since the localization algorithm uses equation 4.1 to locate the markers. The transformation matrix which relates [I] and [RB] is computed as follows:

$$[\boldsymbol{P_1}^{\boldsymbol{RB}}.\boldsymbol{P_2}^{\boldsymbol{RB}}.\boldsymbol{P_3}^{\boldsymbol{RB}}.\boldsymbol{P_4}^{\boldsymbol{RB}}] \quad = \quad \boldsymbol{T_I^{RB}}.[\boldsymbol{P_1}^{\boldsymbol{I}}.\boldsymbol{P_2}^{\boldsymbol{I}}.\boldsymbol{P_3}^{\boldsymbol{I}}.\boldsymbol{P_4}^{\boldsymbol{I}}] \qquad 4.9$$

The matrix at the left and the right-hand side of equation 4.9 contains the coordinates of the four measured markers centres in the real patient space [RB] and corresponding markers in the [I] respectively. Using equation 4.9, the transformation between [I] and [RB], $\mathbf{T_I^{RB}}$ is determined. Now, coordinates of any point can be transformed from the [I] to the real patient space using the homogenous transformation matrix obtained by equation 4.9. The method is validated for three standard poses of the phantom (discussed in chapter 6).

Computation of Transformation of [CAM] with respect to [RP]:

As already discussed, the transformation of [CAM] with respect to [RP], $\boldsymbol{T_{CAM}^{RP}}$, is a rigid transformation, since the camera is rigidly mounted on the platform of the robot. The one-time procedure to find the extrinsic properties of the camera is done with the checkerboard and coordinate measuring machine (CMM). The extrinsic properties of camera are nothing but the position and orientation of the camera coordinate system [CAM] with respect to the robot platform coordinate system [RP]. $\boldsymbol{T_{CAM}^{CHK}}$, [CAM] with respect to the checkerboard, [CHK] is obtained using pose estimation algorithm provided in the OpenCV [120], [121].

Further $\boldsymbol{T}_{CHK}^{Block}$ and $\boldsymbol{T}_{Block}^{RP}$ are obtained by attaching a checkerboard of size 10 mm x 7 mm on a standard block (see figure 4.12 and figure 4.13).

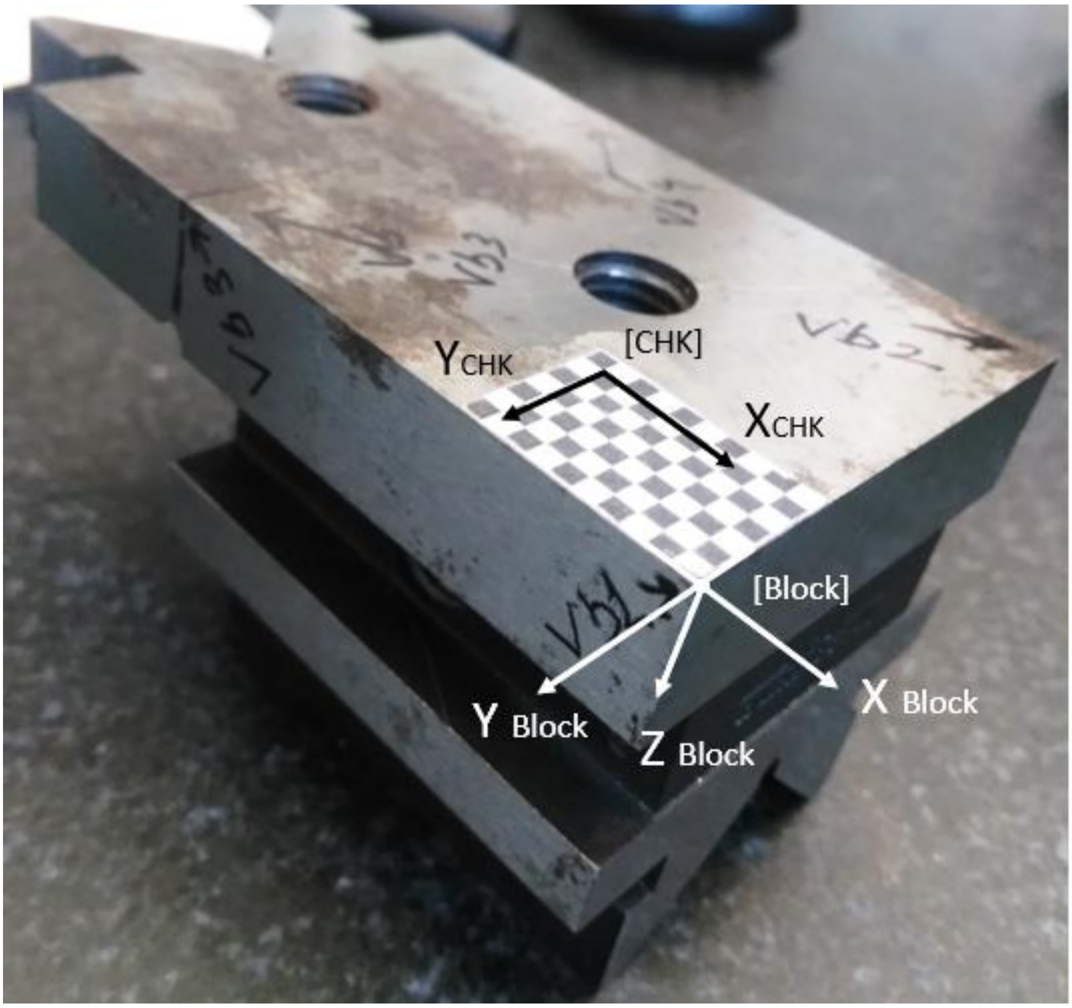

Figure 4.12: Zoomed view of the block with attached small checkerboard

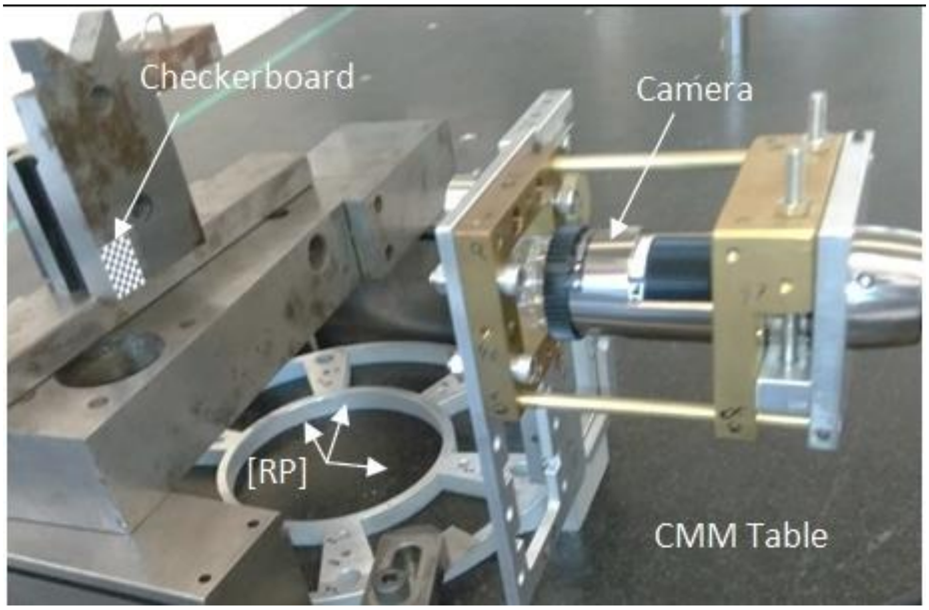

Figure 4.13: Onetime setup to find $\boldsymbol{T}_{CAM}^{RP}$ using CMM

Each square of the checkerboard is 1mm x 1mm. The checkerboard is fixed on the standard reference block such that, the relationship between the checkerboard coordinate system and block coordinate system is defined, ($\boldsymbol{T}_{CHK}^{Block}$). The block coordinate system is measured, with respect to the [RP], using high precision Coordinate Measuring Machine (CMM) (to establish, $\boldsymbol{T}_{Block}^{RP}$**).** Equation 4.10 is used to find the $\boldsymbol{T}_{CAM}^{RP}$.

$$\boldsymbol{T}_{CAM}^{RP} = \boldsymbol{T}_{Block}^{RP}\, \boldsymbol{T}_{CHK}^{Block}\, \boldsymbol{T}_{CAM}^{CHK} \qquad 4.10$$

4.3 Conclusions

A method has been developed to automate the neuro-registration process. The data extracted from the medical scan of the patient and the preoperative planning about patient posturing is used to develop a method to navigate to the markers prior to the actual neuro-registration. The patient is successfully registered with respect to the robot using the above method. After successful neuro-registration the overall accuracy of the robot-based neurosurgery is considerably improved. The other benefits of the above method are: eliminates line of sight problem, no extra device is required for neuro-registration leading to low foot print in OT, less time for registration, reduced human error and low cost.

CHAPTER V

Robust Marker Detection and High Precision Measurement for Real-Time Anatomical Registration using Taguchi Method[†]

5.1 Introduction

One of the major steps in autonomous neuro-registration was the measurement of coordinates of the reference points on the real markers on real patient space (anatomical space). Therefore, the detection of the marker and the measurement should be feasible, accurate, fast and reliable,

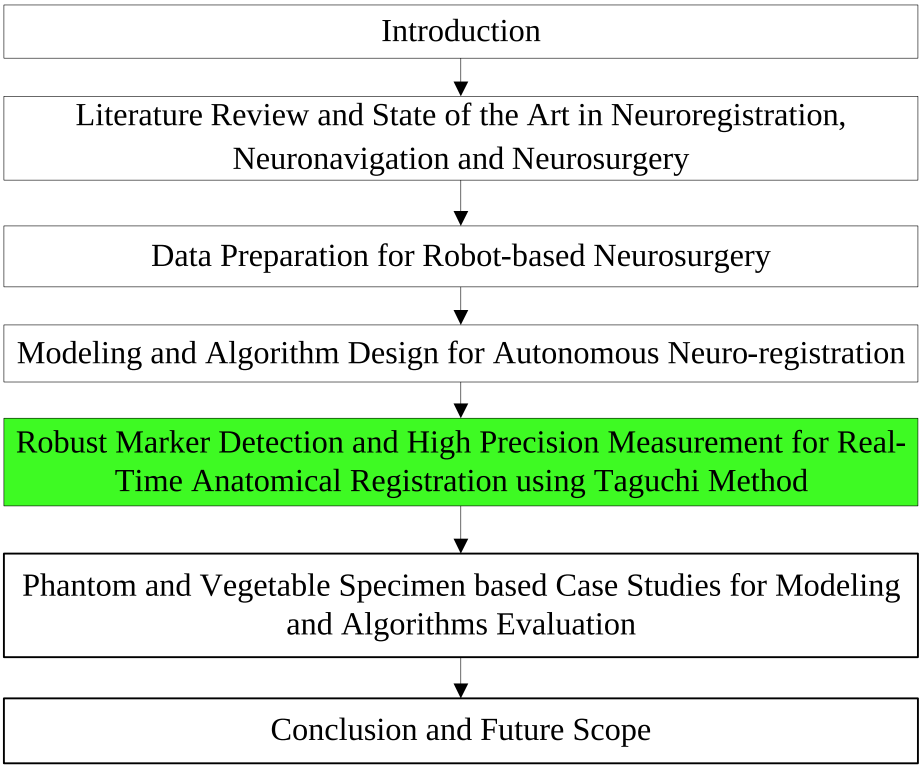

Figure 5.1: The flow of chapters and the importance and robust marker detection and coordinate measurement algorithm for the successful autonomous neuro-registration.

This chapter on robust marker detection and coordinate measurement algorithm shown in figure 5.1 describes steps to achieve the accuracy and reliability objectives. The robust method developed in the chapter is used on the case studies described in next chapter

[†] "Robust Marker Detection and High Precision Measurement for Anatomical Registration using Taguchi Method", Kaushik A, Dwarakanath TA, Bhutani G, International Journal of Medical Robotics and Computer Assisted Surgery ,Wiley. https://doi.org/10.1002/rcs.2102

As already discussed in the previous chapter, the coordinates of reference points at the markers are measured either manually or autonomously in medical image space. In real patient space, the markers are generally measured manually. Very few researchers have proposed the hands-free or autonomous measurement of the markers [78], [122], [123] in real patient space. For successful autonomous registration, the coordinates of the reference points have to be measured each time accurately with least pre-conditions. One of the major steps of the autonomous registration (detection of the markers and measurement of the coordinates of the reference points on the markers) in real patient space is subjected to various unavoidable and unpredictable conditions like uneven lighting, unpredictable orientations of the markers, unknown background of the markers, composite color contrasts and surface distortions of the markers. Due to these uncontrollable factors (noise factors), there are chances that the marker detection can be inconsistent or fail in the given working ambiance in the Operation Theatre (OT). Even different patient, lighting condition and set of new markers can cause failures in detection and measurement, and it is challenging to pinpoint the single cause for the failure. The different patient refers to the changes in the scalp skin tone of each patient, such uncertainties are considerably reduced if the choice of marker with background is made. This chapter presents the robust and real-time algorithm for the marker detection and measurement of the coordinates of the reference point on the marker. The algorithm is developed by using Taguchi method for robot-based autonomous registration. The Taguchi method[124][41] is one of the most versatile statistical techniques used in robust design and quality engineering to improve the process or product by reducing the variance even in the presence of noise factors[42]. Several researchers have applied the Taguchi method in Engineering[45], [47], Biotechnology[48], [49] and Marketing/advertising[51]. All of the above research dealt with the offline processes wherein real-time was not a consideration. During the marker detection and measurement process the factors which cannot be controlled are called noise factors, and the ones that are controllable are called control factors. Each control factor can have multiple levels. The Taguchi method is selected to find the best level of control factor values in real-time for each marker under the presence of several noise factors. Thus, the process is robust to the noise factors. The method is extensively used in problems involving subjective parameters, for example the method used in qualitative analysis. The Taguchi method computes the signal to noise ratio (S/N ratio) as an objective function to optimize control factors levels for the marker detection and coordinate measurement. The method uses a well-planned orthogonal array (OA) which provides equally balanced minimum tests. In this chapter, tests refer to the number of runs conducted in accordance with the OA that is designed. For each test of OA, S/N ratio is computed. After computing the S/N ratio corresponding to all the tests of the OA, Taguchi method is applied to optimize the S/N ratio. The noise factors, the control factors, the control factor levels and Orthogonal Array (OA) are explained in detail in the subsequent sections. The S/N ratio can be Larger-the-better, Smaller-the-better or Nominal-the-best, based on the type of objective function. Larger-the-better can be selected to maximize the objective function, i.e. profit and efficiency, etc. On the contrary, Smaller-the-better can be picked to minimize the objective function, i.e. cost, defect, wastage and time etc. Nominal-the-best quality characteristics can be chosen if a particular value is the utmost desire. The aim is to, first detect the marker in the captured image. Fit the concentric (outer and inner) ellipses to the ring-shaped marker (ring is the most commonly used marker geometry). Measure its center (reference point) in the image taken by the camera in least time with very high probability of the success.

5.2 Methodology

The robot is sequenced to move in real patient space from one marker location to the next as per the sequence of the selection of the markers in the medical image space. The robot traverses toward the marker such that the field of view of the camera covers the first marker. The robot pauses to capture the image and initialize the algorithm (described in the later section of the chapter) to detect the marker and measure the coordinates of the center of the marker. The autonomous neuro-registration algorithm uses three coordinates of the position vector of the center point of the marker with respect to the robot base. Two out of three coordinates of the center of the marker would be precisely generated by the Taguchi method. The two coordinates of centre of all the participating markers would be passed to the autonomous neuro-registration algorithm. The third coordinate is generated by autonomous neuro-registration algorithm (as described in previous chapter). The image is captured by using a high-resolution digital camera attached to the robot platform. Dino-Lite Edge digital camera (Model no. AM7115MZTL) of size 10.5 cm (Height) x 3.2 cm (Diameter) has been used. The resolution is 5 MP, field of view is 19.6 mm x 15.6 mm, and the working distance is 150 mm at fixed 15x zoom. The type of markers is important; the data points of conventional two-dimensional markers used in computer vision would largely be missed and not be visible in CT/MRI scan. The three-dimensional radio-opaque, circular ring-shaped markers are commonly used in medical imaging for registration. Thus, conventional multimodality compatible ring-shaped markers are considered in this thesis. Moreover, circular markers have several advantages over other shapes[125].

Conventional radio-opaque markers are visible in all the imaging modalities and hence very commonly practiced worldwide. Even if the markers are well designed for medical imaging and computer vision applications, there are chances that the marker detection in the image captured by the camera can fail due to uncontrollable factors called noise factors.

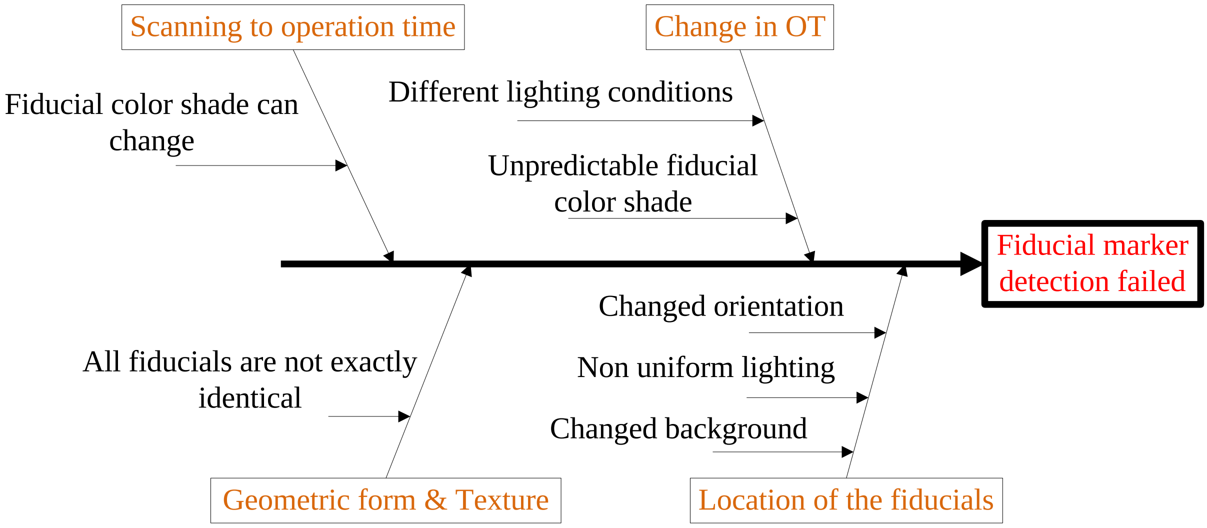

Figure 5.2: Cause and effect plot of the failure of the detection of markers

Figure 5.2 shows the cause and effect plot of the failure of marker detection and measurement. The brown text box indicates the causes of failure; the black text label shows the effects of causes, and the red text shows the outcome of causes and its effects. Scanning to operative time refers to the deterioration of markers from the time of CT/MRI scanning to the time of surgery. Different OT can lead to different lighting conditions and alter the color shades of the markers in the image. Geometric form and texture refer to the variations due to practical limitations related to the manufacturing the identical markers. Position and orientation (location on the scalp) of markers alter the uniformity of lighting. The effect of these factors can be seen in figure 5.2. All of these factors are called noise factors because they cannot be controlled.

Figure 5.3 (a) and figure 5.3 (b) show the affixing of the conventional ring-shaped radio-opaque markers.

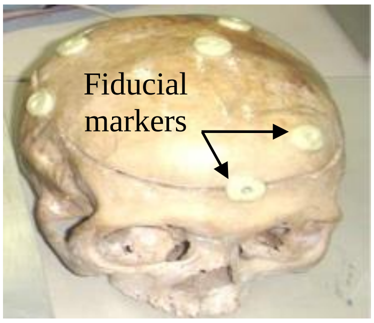

(a) Skull affixed with the markers

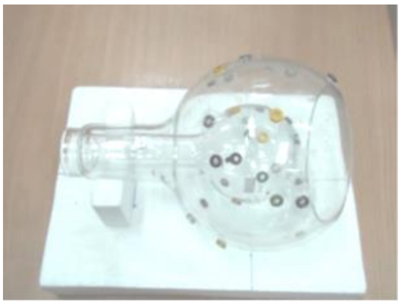

(b) Concentric spherical glass jar phantom affixed with ring-shaped markers

Figure 5.3: Phantoms with attached radio opaque markers

Figure 5.3 (b) shows the concentric glass jar phantom. The markers on the inside jar serve as the target points while the markers on the outer jar are accessible markers for registration.

Figure 5.4 shows instant of the surgical robot approaching the markers to capture the images for detection and measurement of the reference points on the markers. Note that the markers have different orientations depending on the location they are affixed on the scalp. Due to the view angle of the camera mounted on the robot and orientation of markers on the scalp, there is non-uniform lighting, shadow, and glare.

Also, the circular marker appears as the elliptical at the imaging plane of the camera. In a particular image, the aim is to detect the marker and measure the coordinates of the center of the marker (reference point) under any conditions of OT ambiance, state of markers configurations without fail in the least time.

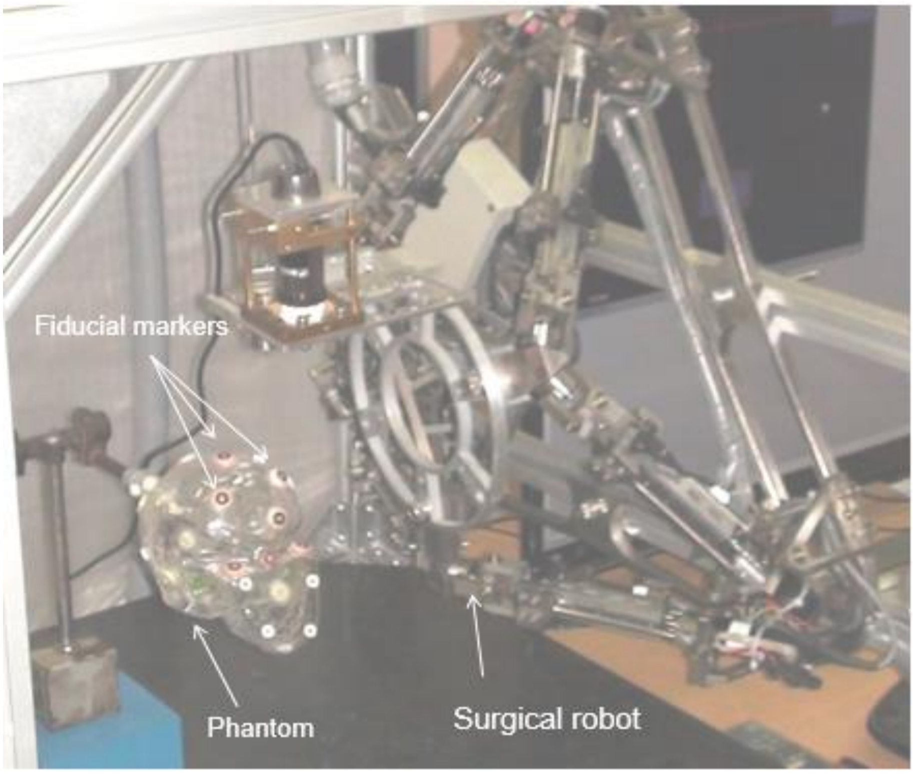

Figure 5.4: An instant of surgical robot motion sequence, while capturing the images of the markers.

Figure 5.5 (a) and figure 5.5 (b) show how the color shade of marker is changed due to glare, and as a consequence, only color-range based marker detection algorithm would fail under such condition. Figure 5.5 (c, d, e) show that the circular ring-shape of the marker has changed to elliptical shape at the imaging plane of the camera because of non-orthographic projection. Note that the projection will be different for each marker based on their relative orientation at the skull. Distortion in color and surface within the timespan of CT/MRI scanning to surgery is shown in figure 5.5 (e).

The method implements a series of image processing algorithms to detect the marker in the captured image and measure coordinates of reference point on the detected marker. The OpenCV[37], [39] (Open-source computer vision library) functions that are used in the algorithm are Template matching, color image conversion to grayscale image, image thresholding, histogram equalization, morphological transformation (closing), canny edge detection, find contour, and fit ellipse.

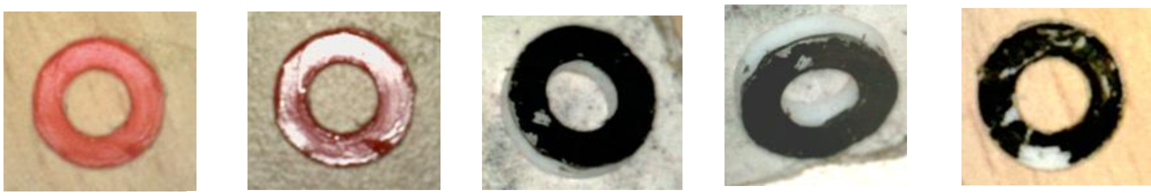

(a) Red color marker

(b) Due to glare shade of red color has changed

(c) Marker is randomly oriented

(d) Marker randomly oriented

(e) The distorted surface of the marker

Figure 5.5: Common noise factors that can fail the detection of marker and measurement of coordinates of the reference points at the marker

Two image processing pipelines are formulated, one each for Marker Detection and Coordinate Measurement. As name indicates, the first pipeline consists of series of image processing algorithm to detect the marker. The second pipeline is responsible for the measurement of coordinates of the marker. The second pipeline have some additional algorithms along with the algorithms used in the first pipeline. Due to the uncontrollable factors (noise factors) discussed earlier, the detection of marker (first pipeline) and measurement of coordinates (second pipeline) are sensitive to the various image processing parameters, i.e. Marker Template, Marker Threshold, Marker Contrast and Image Kernel. Taguchi method considers these controllable image processing parameters as control factors. The discrete range of these control factors are called levels. The number of trials conducted in accordance with the OA are called tests. A robust marker detection and measurement process is designed by careful selection of control factors and optimizing the levels of control factors. Note that the optimization of levels of the control factor varies for different markers and different working ambiance. Thus, the algorithm should be capable of finding the levels in real-time. Taguchi method computes best levels of the control factors for the Marker

Detection by maximizing the template matching. Since the orientation of the marker at the scalp and the working ambiance of the OT is same for both the pipelines. Thus, optimal levels of Marker Template and Marker Contrast obtained for Marker Detection pipeline are used for the Coordinate Measurement pipeline also. Taguchi Method for Coordinate Measurement would optimize the levels of remaining two control factors. Finally, Coordinate Measurement Pipeline is applied with the updated levels of control factors, obtained by second method. The flow diagram of the Taguchi Method for Marker Detection and Taguchi Method for Coordinate Measurement is shown in figure 5.6. Table 5.1 shows four control factors, and each has five levels; thus, full factorial design (maximum tests) will have (5^4), 625 tests. A large number of tests are impractical for real-time registration and measurement.

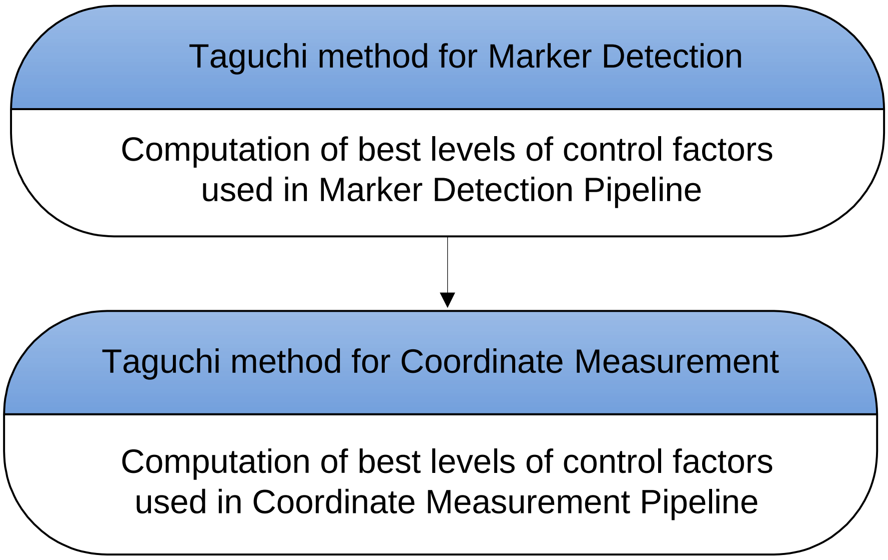

Figure 5.6: Flowchart of Taguchi Method for Marker Detection and Taguchi Method for Coordinate Measurement

Intuitively, it appears that far fewer tests are sufficient to capture the influence of control factors and their levels. It is difficult to resolve the number of tests, which of the tests, and the order of the tests. In table 5.1, the Marker Template is one of the control factors with five levels. The level of Marker Template is the discrete orientation out of infinite possible orientations of the marker. The image of the marker should be close to one of the orientations (level).

Table 5.1: Initial control factors and their levels

Control factors	Level 1	Level 2	Level 3	Level 4	Level 5
Marker Template	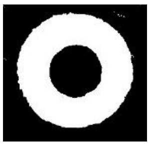 1	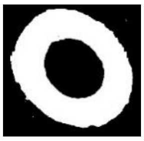 2	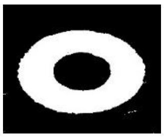 3	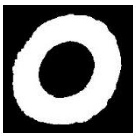 4	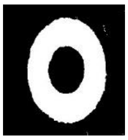 5
Marker Threshold	20	40	60	80	100
Marker Contrast	No	Yes	No	Yes	No
Image Kernel	1x1	2x2	3x3	4x4	5x5

In the case studies, marker top surface as black and background as white is considered. Thus, the Marker Threshold is chosen as one of the control factors. It is discretized into five levels of the threshold from 20 to 100 to segment the marker from the background image. It can be noted that for some other color marker, the levels of Marker Threshold can be set differently. Some of the image processing algorithms like histogram equalization are beneficial in some situations, while in some other cases, they can even make it hard to detect the markers. Thus, Marker Contrast is chosen as the control factor, with only two levels (alternatives). The last control factor is Image Kernel. It is the size of the structuring element of the closing morphological operation. The closing operation is responsible for filling the unwanted patches developed in the marker image after image thresholding operation. A broader discrete range of Image Kernel is selected from 1x1 to 5x5 pixel matrix. Table 5.2 shows the Taguchi based standard L_{25} (5^4) Orthogonal Array (OA), used to resolve the minimum number, the type, and the order of the tests. Standard OA can be found in Taguchi and Konishi[41], [124] and comprehensively discussed in Madhav S Phadke[42].

Table 5.2: Standard L_{25} (5^4) Orthogonal Array (OA) for initial tests based on table 5.1

Test no.	Marker Template	Marker Threshold	Marker Contrast	Image Kernel
1	1	20	No	1x1
2	1	40	Yes	2x2
3	1	60	No	3x3
4	1	80	Yes	4x4
5	1	100	No	5x5
6	2	20	Yes	3x3
7	2	40	No	4x4
8	2	60	Yes	5x5
9	2	80	No	1x1
10	2	100	No	2x2
11	3	20	No	5x5
12	3	40	Yes	1x1
13	3	60	No	2x2
14	3	80	No	3x3
15	3	100	Yes	4x4
16	4	20	Yes	2x2
17	4	40	No	3x3
18	4	60	No	4x4
19	4	80	Yes	5x5
20	4	100	No	1x1
21	5	20	No	4x4
22	5	40	No	5x5
23	5	60	Yes	1x1
24	5	80	No	2x2
25	5	100	Yes	3x3

The OA can also be obtained from statistical software like Minitab[126] and qualityTools package in R software[127]. The algorithm conducts all 25 tests of OA and records the maximum values for template matching and computes S/N ratio (Larger-the-better) to maximize the value of template matching. Using the Taguchi method, the best levels setting of the control factors were determined. The Optimum Initial Level for Threshold (OIL_T) and Optimum Initial Level for Kernel (OIL_K) would be used by the second method. After the determination of the optimum level for each control factor given in table 5.1. The Taguchi method is recursively applied to a reduced number of control factors with more precise levels. The purpose of recursively applying the Taguchi method is to maximize the detection of the number of predefined ellipses (in the detected marker) by maximizing the S/N ratio. The purpose of maximizing ellipse detection is to increase the probability of always getting real concentric ellipse. The false ellipses that appear due to maximization would get filtered on the basis of geometry and size of the markers (discussed later). The reduced control factors with their levels and new OA are shown in table 5.3 and table 5.4, respectively. Table 5.3 and table 5.4, standard L_{18} (6^1 x 3^1) orthogonal array (based on table 5.3), are designed in real-time by the algorithm. Table 5.3 and table 5.4 would be unique for each marker, whereas initial control factors and their settings and tests (table 5.1 and table 5.2) are the same for all the markers. The S/N ratio (Larger-the-better)[42] is computed using equation 5.1.

$$S/N = -10\, log_{10}[\sum(1/y^2)/n \tag{5.1}$$

Where,

y is the observation of the test (maximum value for template matching)

n is the number of observations per test

Table 5.3: Reduced number of control factors with more precise levels

Control factors	Level 1	Level 2	Level 3	Level 4	Level 5	Level 6
Marker Threshold	OIL_T -15	OIL_T -10	OIL_T -5	OIL_T	OIL_T +5	OIL_T +10
Image Kernel	OIL_K -1	OIL_K	OIL_K +1	--	--	--

Table 5.3 and table 5.4 belong to the Taguchi Method for Coordinate Measurement. Table 5.3 shows that the number of control factors has reduced to two. i.e., Marker Threshold and Image Kernel. Since the marker is already detected by the first method, the second method requires a more precise range of levels of control factors. The levels of Marker Threshold and Image Kernel are computed from OIL_T and OIL_K (computed by the first method). Table

5.3 shows the computation of precise levels by OIL_T and OIL_K. Table 5.4 shows standard L_{18} OA based on table 5.3. Figure 5.7 shows the complete flow chart of the Taguchi Method for Marker Detection and Taguchi Method for Coordinate Measurement with a series of image processing functions in pipelines.

Table 5.4: Final standard L_{18} (6^1 x 3^1) OA based on initial tests

Test no.	Marker Threshold	Marker Kernel
1	OIL_T -15	1x1
2	OIL_T -15	2x2
3	OIL_T -15	3x3
4	OIL_T -10	1x1
5	OIL_T -10	2x2
6	OIL_T -10	3x3
7	OIL_T -5	1x1
8	OIL_T -5	2x2
9	OIL_T -5	3x3
10	OIL_T	1x1
11	OIL_T	2x2
12	OIL_T	3x3
13	OIL_T +5	1x1
14	OIL_T +5	2x2
15	OIL_T +5	3x3
16	OIL_T +10	1x1
17	OIL_T +10	2x2
18	OIL_T +10	3x3

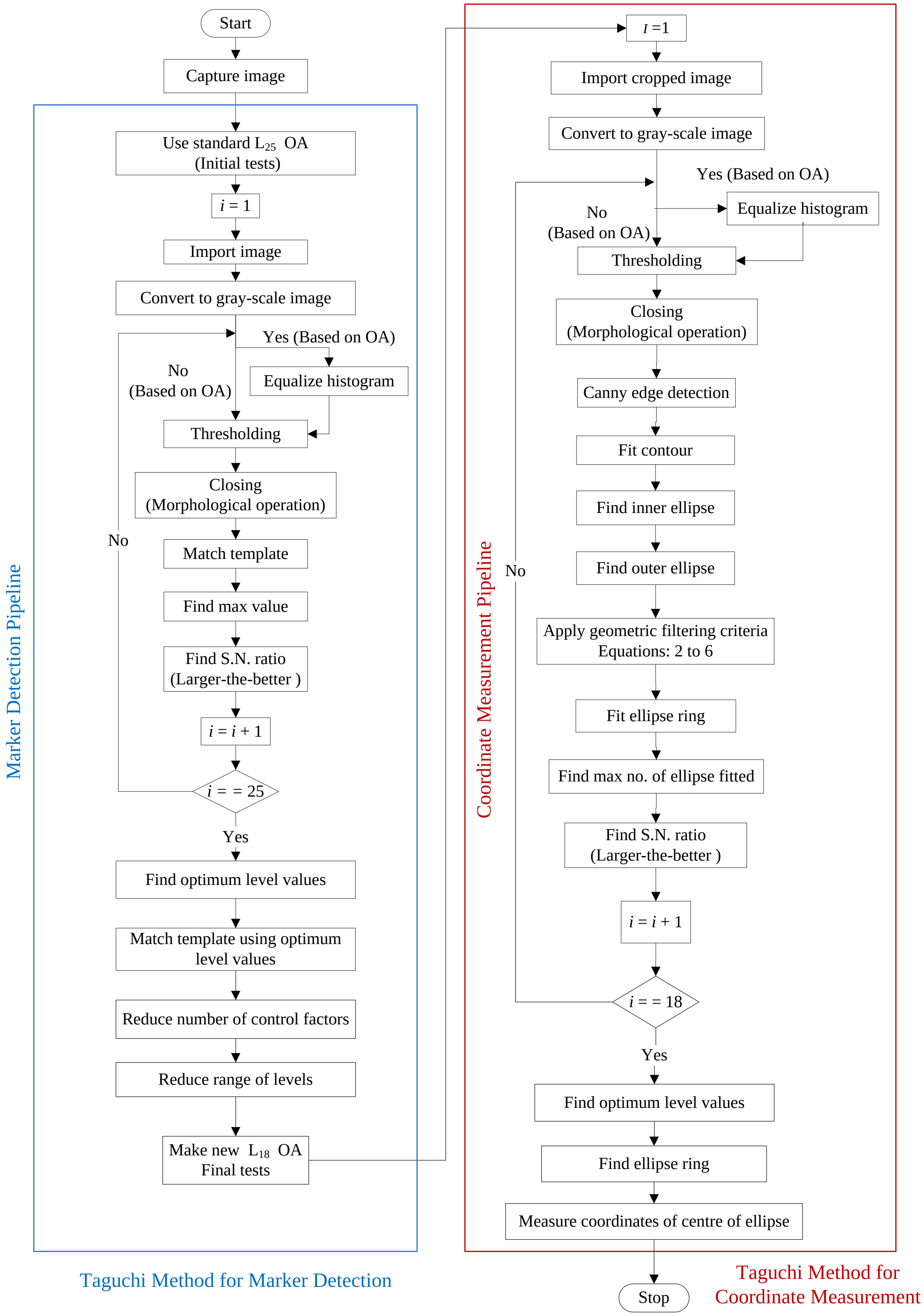

Figure 5.7: Complete flow chart applying Taguchi Method twice in sequence for Marker Detection and Coordinate Measurement with associated pipelines

5.3 Results and discussions

In this section, the detailed case study of one of the marker detection and measurement of the coordinates of the center of the marker is presented. The results of each stage are discussed in detail. Results of two more case studies are presented to validate the consistency in detection and measurement in different working ambiance, lighting conditions, and other noise factors. The optimum level settings of the control factors will be different and will be designed in real-time by the method for each case study. First, the Taguchi Method for Marker Detection applies a series of image processing algorithms with control factors levels based on the tests (given in table 5.5) and measure the maximum value of template matching. Subsequently, computes the corresponding S/N ratio using equation 5.1 to maximize the template matching.

For all the markers, the initial control factors, their levels, and initial tests remain the same (shown in table 5.1 and table 5.2). Note that the values in the column, "maximum value of Template Matching" in table 5.5 is directly proportional to the percentage matching of the template with the image taken by the camera. Illustrating the first row, 56.8 % template matching with the S/N ratio of - 4.898 is possible if the parameters of Marker Templates are 1, the Marker Threshold to be 20, with no Marker Contrast and 1x1 Image Kernel are selected.

Table 5.6 shows the response table for S/N ratio and the mean S/N ratio values for each control factor for each level. -4.629 is the mean S/N ratio of control factor, "Marker Template" for level 1. Similarly, -4.450 is the mean S/N ratio for the control factor, "Marker Threshold" for level 3. In table 5.6, Δ indicates the difference between the maximum and minimum mean of S/N ratios for each control factor.

Table 5.5: L_{25} OA Initial tests

Test No.	Marker Template	Marker Threshold	Marker Contrast	Image Kernel	Maximum value of Template Matching	S/N ratio (Larger-the-better)
1	1	20	No	1x1	0.568	-4.898
2	1	40	Yes	2x2	0.604	-4.369
3	1	60	No	3x3	0.627	-4.053
4	1	80	Yes	4x4	0.529	-5.526
5	1	100	No	5x5	0.609	-4.296
6	2	20	Yes	3x3	0.649	-3.750
7	2	40	No	4x4	0.644	-3.820
8	2	60	Yes	5x5	0.613	-4.248
9	2	80	No	1x1	0.645	-3.800
10	2	100	No	2x2	0.653	-3.693
11	3	20	No	5x5	0.689	-3.225
12	3	40	Yes	1x1	0.707	-3.008
13	3	60	No	2x2	0.700	-3.095
14	3	80	No	3x3	0.715	-2.903
15	3	100	Yes	4x4	0.580	-4.717
16	4	20	Yes	2x2	0.501	-5.994
17	4	40	No	3x3	0.493	-6.133
18	4	60	No	4x4	0.505	-5.933
19	4	80	Yes	5x5	0.474	-6.474
20	4	100	No	1x1	0.508	-5.877
21	5	20	No	4x4	0.568	-4.902
22	5	40	No	5x5	0.585	-4.643
23	5	60	Yes	1x1	0.567	-4.918
24	5	80	No	2x2	0.588	-4.610
25	5	100	Yes	3x3	0.526	-5.567

Figure 5.8 shows the corresponding main effect plot for S/N ratios. The last row of table 5.6 and figure 5.8 shows the influence of control factors on the mean of S/N ratios. It can be seen that Marker Template has the highest impact, followed by Image Kernel and Marker Contrast, the least being the Marker Threshold. Since the objective here is to maximize the template matching, thus based on the response graph, the recommended control factor levels are shown in table 5.7.

Table 5.6: Response table for Signal to Noise Ratios (Larger-the-better)

Level	Marker Template	Marker Threshold	Marker Contrast	Image Kernel
1	-4.629	-4.554	-4.393	-4.501
2	-3.863	-4.395	-4.858	-4.353
3	-3.390	-4.450	---	-4.482
4	-6.083	-4.663	---	-4.980
5	-4.928	-4.830	---	-4.578
Δ	2.693	0.435	0.465	0.627
Rank	1	4	3	2

Figure 5.9 shows template matching, using optimized levels of the control factors based on table 5.7 and figure 5.8. Figure 5.9 also shows the sequence of image processing operations (Marker Detection Pipeline) to maximize the template matching. The various image processing operations are conversion to grey-scale imaging, image thresholding the image, morphological closing operation, template matching, and crop image operation. The green box in figure 5.9(e) shows the detected marker.

Table 5.7: Recommended control factors levels with the corresponding S/N ratio to maximize template matching

Control factors	Best level	Corresponding S/N ratios
Marker Template	3 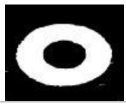	-3.390
Image Kernel	2 (2x2) (OIL_K)	-4.353
Marker Contrast	1 (No)	-4.393
Marker Threshold	2 (40) (OIL_T)	-4.395

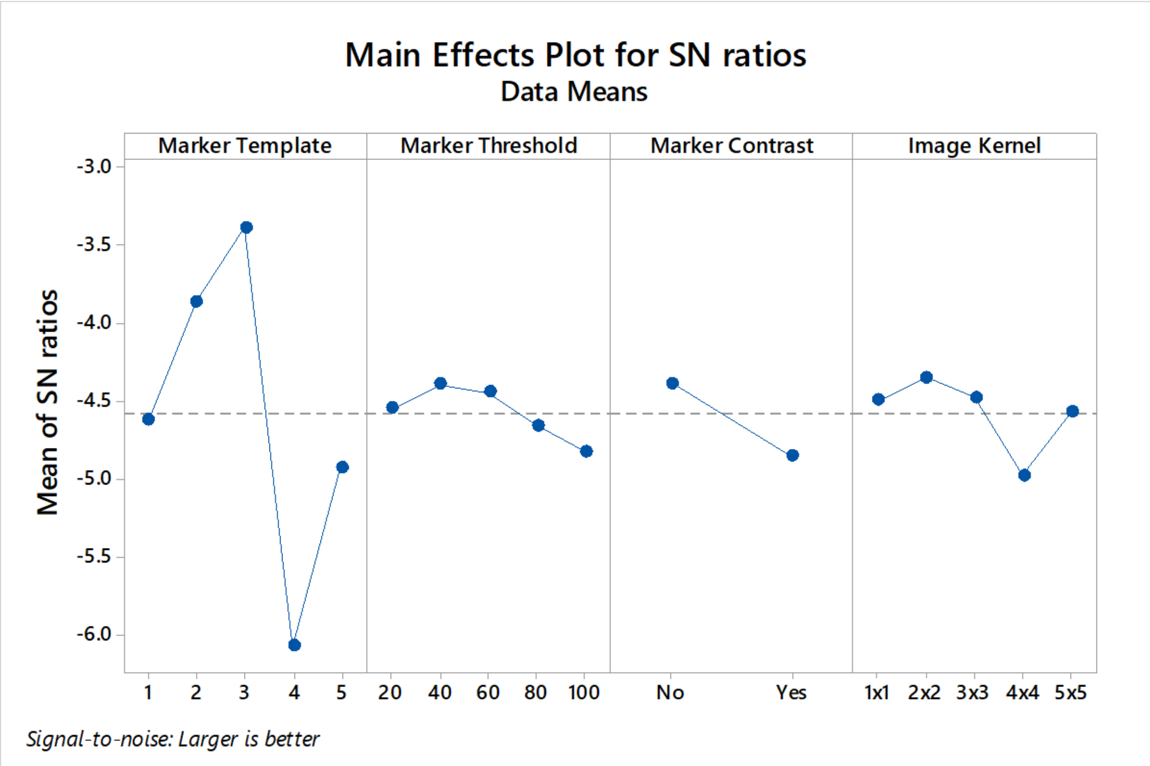

Figure 5.8 : Main Effect Plot for S/N ratio to maximize the template matching

(a) Captured image →

(b) Gray-scale image →

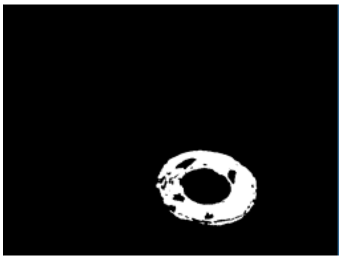

(c) Threshold image →

(d) Morphological operation→ (closing)

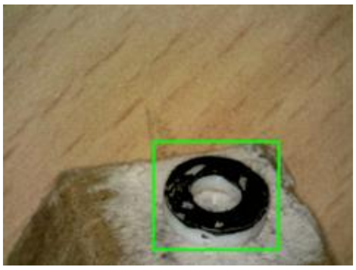

(e) Marker detected (Template matching)→

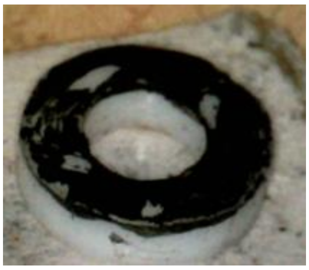

(f) Cropped image

Figure 5.9: Template matching using optimized levels of control factors based on initial tests

Once the marker is detected, the next stage is to refine the number of control factors and their levels to maximize the number of ellipse detection on the cropped image of the detected marker. For a particular marker, the orientation of marker at the scalp and ambient lighting condition will remain the same for the Taguchi Method for Coordinate Measurement. Thus, the best levels for Marker Template and Marker Contrast to maximize the template matching will remain the best levels for subsequent tests to maximize the number of ellipse detection. Hence the two can be removed from the list of control factors for the Taguchi Method for Coordinate Measurement. It can be noted that the Coordinate Measurement Pipeline involves fitting ellipses after canny edge detection and contour fitting; thus, these tests require more precise values of Marker Threshold and Image Kernel. Table 5.8 shows the remaining control factors and their more precise levels (levels with small intervals). The Optimum Initial Level for Threshold (OIL_T) was 40, and the Optimum Initial Level for Kernel (OIL_K) was 2x2 (see figure 5.8 and table 5.7) to maximize the template matching. Now for the Coordinate Measurement Pipeline, the new levels for remaining control factors, that is, Marker Threshold and Image kernel, have small intervals and are close to OIL_T and OIL_K based on table 5.3 and can be seen in table 5.8.

Table 5.8: Reduced number of control factors with more precise levels

Control factors	Level 1	Level 2	Level 3	Level 4	Level 5	Level 6
Marker Threshold	40-15 =25	40-10 =30	40-5=35	40	40 +5 =45	40+10 = 50
Image Kernel	1x1	2x2	3x3	--	--	--

Table 5.9 is a standard L_{18} Orthogonal Array (OA) based on the remaining control factors with more precise levels (table 5.8). Since the template is already matched, the marker is identified and cropped from the main image (refer figure 5.9(e) and figure 5.9(f)); thus, the objective of the Coordinate Measurement Pipeline is to maximize the number of ellipse detection in the cropped image. Therefore, the number of ellipses detected and corresponding

S/N ratio (Larger-the-better) are recorded for each test. The S/N ratio is again computed using equation 5.1. Table 5.10 and figure 5.10 shows the most influencing factors in decreasing order are Marker Threshold and Image Kernel. Based on table 5.10 and figure 5.10, the recommended final control factor levels for Marker Threshold and Image Kernel are given in table 5.11 with the corresponding S/N ratio. Thus, based on the Taguchi Method for Marker Detection and Taguchi Method for Coordinate Measurement, the final control factors levels are shown in table 5.12.

Table 5.9: L_{18} OA based on table 8 (Reduced control factors with more precise levels)

Test no.	Marker Threshold	Image Kernel	No. of ellipses detected	S. N. ratio (Larger-the-better)
1	25	1x1	2.000	6.021
2	25	2x2	4.000	9.542
3	25	3x3	2.000	6.021
4	30	1x1	1.000	0.000
5	30	2x2	1.000	0.000
6	30	3x3	1.000	0.000
7	35	1x1	4.000	9.542
8	35	2x2	1.000	0.000
9	35	3x3	1.000	0.000
10	40	1x1	4.000	9.542
11	40	2x2	1.000	0.000
12	40	3x3	1.000	0.000
13	45	1x1	4.000	9.542
14	45	2x2	4.000	9.542
15	45	3x3	4.000	9.542
16	50	1x1	4.000	9.542
17	50	2x2	4.000	9.542
18	50	3x3	4.000	9.542

Table 5.10: Response table for Signal to Noise Ratios (Larger-the-better)

Level	Marker Threshold	Image Kernel
1	7.194	7.365
2	0.000	4.771
3	3.181	4.184
4	3.181	---
5	9.542	---
6	9.54	---
Delta	9.541	3.180
Rank	1	2

Figures (a to f) in figure 5.11, figure 5.12 and figure 5.13 show the result of Marker Detection Pipeline and (figures g to i) show the result of the Coordinate Measurement Pipeline using optimized levels of control factors for three case studies.

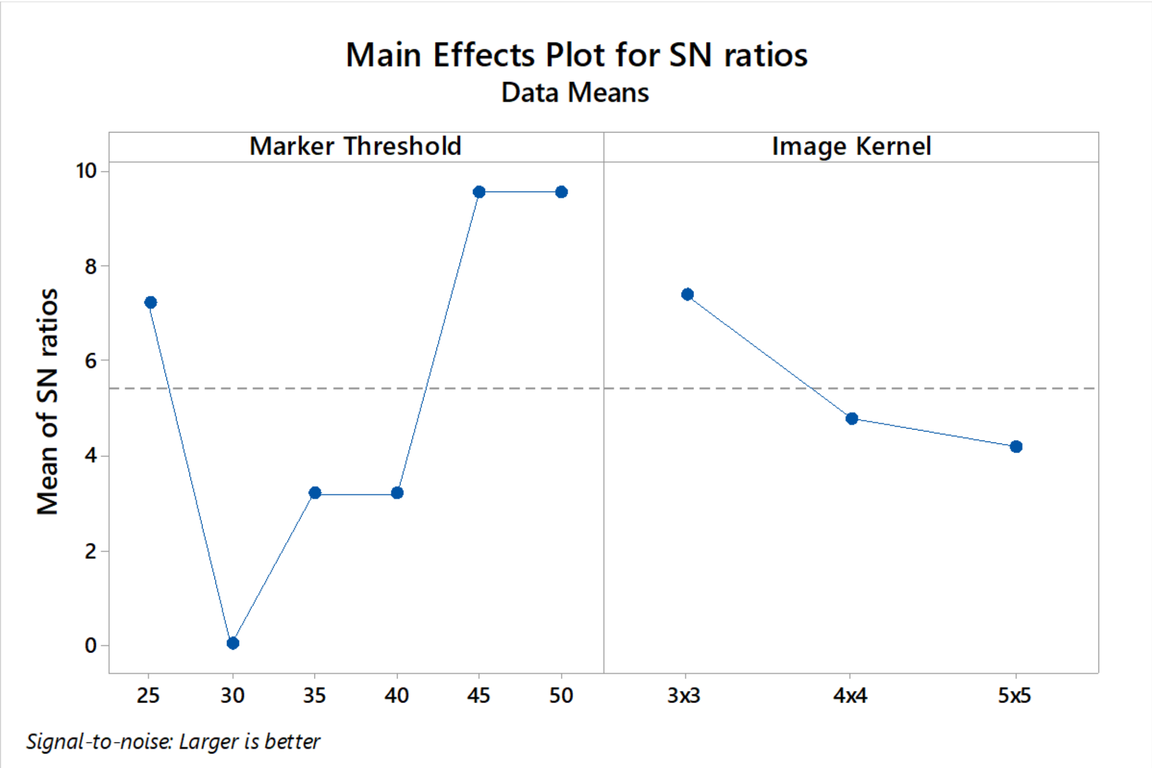

Figure 5.10: Main Effect Plot for S/N ratio to maximize the number of predefined ellipse detection (final tests)

Table 5.11: Recommended control factors levels with the corresponding S/N ratio to maximize the number of ellipse detection

Control factors	Best level	Corresponding S/N ratios
Marker Threshold	5 (45) and 6(50)	9.542
Image Kernel	1 (3x3)	7.365

Table 5.12: Final control factors levels

Control factors	Best level	Remark
Marker Template	3 	Initial phase tests
Marker Threshold	5(45) or 6(50)	Updated by second phase tests
Marker Contrast	1 (No)	Initial phase tests
Image Kernel	1 (3x3)	Updated by second phase tests

Figures (j to l) in figure 5.11, figure 5.12 and figure 5.13 shows the precise fitting of inner and outer ellipses to the cropped image of the detected marker. Since the dimensions of the marker are known, only ellipses that meet the filtering criteria given from Equation 5.2 to Equation 5.6 are fitted.

$$T_{e,mjr}^{min} \leq d_{e,mjr} \leq T_{e,mjr}^{max} \quad (5.2) \qquad T_{e,mnr}^{min} \leq d_{e,mnr} \leq T_{e,mnr}^{max} \quad (5.3)$$

$$\boldsymbol{c}_i = \boldsymbol{c}_o \pm \Delta \boldsymbol{T} \quad (5.4)$$

$$T_{ratio,mnr}^{min} \leq \frac{d_{o,mnr}}{d_{i,mnr}} \leq T_{ratio,mnr}^{max} \quad (5.5) \qquad T_{ratio,mjr}^{min} \leq \frac{d_{o,mjr}}{d_{i,mjr}} \leq T_{ratio,mjr}^{max} \quad (5.6)$$

Where:

$d_{e,mjr}$ and $d_{e,mnr}$ are the major and minor diameters of an ellipse for $e = i\ or\ o$, the first subscript, "i" specifies the inner ellipse, and the first subscript "o" represent outer ellipse diameter in pixels respectively.

$T_{e,mjr}^{min}$ and $T_{e,mjr}^{max}$ are the minimum and maximum tolerance limit of the major diameter of the ellipse in pixels, respectively, for $e = i$ and o.

$T_{e,mnr}^{min}$ and $T_{e,mnr}^{max}$ are the minimum and maximum tolerance limit of minor diameter of the ellipse in pixels, respectively, for $e = i$ and o.

$\boldsymbol{c}_i$, $\boldsymbol{c}_o$ and $\Delta\boldsymbol{T}$ are the vectors represents the center of the inner and outer ellipse and tolerance of the centers in pixels respectively

$T_{ratio,mnr}^{min}$ and $T_{ratio,mnr}^{max}$ are the minimum and maximum tolerance limits of the ratio of minor diameters of outer to inner ellipse respectively

$T_{ratio,mjr}^{min}$ and $T_{ratio,mjr}^{max}$ are the minimum and maximum tolerance limits of the ratio of major diameters of outer to inner ellipse, respectively. Note that the small contours (refer figure 5.11 (f) to (i)) produce due to distorted surface of the marker are filtered out by the algorithm using the above criteria for predefined ellipse fitting.

Results of case study 1

(a) Captured image → (b) Grayscale image → (c) Threshold image →

(d) Morphological operation→ (e) Marker detected → (f) Cropped image→

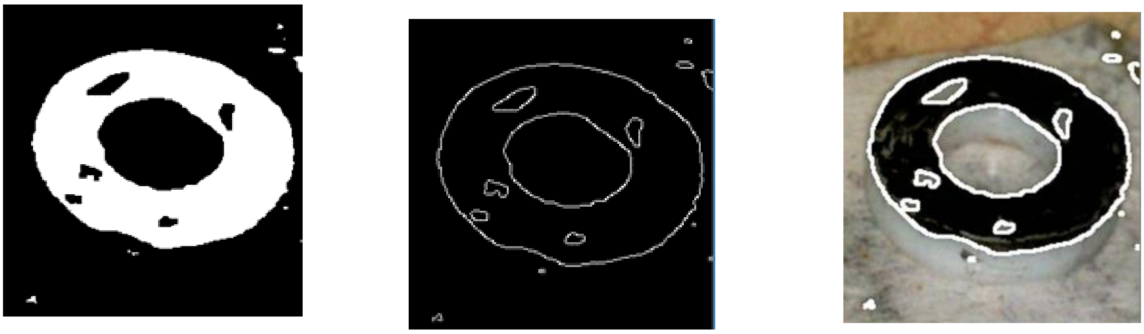

(g)Morphological operation→ (h) Canny threshold image→ (i) Contour detection→

(j) Inner ellipse fitting → (k) Outer ellipse fitting → (l) Ellipse ring fitting

Figure 5.11: Case study 1: Marker Detection and Coordinate Measurement

Results of case study 2

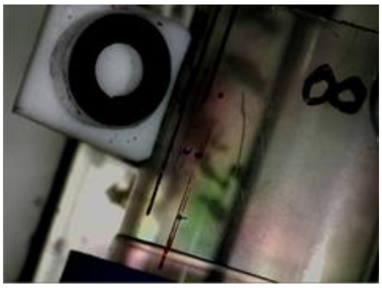

(a) Captured image →

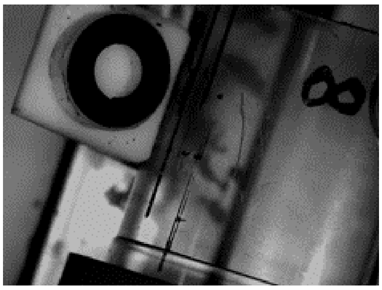

(b) Grayscale image →

(c) Threshold image →

(d) Morphological operation→ (closing)

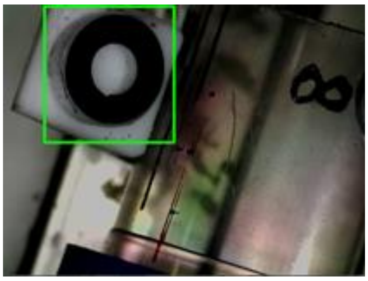

(e) Marker detected (Template matching)→

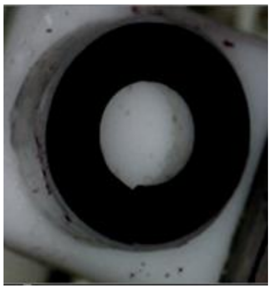

(f) Cropped image→

(g)Morphological operation→ (closing) on cropped image

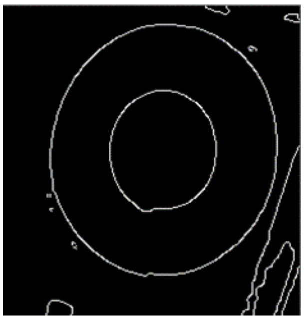

(h) Canny threshold image→

(i) Contour detection→

(j) Inner ellipse fitting →

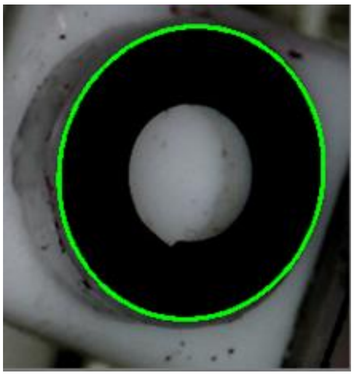

(k) Outer ellipse fitting →

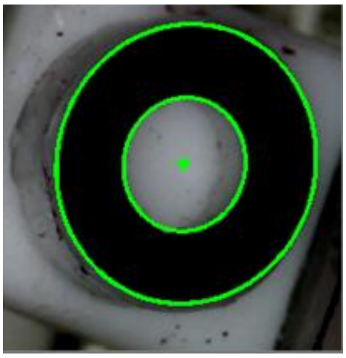

(l) Ellipse ring fitting

Figure 5.12: Case study 2: Marker Detection and Coordinate Measurement

Results of case study 3

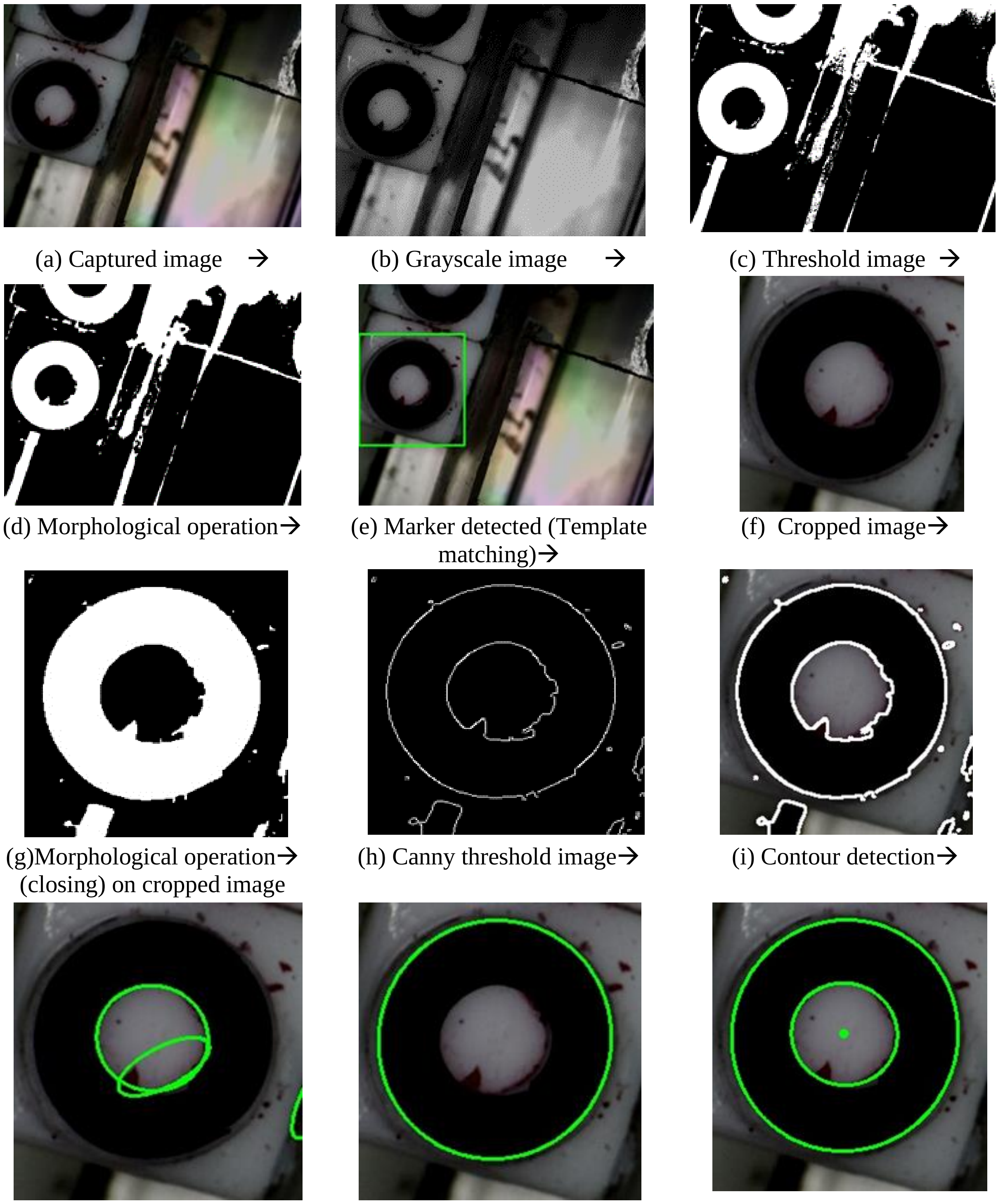

(a) Captured image →
(b) Grayscale image →
(c) Threshold image →
(d) Morphological operation→
(e) Marker detected (Template matching)→
(f) Cropped image→
(g)Morphological operation→ (closing) on cropped image
(h) Canny threshold image→
(i) Contour detection→
(j) Inner ellipse fitting →
(k) Outer ellipse fitting →
(l) Ellipse ring fitting

Figure 5.13: Case study 3: Marker Detection and Coordinate Measurement

The comparative performance in measuring the coordinates is benchmarked against the ImageJ software[128] (standard open-source image processing software). The standard software cannot detect the marker itself and only measure the center of the drawn ellipse given the distortion-free ellipse and under the pre-set condition of the ambiance. Figure 5.14 shows the measurement of coordinates of the center of all three markers using ImageJ software. Table 5.13 shows 2D Fiducial localization Error (FLE) in pixels unit.

The average execution time of the marker detection and coordinate measurement algorithm is found to be 1.37 seconds per marker using a conventional computer system with intel inside™ core i7 processor, 8 GB RAM, and 64-bit windows™ operating system.

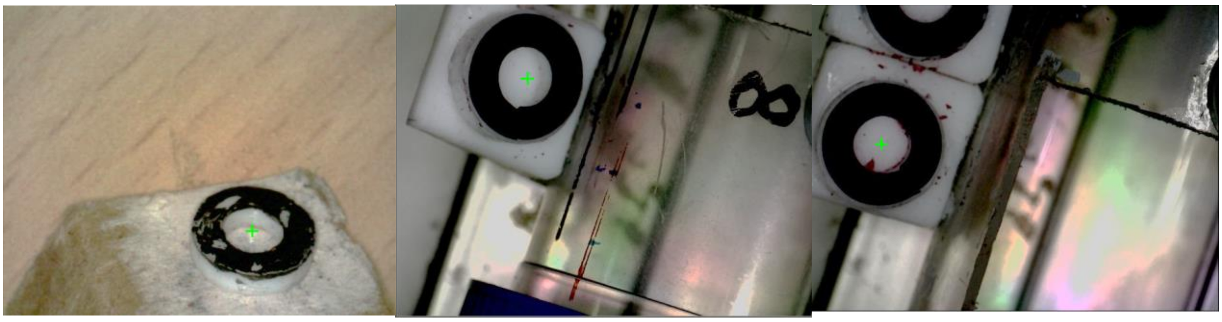

Case Study 1 Case Study 2 Case Study 3

Figure 5.14: Measurement of coordinates (green crosshair) of the center of the markers using ImageJ software

Table 5.13: Comparison of measurement of 2D coordinates of the centre of marker using our method and ImageJ software

Case studies	Our Method		ImageJ Software		2D FLE	
	X	Y	X	Y	X	Y
Case 1	389	348	390	351	-1	-3
Case 2	220	111	218	114	2	-3
Case 3	196	111	198	111	-2	0
The coordinates are measured in pixels. For this particular resolution of image, 1 mm = 23.143 pixels						

5.4 Conclusions

A robust recursive Taguchi method-based algorithm is designed for real-time detection of the markers and precise measurement of the coordinates of the reference points. The method is designed and tested for all the commonly used multimodality compatible ring-shaped markers. The method is shown to be robust, accommodates the change in marker and working ambiance comprehensively. Many cases are performed successfully with no failures. Case studies are presented for the conditions of the marker with extreme noise factors like the distorted surface, unknown lighting conditions, and marker orientation with large composite angles. Detailed results of two more marker detection and coordinate measurement are presented. The robust detection, precise measurement, and time optimization make it a feasible real-time method for autonomous anatomical body registration.

CHAPTER VI

Phantom and Vegetable Specimen based Case Studies for Modeling and Algorithms Evaluation[†]

6.1 Introduction

The earlier chapters discussed the autonomous neuro-registration, robust and real-time algorithm for autonomous neuro-registration. This chapter, as shown in figure 6.1 progresses to the implementation of autonomous neuro-registration and neuronavigation. Describe and conduct case studies to establish performance characteristics in terms of repeatability, accuracy and operative time. The performance characteristics are evaluated for many combinations of the patient pose, burr hole entry point, lesion's target point and set of registration points.

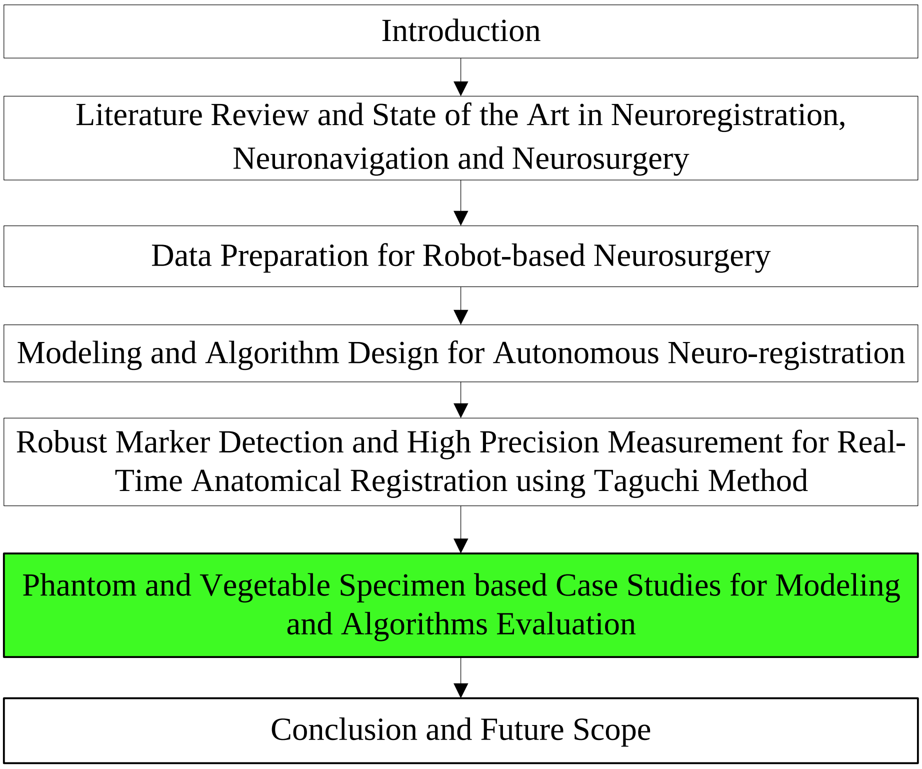

Figure 6.1: Workflow and the importance of case studies for validation of autonomous robot-based neurosurgery

[†] "Robot-based Autonomous Neuro-registration and Neuronavigation *: Implementation and Case studies"*, Kaushik A, Dwarakanath TA, Bhutani G, Dwarakanath S. World Neurosurgery, Elsevier, 2019, Volume 134, February 2020, Pages e256-e271. https://doi.org/10.1016/j.wneu.2019.10.041

6.2 Phantom-based case studies

Robot-based neurosurgery have to be highly accurate and reliable. It is subjected to rigorous tests for validation of safety, accuracy and practicability before operating on the human patient. Before going for human trials, the validation involves stage-wise progressive tests starting from simulation study[93], [94], experiments on multiple phantoms [95], experiments on fruit/vegetables to mimic the material density[100], animals [102] and cadavers [103]. This chapter presents the case studies of the robot-based autonomous neurosurgical procedure on multiple phantoms and vegetable specimen. The results of the experiments have direct bearing in qualifying the proposed robot-assisted surgical intervention on the small animals and humans.

In this chapter, the case studies of autonomous neuro-registration conducted on three case trials of the most common patient posturing and vegetable specimen are presented. The axial, coronal, sagittal sectional views and the 3D model of the skull phantom is shown in figure

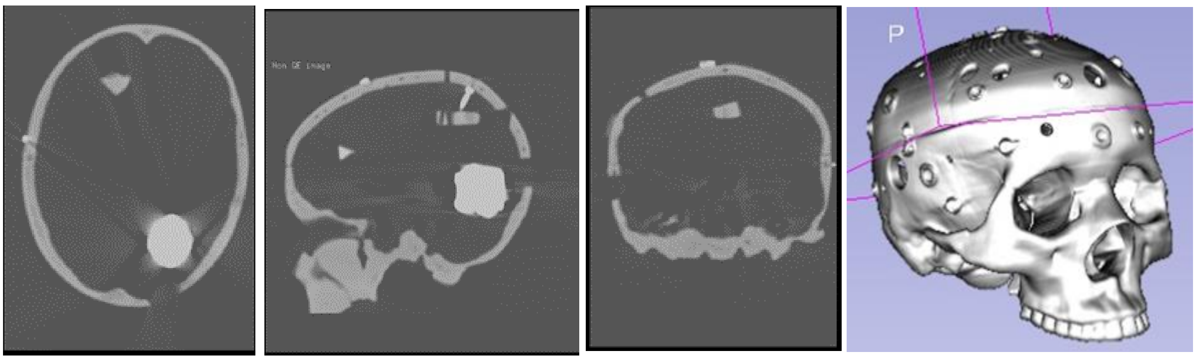

6.2.

Figure 6.2: Axial, Coronal, Sagittal views and the 3D model of the PVC skull phantom from the CT data

Case trial I is shown in figure 6.3(a), the coarse estimate of the pose of the skull phantom is the Head First Supine (HFS). HFS means that the head (of skull phantom) is in a supine position and the head is towards the robot. According to DICOM standard 3.0 [26], [27], the orientation of the image coordinate system, [I] is based on the pose of the patient on the couch. For example, the direction of X-axis of [I] is RHS to LHS, the direction of Y-axis is from anterior to posterior and direction of z axis is from foot to head of the patient. This basis is used to get a rough estimate of the phantom orientation with respect to the couch. Along with the orientation, the position of one of the markers with respect to the surgical couch is also given as a rough estimate (as discussed in the section 4.2.3 of chapter 4).

C*ase trial II* is shown in figure 6.3(b), the coarse estimate of the pose shows the skull phantom is in HFS with the image coordinate system [I] rotated by -10^0 (clockwise) about X and by $+30^0$ (anticlockwise) about Y.

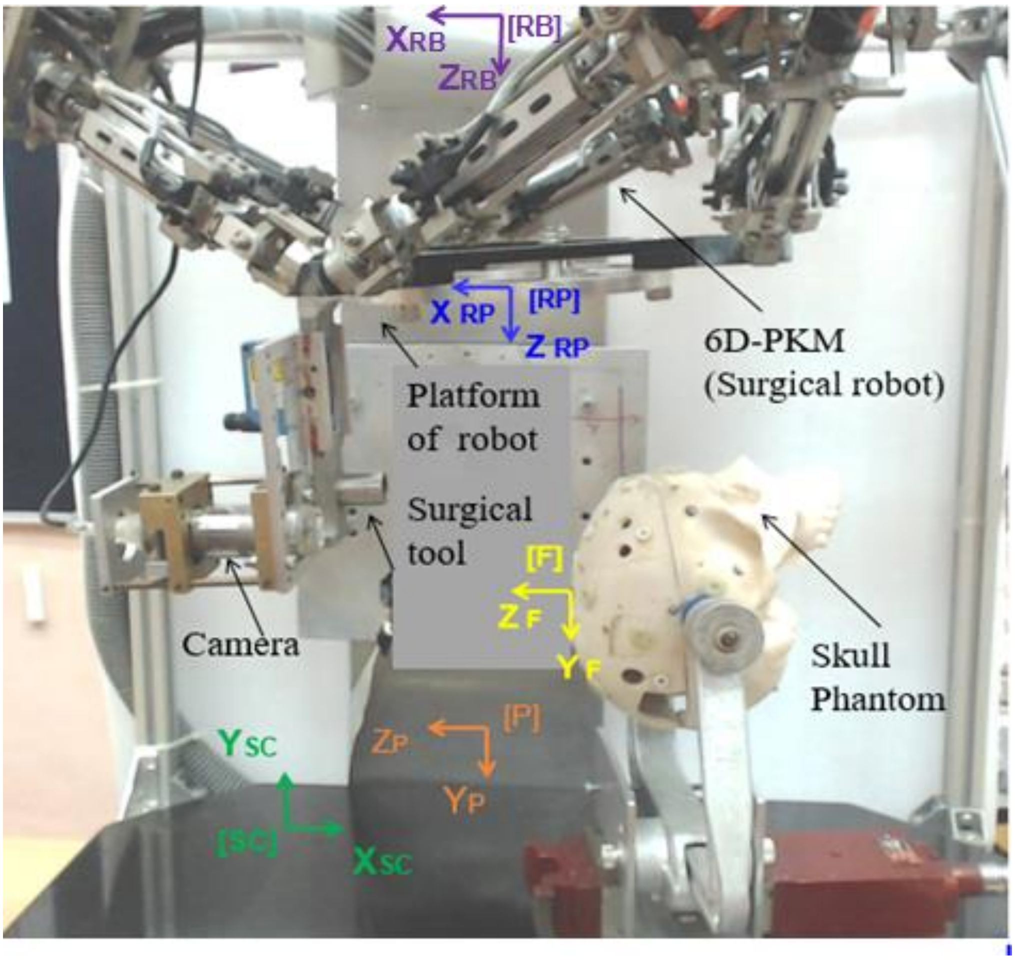

(a)

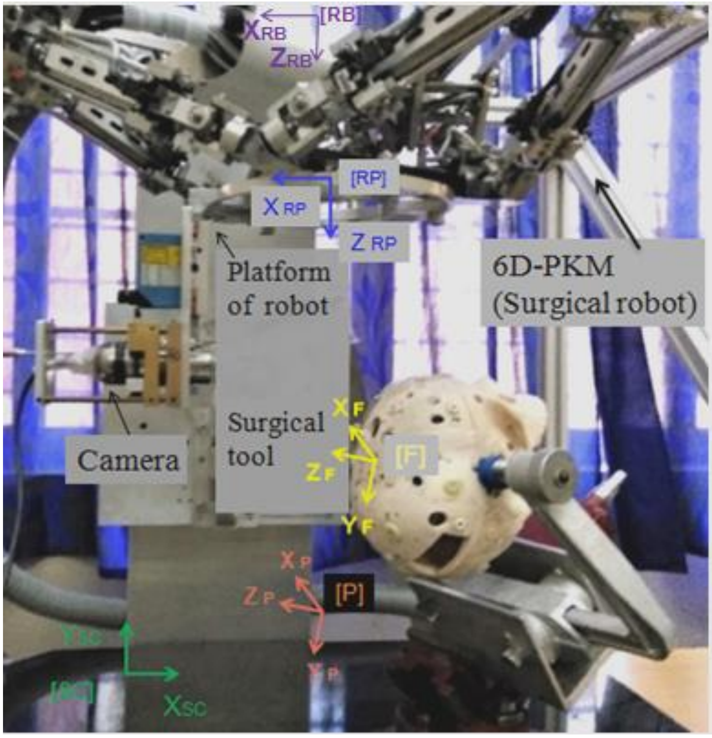

(b)

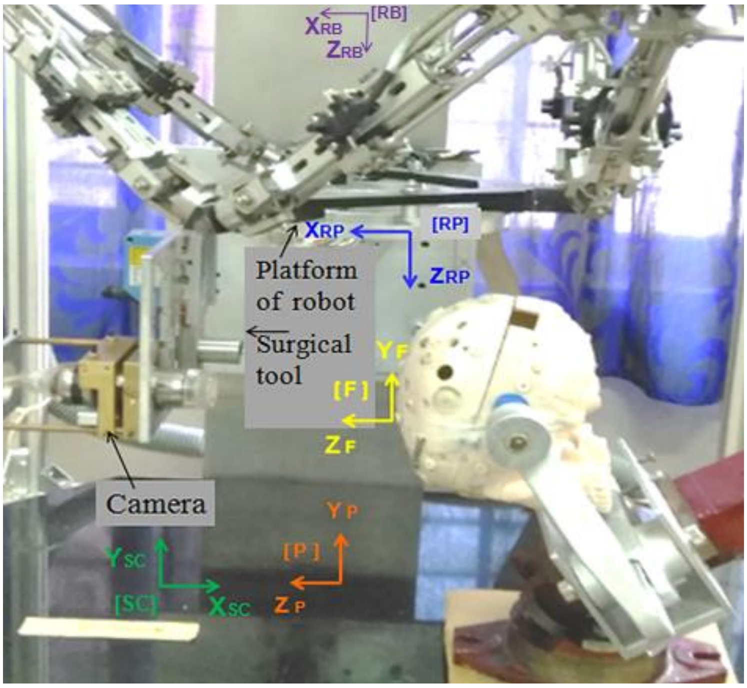

(c)

Figure 6.3: Skull phantom mounted in (a) HFS, (b) HFS with composite angles, (c) HFP pose

In the rest of the thesis, this pose (C*ase trial II*) will be referred as oriented HFS pose. *Case trial III* is shown in figure 6.3(c), the skull phantom is set in the Head First Prone (HFP) position. Head First Prone means head is toward the robot and face is toward the floor.

These experiments were repeated on an average of one experiment per day over two months. For each pose, different sets of four markers out of the available ten markers on the PVC skull phantom were used for the neuro-registration. Further to validate the method and to check the overall accuracy of the system, different target sets were used for each pose. The target sets include markers and holes of different sizes.

Table 6.1: Coordinates of registration points in a medical image, [I] for HFS pose of the phantom

Coordinates (in mm)	**Markers**			
	1	2	3	4
X	-35.46	-7.46	-21.10	-19.23
Y	9.65	10.52	27.44	-27.95
Z	75.49	85.90	79.59	74.72

Marker 1 Marker 2 Marker 3 Marker 4

Figure 6.4: Markers within the viewing window (Field of view) of the digital camera. The field of view of the camera is 19.6 mm x 15.6 mm. The pose of the skull phantom is in HFS

In *case trial I*, the pose of the skull phantom was set in HFS. The measurement of coordinates of the four markers, selected for the registration, in the medical image is shown in table 6.1. Figure 6.4 shows the successful initial localization of markers in this pose. Similarly, robot-based measurement of coordinates of the four markers on the phantom is done. The successful autonomous neuronavigation based on the proposed method for all the target points is shown in table 6.2 and figures 6.5(a) to 6.5(d).

Table 6.2 also shows the coordinates of the target points in [I] for HFS pose of the skull phantom and corresponding images of the needle touching the target points. Table 6.3 shows coordinates of the selected registration points (centre of the markers) with respect to [I], in oriented HFS pose (C*ase trial II.*).

Table 6.2: Coordinates of target points in [I] for HFS pose of the skull phantom

Coordinates (in mm)	Markers			
	1	2	3	4
X	15.75	38.32	25.43	19.85
Y	-7.23	14.34	-19.69	6.01
Z	75.61	69.63	6.01	77.43
Result (images of needle reaching the desired target points)				
Needle reaching the four target points in HFS pose of the skull phantom	Target: Marker 1 Dia. of marker: 4 mm Dia. of the needle: 2.5 mm TRE (Accuracy < 1 mm)	Target: Marker 2 Dia. of marker: 4 mm Dia. of the needle: 2.5 mm TRE (Accuracy < 1 mm)	Target: Hole 1 Dia. of hole: 5 mm Dia. of the needle: 2.5 mm TRE (Accuracy < 1 mm)	Target: Hole 2 Dia. of hole: 4 mm Dia. of the needle: 2.5 mm TRE (Accuracy < 1 mm)

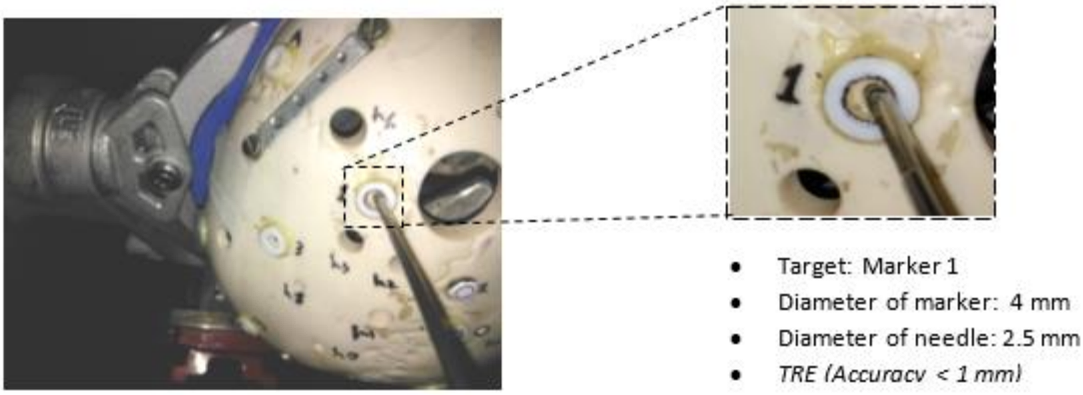
Target: Marker 1
Diameter of marker: 4 mm
Diameter of needle: 2.5 mm
TRE (Accuracy < 1 mm)

(a)

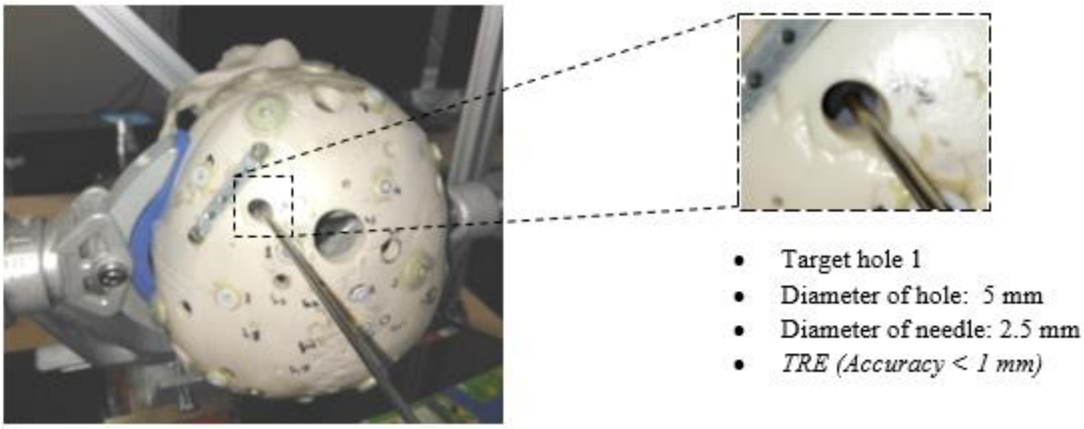
Target hole 1
Diameter of hole: 5 mm
Diameter of needle: 2.5 mm
TRE (Accuracy < 1 mm)

(b)

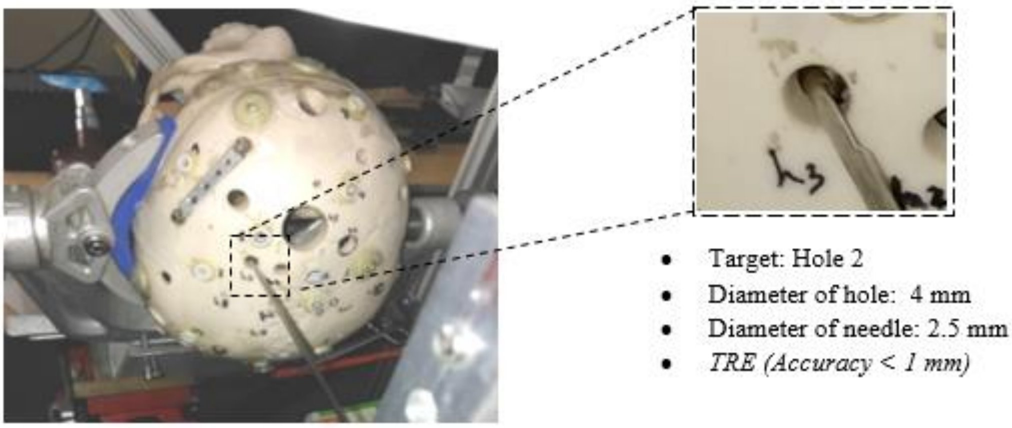
Target: Hole 2
Diameter of hole: 4 mm
Diameter of needle: 2.5 mm
TRE (Accuracy < 1 mm)

(c)

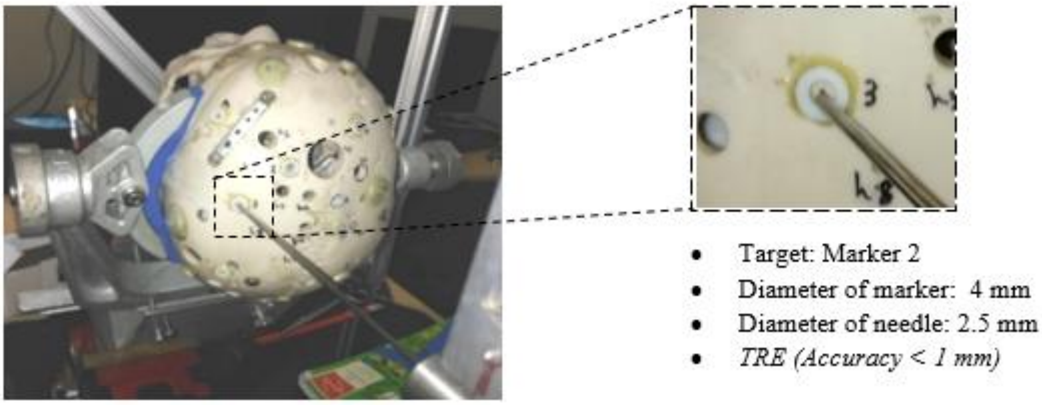

(d)

Figure 6.5: The needle has reached the four different targets for C*ase trial I.*

Figure 6.6 shows the results of the initial localization in identifying the markers for the pose of the skull phantom mentioned above. Table 6.4 gives the coordinates of the target points in [I] for this pose of the skull. Table 6.4 and figures 6.7(a) to 6.7(d) show successful neuronavigation for this pose of the skull phantom.

Table 6.3 Coordinates of registration points in a medical image, [I] for oriented HFS pose of the skull phantom

Coordinates (in mm)	**Markers**			
	1	2	3	4
X	-35.46	-7.46	-58.14	-21.10
Y	9.65	10.52	13.93	27.44
Z	75.49	85.90	61.50	79.59

Marker 1 Marker 2 Marker 3 Marker 3

Figure 6.6: Markers within the field of view of the camera. The skull phantom is in oriented HFS pose (*Case trial II*)

Table 6.4 Coordinates of target points in [I] for oriented HFS pose of the skull phantom (C*ase trial II*)

Coordinates (in mm)	**Markers**			
	1	2	3	4
X	15.75	38.32	25.43	19.85
Y	-7.23	14.34	-19.69	6.01
Z	75.61	69.63	69.15	77.43
Result (images of needle reaching the desired target points)				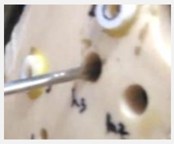
Needle reaching the four target points in oriented HFS pose of the skull	Target: Marker 1 Dia. of marker: 4 mm Dia. of the needle: 2.5 mm TRE (Accuracy < 1 mm)	Target: Marker 2 Dia. of marker: 4 mm Dia. of the needle: 2.5 mm TRE (Accuracy < 1 mm)	Target: Hole 1 Dia. of hole: 5 mm Dia. of the needle: 2.5 mm TRE (Accuracy < 1 mm)	Target: Hole 2 Dia. of hole: 4 mm Dia. of the needle: 2.5 mm TRE (Accuracy < 1 mm)

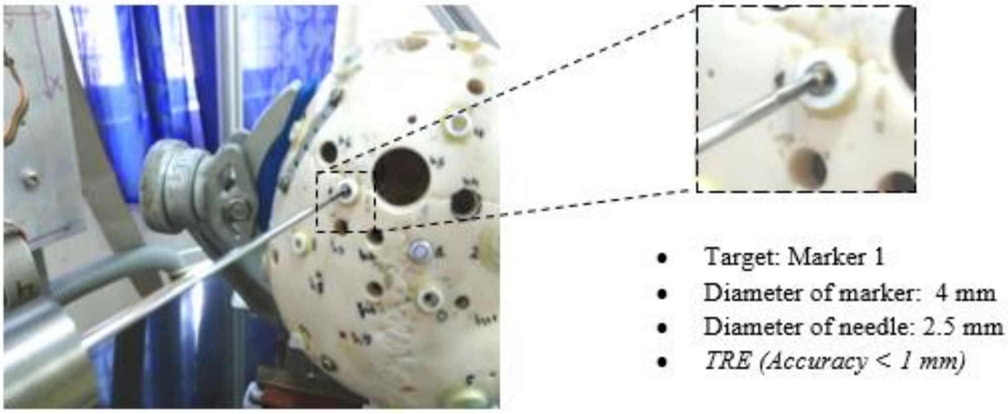

- Target: Marker 1
- Diameter of marker: 4 mm
- Diameter of needle: 2.5 mm
- *TRE (Accuracy < 1 mm)*

(a)

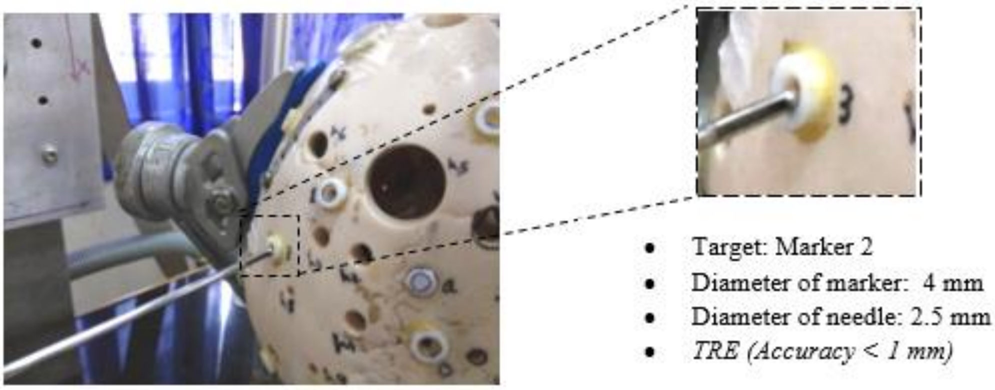

- Target: Marker 2
- Diameter of marker: 4 mm
- Diameter of needle: 2.5 mm
- *TRE (Accuracy < 1 mm)*

(b)

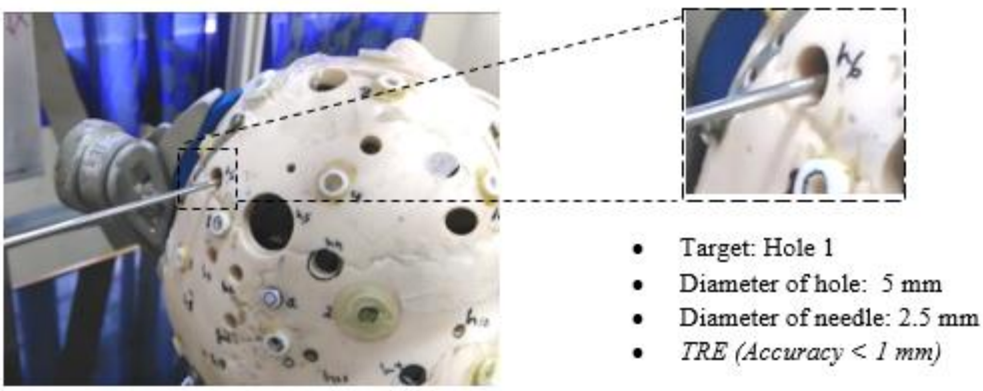

- Target: Hole 1
- Diameter of hole: 5 mm
- Diameter of needle: 2.5 mm
- *TRE (Accuracy < 1 mm)*

(c)

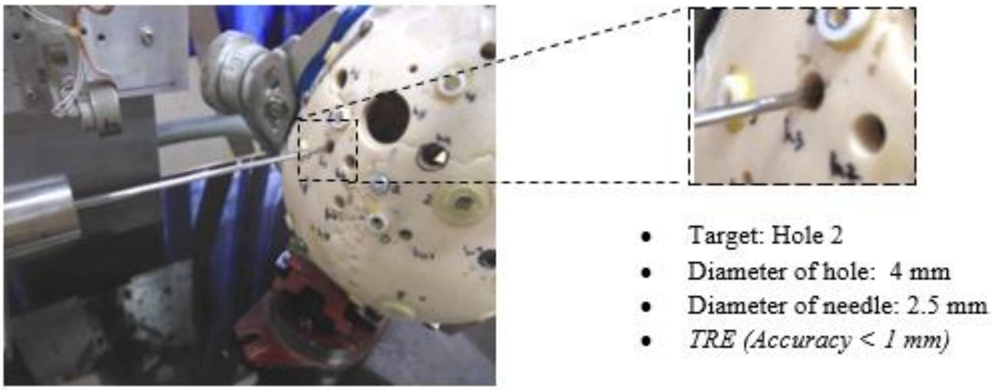

(d)

Figure 6.7: The needle has reached the four different targets for C*ase trial II.*

Similarly, coordinates of the registration points for HFP pose (C*ase trial III*) with respect to medical image [I] are given in table 6.5. The results of the initial localization in identifying the markers for this pose are shown in figure 6.8. Table 6.6 and figures 6.9(a) to 6.9(d) show the target points and successful neuronavigation based on the proposed method for HFP pose of the skull phantom (C*ase trial III*).

Table 6.5: Coordinates of target points in [I] for HFP pose of the skull phantom (C*ase trial III*)

Coordinates (in mm)	**Markers**			
	1	2	3	4
X	38.32	42.16	19.85	19.85
Y	14.34	57.62	45.64	6.01
Z	69.63	62.22	76.81	77.43

Marker 1 Marker 2 Marker 3 Marker 4

Figure 6.8 : Markers within the viewing window (Field of view) of the digital camera. The pose of the skull phantom is HFP (*Case trial III*).

Table 6.6: Coordinates of target points in [I] for HFP pose of the skull phantom (C*ase trial III*)

Coordinates (in mm)	**Markers**			
	1	2	3	4
X	-35.46	-7.73	-21.10	-11.40
Y	9.65	11.13	27.44	25.78
Z	75.49	86.15	79.59	84.34
Result (images of needle reaching the desired target points)				
Needle reaching the four target points in HFP pose of the skull phantom	Target: Marker 1 Dia. of marker: 3 mm Dia. of the needle: 2.5 mm TRE (Accuracy < 1 mm)	Target: Marker 2 Dia. of marker: 4 mm Dia. of the needle: 2.5 mm TRE (Accuracy < 1 mm)	Target: Marker 3 Dia. of hole: 4 mm Dia. of the needle: 2.5 mm TRE (Accuracy < 1 mm)	Target: Hole 1 Dia. of hole: 3 mm Dia. of the needle: 2.5 mm TRE (Accuracy < 1 mm)

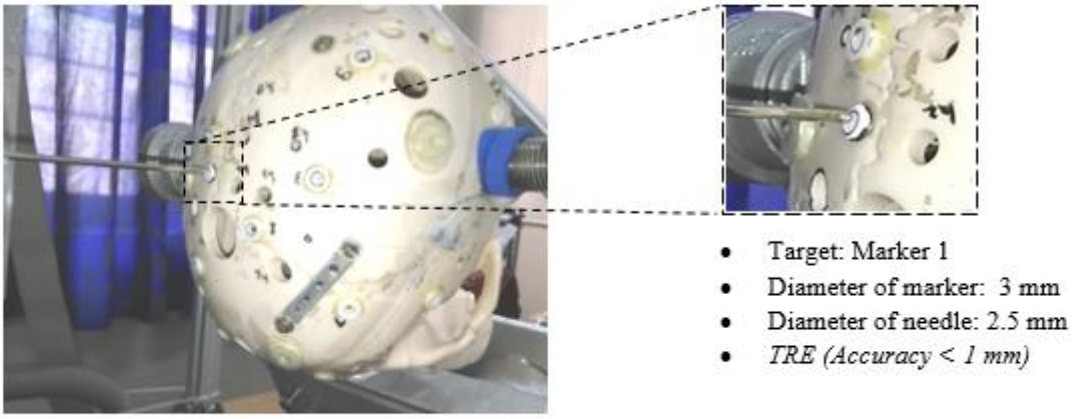

(a)

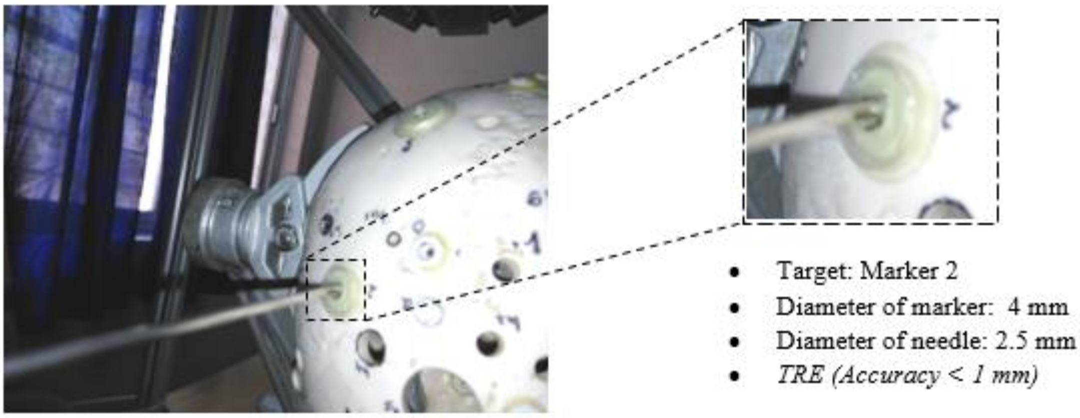

(b)

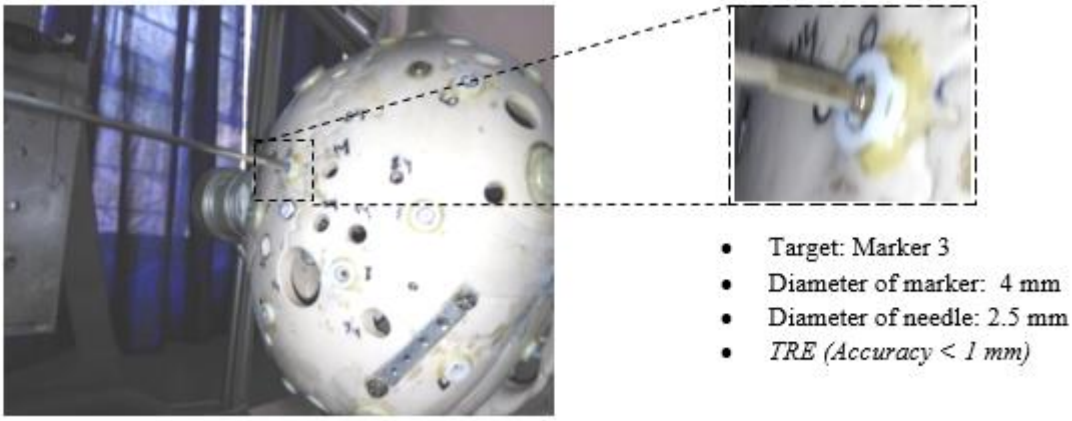

(c)

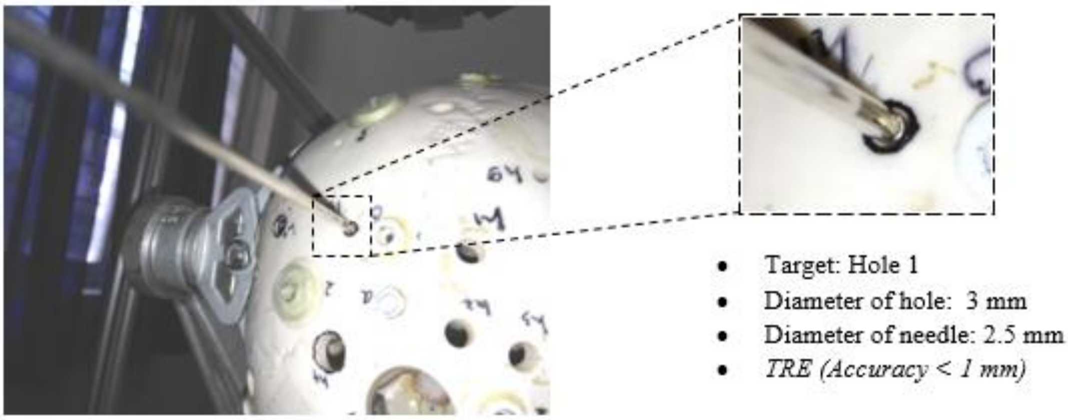

(d)

Figure 6.9: The needle has reached the four different targets for C*ase trial III*.

All three poses were successfully registered. Repetition of the registration produced consistent results. In all the cases, the overall accuracy was less than 1 mm. The results are given on the basis of go and no go. If the needle passes through a certain hole, then the maximum difference between the needle centre and hole centre is considered as error. There is no standard way to measure such a small error. The error is observed visually. For example, in table 6.6, Marker no. 4, the needle diameter is 2.5 mm and hole diameter is 3 mm. The difference is 0.5 mm. The 1 mm accuracy is a conservative statement and applies for all the experiments not just one experiment.

After autonomous registration, the biopsy needle attached to the surgical robot was able to reach all the target points successfully. All the experiments were repeated several times, and the results exhibited high repeatability in the accuracy. The maximum deviation was observed to be within 1 mm. The assessment of the results further shows that the accuracies are highest if the target lies close to the centroid of the markers used for the registration. This assessment is in line with the classic observations made by West and Fitzpatrick[129].

6.2.1 Glass jar and glass skull phantom-based experiments.

A glass jar phantom was prepared with two shells, the outer shell represents the skull and the inner shell, which is 50 mm inside the outer shell, represents the deep-rooted target. Figure 6.10 shows the glass jar phantom with many pairs of holes made on both the outer and the inner shell, which were in line with the center of the outer glass jar. These pairs of holes were separated by 50 mm in the radial distance of the inner and outer shells. Individual holes, markers and artificial targets were also attached at various places. Similarly, a glass skull phantom (see figure 6.11) is also prepared to simulate the similarity in surfaces and real approach angles. The transparent nature of phantoms aid in visualizing the accuracy of navigation.

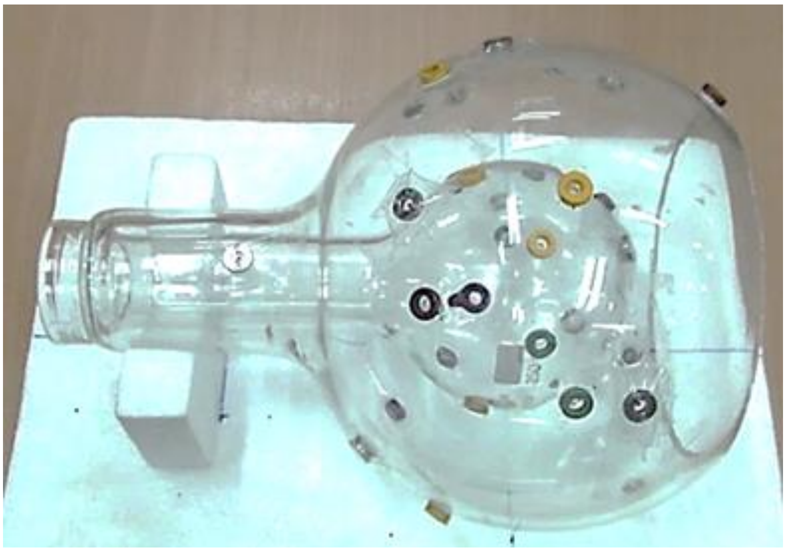

Figure 6.10: Concentric glass jar phantom with multiple pair of concentric holes

Figure 6.11 : Glass skull with fiducials

The axial, coronal, sagittal views and 3D model of the concentric glass jar and glass skull phantoms are shown in figures 6.12 and 6.13 respectively.

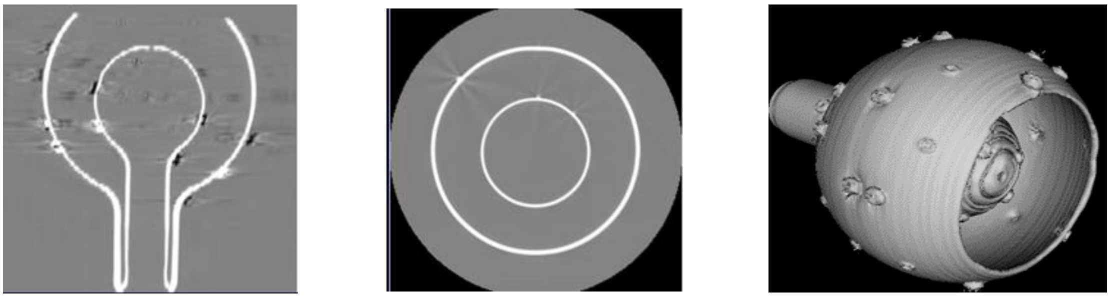

Figure 6.12: CT cross-sectional images and 3D model of concentric glass jar

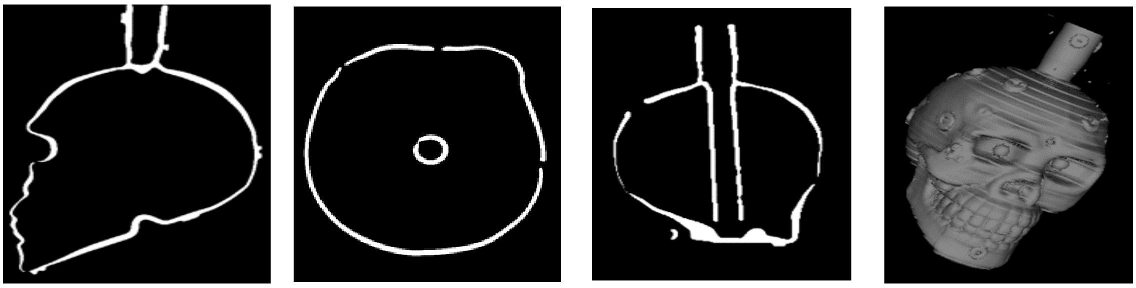

Figure 6.13: CT cross-sectional images and 3D model of glass skull phantom

To validate the path precision, a needle of the thickness of 1 mm was navigated to reach the deep-rooted target inside a double concentric jar through a path length of 195 mm. The needle was regulated to pass through a 2 mm diameter entry holes both on the outer and the inner concentric jars. Figures 6.14 and figure 6.15 show the transparent glass jar with the needle insertion. The experiment was repeated several times successfully. The similar experiment was also conducted on glass skull phantom (see figure 6.16). In both the experiments, the accuracy was found to be less than 1 mm. The Target Registration Error (TRE) and Fiducial Registration Error (FLE) were found to be less than 1 mm and 0.5 mm, respectively. The submillimeter TRE and FRE could not be measured practically. TRE and FRE were estimated by go or no-go basis by passing a needle of 2.4 mm diameter to a target hole and marker hole of 4 mm diameter, i.e., with a radial clearance of only 0.8 mm (see figure 6.16).

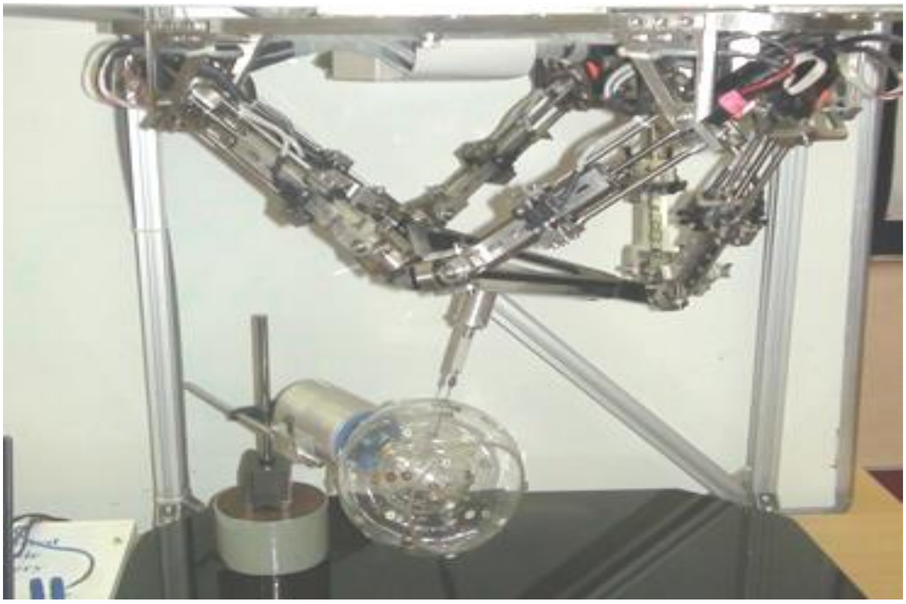

Figure 6.14: Validation of autonomous neuro-registration using glass jar phantom

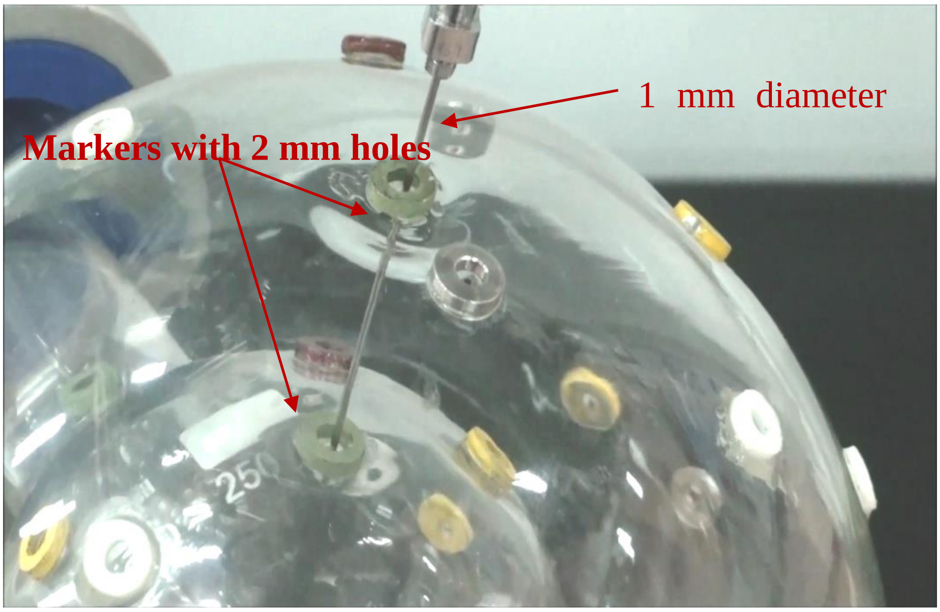

Figure 6.15: Zoomed view of the Validation of autonomous neuro-registration using glass jar phantom

In each case, the all-round clearance gap between the needle and the target hole was observed. Thus, a conservative statement of TRE < 1 mm and FRE < 0.5 mm is justified. Figure 6.16 shows that the needle is reaching one of the targets of the registered phantom.

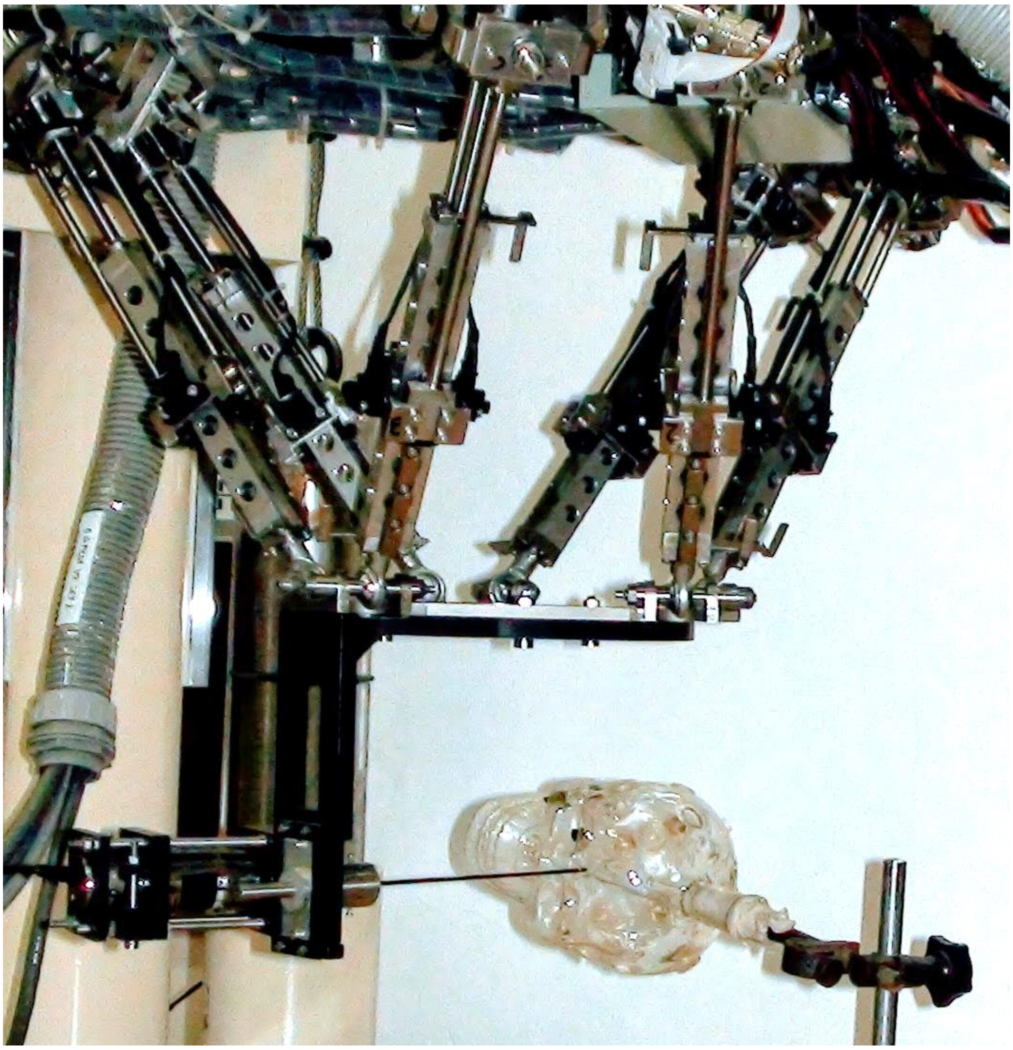

Figure 6.16: Validation of autonomous neuro-registration using glass skull phantom. The needle is passing through the target hole in registered glass skull phantom

6.3 Vegetable specimen-based case study†

This work simulates the robot-based autonomous targeted neurosurgical procedure like biopsy on a vegetable specimen. The objective of the work is to validate the robot-based autonomous neuro-registration and neuronavigation for neurosurgery in terms of stereotactic navigation and target accuracy. This case presents a preliminary study and the results of the robot-based autonomous surgical procedure on a vegetable specimen. This section discusses

† "Validation of high precision robot-assisted methods for intracranial applications: Preliminary study", Kaushik A, Dwarakanath TA, Bhutani G, Moiyadi A., Chaudhari P, World Neurosurgery, Elsevier, 2020, Volume 137, May 2020, Pages 71-77. https://doi.org/10.1016/j.wneu.2020.01.206

case study, which simulated all aspects of the actual neurosurgical procedure on vegetable specimens. The vegetable case studies are included as they closely simulate the intracranial navigation. The real tissue interaction is replicated in the tests, as the needle has to pierce and continuously pass through the material from the entry point to the target point. Stringent criteria in terms of accessing small targets and high accuracy in following the given trajectory are considered. To simulate the real tissue interaction, a small tubular tray embedded with markers was prepared for fixating the small animal for conducting the robot-assisted autonomous surgery. The tubular tray was designed for securing the animal for scanning as well as surgery. The tubular tray fixation is for small animals under anaesthesia by constraining the body mobility. However, for the rat brain surgery, the tube has to be modified to fix the head securely. The rat surgery was not a part of the thesis. As a preliminary step, before going for the rat surgery, robot-assisted surgery was conducted on a vegetable equivalent of the size of the small animal. It is conducted on a carrot as a part of robot assisted surgical rehearsal and evaluation. A carrot was subjected to surgical tests. Mint (Pudin-Hara tablet[130]) spherical capsules of size 1.5 mm spherical radius were inserted deep at three different locations. The density of a carrot is 1.04 gram/cm^3 [131], which is very similar to the average density of brain tissue (cerebrum), which is 1.043 [132], [133]; thus, the carrot was selected for the experiments. The mint capsules contain mentha (Menthe piperata), spearmint (menthe spicata) oil, and color[134], which is visible in both the CT and MRI images. Figure 6.17 shows the mint capsule concealed within the carrot. Figure 6.18 shows the tubular tray embedded with circular markers, opening for access, fixated carrot with targets (mint), and a tiny entry hole (representing the burr hole).

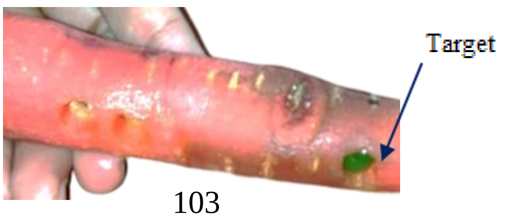

Figure 6.17: Spherical mint capsule concealed inside the carrot to serve as the target

The tubular tray is made in accordance with the requirements of the rat surgery, as shown in figure 6.19. The markers are asymmetrically distributed in spatial dimensions and encompass the targets. The target registration error (TRE) is minimized if the markers are asymmetrically distributed across the volume, and the target is close to the centroid of the set of markers[129].

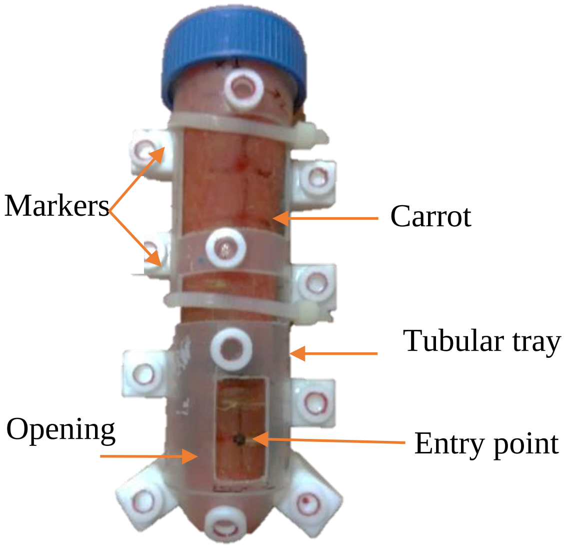

Figure 6.18: Markers embedded tray to fixate small-sized animal

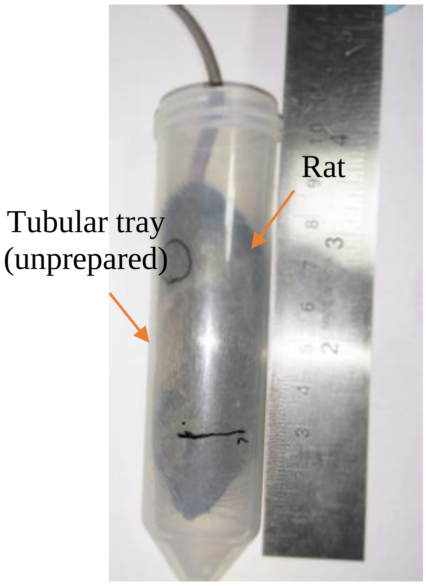

Figure 6.19: Rat inside the tubular tray (Only for measurement. No experiment was performed on the rat)

The markers are visible in CT images and are easily detected by the camera attached to the robot for registration. A high-resolution scan of the vegetable fixated in the tubular tray was taken on a micro CT machine (TriFoil Imaging Inc USA) with a bore diameter of 120 mm. The slice thickness and pixel spacing were set to be 0.15 mm. The image data was prepared for robot-assisted surgery. A software module developed at the authors' laboratory (refer section 3.3.1 of chapter 3) was used to create the axial, coronal, sagittal, and 3D views of the object. Coordinates of the four markers were measured using these views with respect to the imaging coordinate system. Details of the software module and the method of measurement of markers in medical image space (virtual space) can be found in section 3.3.1 of the chapter 3. In the real specimen space (Physical space), the markers were autonomously detected, and the coordinates of the center point of the top surface of the markers were measured by the surgical robot. The autonomous robot-assisted surgery, and the actual surgical procedure simulation case studies were conducted.

The diagrammatical depiction of the workflow is explained below. The analytical description of the methods can be found in the chapter 4.

Figure 6.20: Vegetable with tubular tray, markers, and targets

Step 1: Preparing carrot by concealing deep-rooted targets (mint) along with spherical indents of the radius of 0.75 mm shallow holes on the surface (representing the burr hole). The specimen was rigidly fixated on a tubular tray by wire tags. The rotational and lateral motions of carrot with respect to the tray were locked by wire tags, and the longitudinal motion was locked by tightening the cap of the tube. The tray was embedded with circular markers (see figure 6.20). The same tray would be used for the surgery of the rat and other small animals.

Step 2: A scan of the prepared specimen was taken in the micro CT machine. Figure 6.21 shows the micro CT machine and zoomed view of tubular tray attached at the bed of the machine

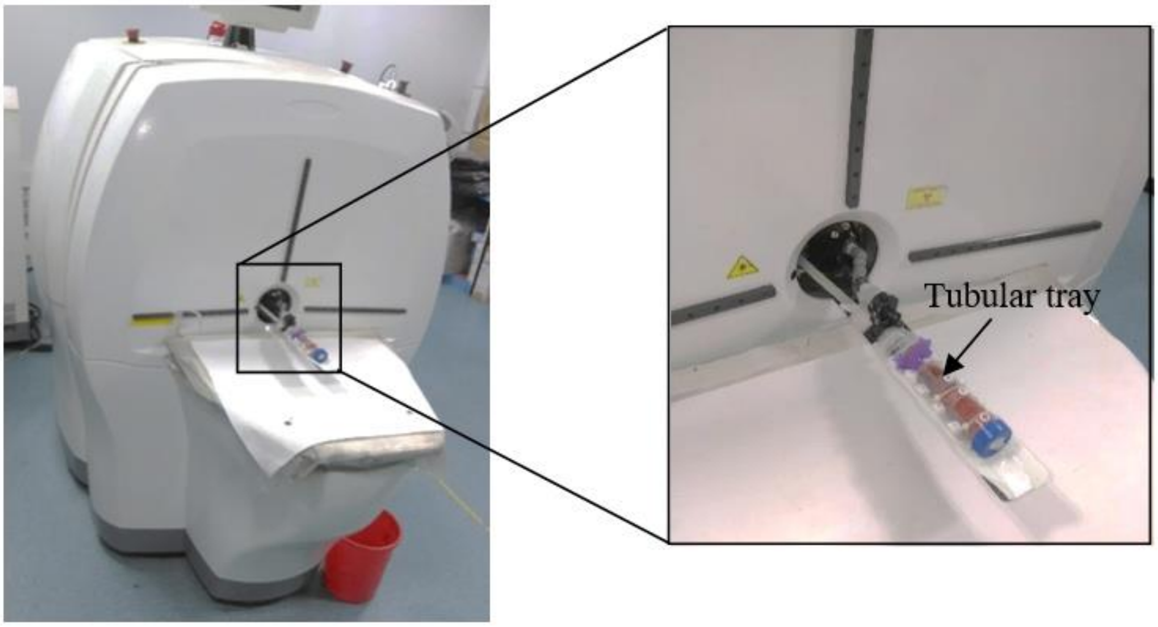

Figure 6.21: Micro CT scan of the specimen and zoomed view of the specimen

Step 3: Generation of axial, coronal, sagittal views, construction of a 3D model from the CT image slices (see figure 6.22), and measurement of the coordinates of the center of markers with respect to the imaging coordinate system (Virtual space).

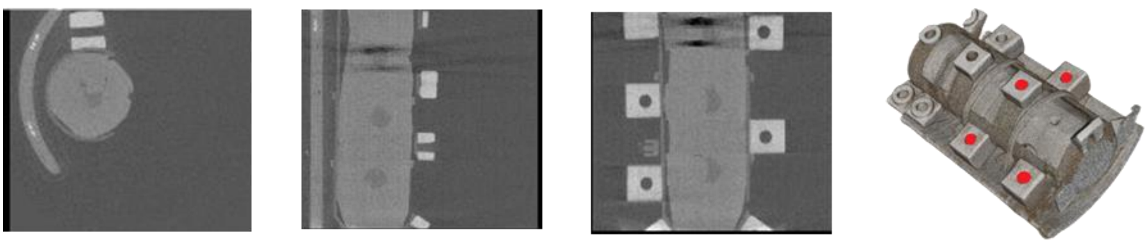

Figure 6.22: Axial, coronal, sagittal, and 3D view of the scanned specimen. Red dots indicate that fiducial markers were measured in the imaging space [I] during the registration process

Step 4: In the lab OT, the surgical robot conducted an autonomous high precision coordinate measurement of the same number of markers in the same order of measurement as in step 3 for the registration, as shown in figure 6.23.

Step 5: The surgical robot reached the target following the specified trajectory through the entry point, as specified in the imaging space.

Figure 6.23: Autonomous robotic measurement of the same markers in real patient space for registration

Four fiducial markers (shown red in figure 6.22) were measured with respect to both the image space and the real patient space (vegetable specimen space, in this case) for registration. During measurement in the image space, the entry point and the target point were also marked and measured. The target points were the volume center of the mint tablets, which were a sphere of 1.5 mm radius. The entry points were the center of the spherical indents on the surface of the vegetable. These points were later transformed with respect to the robot. The robot motion algorithm regulates the robot trajectory to ensure that the surgical needle passes through the entry point and reaches the target point. The target was reached by honouring both the entry and target points. The trajectory of the needle inside the specimen was controlled within 1 mm precision. The final configuration of the robot accessing the target point is shown in figure 6.24. The successful puncture of the mint tablet placed as a target and spilled mint confirmed accessing the target with high precision. The experiment was repeated multiple times to observe the high repeatability of the results. Further, the experiments were conducted with different target and entry locations.

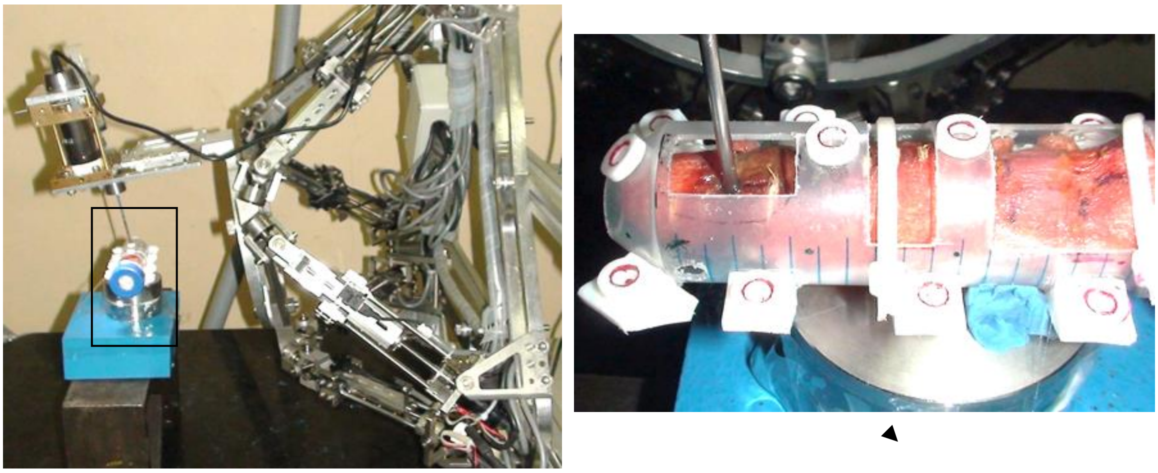

(a) (b)

Figure 6.24: Robot access of the target point after autonomous neuro-registration

All algorithms were executed on Intel inside™ core i7 processor, 8 GB RAM, and 64-bit windows™ operating system-based computer. The execution time depends on the surgical task. The average execution time of the autonomous neuro-registration algorithm is found to be less than 5 minutes.

6.4 Conclusions

The proposed robot-assisted autonomous neuro-registration shows an all-round improvement. The robot-assisted registration is shown to result in high accuracy and repeatability and provides time-optimal registration. Also, multiple registrations during a course of surgery have become necessary due to newer intra-operative imaging practices; autonomous neuro-registration serves as the right solution due to its performance attributes. The benefits in saving the OT time for the patient and OT occupancy are significant. The vulnerability to mistakes in mapping is avoided in the autonomous registration leading to a fault-free correspondence. The human factors affecting the accuracy and consistency have been minimised substantially. The results of the experiments show the successful replication of the robot assisted surgical procedures. The same performance values over a large number of experiments reveal high consistency. The case studies are of higher intricacies in terms of trajectory precision and accuracy. The method can serve many domains of the robot assisted spine and neurosurgery. The robot, the method and the algorithms in the case studies have met the prescribed guidelines for the robot based autonomous neurosurgery for the next stage of experiments on small animals and humans.

CHAPTER VII

Conclusion and Future Work

7.1 Conclusion:

Capabilities of MIS can be largely enhanced by coupling it with the robotics, advance visualization and navigation technologies.

The DICOM tags though contain large information for surgery, the newer DICOM tags prepared in the work facilitate robot assisted autonomous registration and navigation.

The imaging-based visualization can be considered as one of the major prerequisites for frameless stereotactic robot-based neurosurgery. The enhanced visualization with detailed internal information of the patient has high impact on presurgical planning, surgical guidance and supervision.

The accuracy and persistent focus are most important feature in neurosurgery. Robot assisted measurement eliminate the chances of human mistakes. Reducing the human interventions will considerably enhance the accuracy. The precision and repetitive operations i.e. selection of a reference points in medical and real patient space, coordinate measurement, navigation of the needle within the brain to a specific point, repetitive tasks, tremor-free motion of the surgical needle, and correspondence of points in both the spaces are well suited for robot-based neurosurgery.

The parallel robots best-fits the neurosurgical application due to the reason that small region to be attended with high accuracy and rigidity. The robot based autonomous, frameless neuro-registration can provide accuracy comparable to frame-based-method. Also provides enhanced solution as the line of sight problem, manual correspondence, and need of additional equipment for measurement is eliminated.

The accuracy of registration has direct bearing on the measurement of markers. Most of the image processing operation related to the robot-based neurosurgery are sensitive to the working ambiance. It is impractical to set stringent pre-conditions on working ambience of the OT. The algorithms developed for autonomous neuro-registration accommodate varied working conditions of OT, i.e. change in lighting, markers, patient etc.

The real-time implementation of the algorithms is one of the most important concerns for the autonomous-neuro-registration. The framework introduced based on the Taguchi method is shown to be suitable for optimizing parameters of the image processing algorithms, design a robust marker detection and coordinate measurement. Identifying control factors of working ambience and optimising them using Taguchi method helped to achieve robust real time measurement.

The design of various phantoms apart from standard skull type, like spherical concentric glass jars, transparent glass skull with markers served the purpose of evaluating performance characteristics in term of accuracy, precision, trajectory of navigation and time.

The vegetable-based experiments are the advance validation of robot-based neurosurgery to check the performance characteristics and needle tissue interaction. The vegetable experiments-based validation prior to the animal and the human trial runs give greater insight into the performance characteristics of robot assisted neurosurgery. Rehearsing and training before the surgery is feasible and economical.

The autonomous neuro-registration is faster, accurate and eliminate human errors. High precision trajectory following navigation through a small burr hole supports MIS. The overall accuracy achieved is less than 1 mm. All algorithms were executed on Intel inside™ core i7 processor, 8 GB RAM, and 64-bit windows™ operating system-based computer. The execution time depends on the surgical task. The average execution time of the autonomous neuro-registration algorithm and marker detection and coordinate measurement algorithm are found to be less than 5 minutes and 1.37 seconds per marker respectively.

The autonomous neuro-registration and navigation is a progressive technology toward the patient friendly and accurate neurosurgical method.

7.2 Future Scope:

The autonomous neuro-registration method is developed, implemented, and validated for the multiple phantoms and vegetable specimens. The method can also be validated for small animal and cadaver surgeries. The same setup of the tubular tray, which is used for the vegetable specimen surgery, can be used for the biopsy of rat and mouse. The algorithms developed for robot-based neurosurgery build a foundation for the other surgeries thus can be modified for robot-based autonomous spine surgery. The data can be prepared using multimodality fused medical images to provide enhanced information to conduct the robot-based neurosurgery. Present OT design is based on human surgeons conducting the surgeries, can be modified to facilitate robot based autonomous surgery.

References

[1] J. Engel, T. A. Pedley, and J. Aicardi, *Epilepsy: A Comprehensive Textbook*, no. v. 3. Wolters Kluwer Health/Lippincott Williams & Wilkins, 2008.

[2] O. P. Jaggi, *Cancer: Causes, Prevention And Treatment*. Orient Paperbacks, 2005.

[3] National Institute of Health, “https://www.nia.nih.gov/health/parkinsons-disease.” https://www.nia.nih.gov/health/parkinsons-disease (accessed Feb. 01, 2020).

[4] W. S. Anderson and T. S. I. N. Neurosurgery, *Deep Brain Stimulation: Techniques and Practices*. Thieme, 2019.

[5] A. Raabe, *The Craniotomy Atlas*. Thieme, 2019.

[6] D. C. Brooks, *Current Review of Minimally Invasive Surgery*. Springer New York, 2012.

[7] V. Horsley and R. H. Clarke, “The structure and functions of the cerebellum examined by a new method,” *Brain*, vol. 31, no. 1, pp. 45–124, 1908, doi: 10.1093/brain/31.1.45.

[8] L. Leksell, “Occasional review Stereotactic radiosurgery,” *J. Neurol. Neurosurg. Psychiatry*, vol. 46, no. April, pp. 797–803, 1983, doi: 10.1136/jnnp.46.9.797.

[9] P. Suetens, *Fundamentalsof Medical Imaging*. Cambridge University Press, 210AD.

[10] “Springer - MRI Physics for Physicians.pdf.” .

[11] Y. S. Kwoh, J. Hou, E. A. Jonckheere, and S. Hayati, “A robot with improved absolute positioning accuracy for CT guided stereotactic brain surgery,” *IEEE Trans. Biomed. Eng.*, vol. 35, no. 2, pp. 153–160, 1988, doi: 10.1109/10.1354.

[12] J. Pransky, “ROBODOC - surgical robot success story,” *Ind. Rob.*, vol. 24, no. 3, pp.

231–233, 1997, doi: 10.1108/01439919710167444.

[13] Intutive surgical, “Da vinci.” https://www.intuitive.com/en-us/products-and-services/da-vinci/systems (accessed Feb. 15, 2020).

[14] J. Rosen, B. Hannaford, and R. M. Satava, *Surgical Robotics: Systems Applications and Visions*. Springer US, 2011.

[15] P. A. Woerdeman, P. W. A. Willems, H. J. Noordmans, C. A. F. Tulleken, and J. W. B. Van Der Sprenkel, “Application accuracy in frameless image-guided neurosurgery: A comparison study of three patient-to-image registration methods,” *J. Neurosurg.*, vol. 106, no. 6, pp. 1012–1016, 2007, doi: 10.3171/jns.2007.106.6.1012.

[16] S. Wolfsberger, K. Rössler, R. Regatschnig, and K. Ungersböck, “Anatomical landmarks for image registration in frameless stereotactic neuronavigation,” *Neurosurg. Rev.*, vol. 25, no. 1–2, pp. 68–72, 2002, doi: 10.1007/s10143-001-0201-x.

[17] C. R. Wilson, “The Essential Physics of Medical Imaging, 2nd Edition,” *Shock*, vol. 19, no. 4. p. 398, 2003, doi: 10.1097/00024382-200304000-00022.

[18] D. Weishaupt, V. D. Kochli, B. Marincek, and E. E. Kim, *How Does MRI Work? An Introduction to the Physics and Function of Magnetic Resonance Imaging*, vol. 48, no. 11. 2007.

[19] J. L. Cura, P. Seguí, and C. Nicolau, *Learning Ultrasound Imaging*. Springer Berlin Heidelberg, 2012.

[20] D. W. T. Dale L Bailey, *Positron Emission Tomography*. .

[21] Roger Bourne, *Fundamentals of Digital Imaging in Medicine*. .

[22] S. O. Mahboob and M. Eljamel, “Intraoperative image-guided surgery in neuro-

oncology with specific focus on high-grade gliomas," *Futur. Oncol.*, vol. 13, no. 26, pp. 2349–2361, Nov. 2017, doi: 10.2217/fon-2017-0195.

[23] R. M. Comeau, A. F. Sadikot, A. Fenster, and T. M. Peters, "Intraoperative ultrasound for guidance and tissue shift correction in image-guided neurosurgery," *Med. Phys.*, vol. 27, no. 4, pp. 787–800, Apr. 2000, doi: 10.1118/1.598942.

[24] H. Rivaz and D. L. Collins, "Deformable registration of preoperative MR, pre-resection ultrasound, and post-resection ultrasound images of neurosurgery," *Int. J. Comput. Assist. Radiol. Surg.*, vol. 10, no. 7, pp. 1017–1028, 2015, doi: 10.1007/s11548-014-1099-4.

[25] F. Prada *et al.*, "Fusion imaging for intra-operative ultrasound-based navigation in neurosurgery," *J. Ultrasound*, vol. 17, no. 3, pp. 243–251, 2014, doi: 10.1007/s40477-014-0111-8.

[26] O. S. Pianykh, *Digital imaging and communications in medicine (DICOM)*. 2011.

[27] *PS 3.3-2011 Digital Imaging and Communications in Medicine (DICOM) Part 3: Information Object Definitions*. NEMA, 2011.

[28] R. Kikinis, S. D. Pieper, and K. G. Vosburgh, "3D Slicer: A Platform for Subject-Specific Image Analysis, Visualization, and Clinical Support BT - Intraoperative Imaging and Image-Guided Therapy," F. A. Jolesz, Ed. New York, NY: Springer New York, 2014, pp. 277–289.

[29] A. Fedorov *et al.*, "3D Slicer as an image computing platform for the Quantitative Imaging Network," *Magn. Reson. Imaging*, vol. 30, no. 9, pp. 1323–1341, Nov. 2012, doi: 10.1016/j.mri.2012.05.001.

[30] Slicer community, "3D slicer." https://www.slicer.org/ (accessed Feb. 11, 2020).

[31] VTK, “Visualization Toolkit.” www.vtk.org (accessed Feb. 11, 2020).

[32] ITK, “Insight Toolkit.” www.itk.org (accessed Feb. 11, 2020).

[33] OsiriX, “Osirix-Viewer.” https://www.osirix-viewer.com/ (accessed Feb. 11, 2020).

[34] R. Viewer, “RadiAnt Viewer.” https://www.radiantviewer.com/ (accessed Feb. 11, 2020).

[35] L. T. De Paolis, M. Pulimeno, L. Ramundo, and G. Aloisio, “Human anatomy visualization and navigation system for image-guided surgery,” *Final Progr. Abstr. B. - 9th Int. Conf. Inf. Technol. Appl. Biomed. ITAB 2009*, no. November, pp. 5–7, 2009, doi: 10.1109/ITAB.2009.5394338.

[36] B. Zeng, F. Meng, H. Ding, and G. Wang, “A surgical robot with augmented reality visualization for stereoelectroencephalography electrode implantation,” *Int. J. Comput. Assist. Radiol. Surg.*, vol. 12, no. 8, pp. 1355–1368, 2017, doi: 10.1007/s11548-017-1634-1.

[37] OpenCV: Open source computer vision library, “OpenCV Tutorials.” https://docs.opencv.org/master/d9/df8/tutorial_root.html (accessed Jul. 13, 2019).

[38] OpenCV, “OpenCV.” https://opencv.org/ (accessed Sep. 04, 2019).

[39] K. Dawson-howe, *(Wiley-IS&T Series in Imaging Science and Technology) Kenneth Dawson-Howe - A Practical Introduction to Computer Vision with OpenCV-Wiley (2014)*. .

[40] S. van der Walt *et al.*, “scikit-image: image processing in Python,” *PeerJ*, vol. 2, p. e453, 2014, doi: 10.7717/peerj.453.

[41] G. Taguchi and S. Konishi, *Taguchi methods: orthogonal arrays and linear graphs;*

tools for quality engineering. ASI press, 1987.

[42] Madhav S. Phadke, *Quality Engineering Using Robust Design*, ISBN-13: 9. Prentice Hall, 1989.

[43] C. F. Lin, P. H. Yang, C. C. Wu, and T. Y. Kuo, "Application of Taguchi Method in Light-Emitting Diode Backlight Design for Wide Color Gamut Displays," *IEEE/OSA J. Disp. Technol.*, vol. 5, no. 8, pp. 323–330, 2009, doi: 10.1109/JDT.2009.2023606.

[44] C. H. Yeh, Z. Q. Zhao, P. L. Shen, and Y. C. Lin, "Optimization of an optical inspection system based on the taguchi method for quantitative analysis of point-of-care testing," *Sensors (Switzerland)*, vol. 14, no. 9, pp. 16148–16158, 2014, doi: 10.3390/s140916148.

[45] J. L. Rosa, A. Robin, M. B. Silva, C. A. Baldan, and M. P. Peres, "Electrodeposition of copper on titanium wires: Taguchi experimental design approach," *J. Mater. Process. Technol.*, vol. 209, no. 3, pp. 1181–1188, 2009, doi: 10.1016/j.jmatprotec.2008.03.021.

[46] Y. T. Liu, R. F. Fung, and C. C. Wang, "Application of the nonlinear, double-dynamic taguchi method to the precision positioning device using combined piezo-VCM actuator," *IEEE Trans. Ultrason. Ferroelectr. Freq. Control*, vol. 54, no. 2, pp. 240–250, 2007, doi: 10.1109/TUFFC.2007.239.

[47] T. Roy and R. K. Dutta, "Integrated fuzzy AHP and fuzzy TOPSIS methods for multi-objective optimization of electro discharge machining process," *Soft Comput.*, pp. 1–11, 2018, doi: 10.1007/s00500-018-3173-2.

[48] R. S. Rao, C. G. Kumar, R. S. Prakasham, and P. J. Hobbs, "The Taguchi methodology as a statistical tool for biotechnological applications: A critical appraisal," *Biotechnol. J.*, vol. 3, no. 4, pp. 510–523, 2008, doi: 10.1002/biot.200700201.

[49] R. S. Prakasham, C. S. Rao, R. S. Rao, S. Rajesham, and P. N. Sarma, "Optimization of alkaline protease production by Bacillus sp. using taguchi methodology," *Appl. Biochem. Biotechnol.*, vol. 120, no. 2, pp. 133–144, 2005, doi: 10.1385/ABAB:120:2:133.

[50] A. Chenthamarakshan *et al.*, "Optimization of laccase production from Marasmiellus palmivorus LA1 by Taguchi method of Design of experiments," *BMC Biotechnol.*, vol. 17, no. 1, pp. 1–10, 2017, doi: 10.1186/s12896-017-0333-x.

[51] C. W. Hong, "Using the Taguchi method for effective market segmentation," *Expert Syst. Appl.*, vol. 39, no. 5, pp. 5451–5459, 2012, doi: 10.1016/j.eswa.2011.11.040.

[52] G. C. Sharp, S. Kollipara, T. Madden, S. B. Jiang, and S. J. Rosenthal, "Anatomic feature-based registration for patient set-up in head and neck cancer radiotherapy," *Phys. Med. Biol.*, vol. 50, no. 19, p. 4667, 2005.

[53] A. H. EL SANOUSI, F. A. A. MUSTAFA, and M. I. B. YAHIA, "Accuracy Analysis For Anatomical Landmarks Based Registration in Image Guided Neurosurgery." Sudan University of Sciences and Technology, 2015.

[54] S. Hunsche *et al.*, "MR-guided stereotactic neurosurgery—comparison of fiducial-based and anatomical landmark transformation approaches," *Phys. Med. Biol.*, vol. 49, no. 12, p. 2705, 2004.

[55] P. W. A. Willems, J. W. B. van der Sprenkel, and C. A. F. Tulleken, "Comparison of adhesive markers, anatomical landmarks, and surface matching in patient-to-image registration for frameless stereotaxy," in *Biomonitoring and Endoscopy Technologies*, 2001, vol. 4158, pp. 156–163.

[56] D. Han, Y. Gao, G. Wu, P.-T. Yap, and D. Shen, "Robust anatomical landmark

detection with application to MR brain image registration," *Comput. Med. Imaging Graph.*, vol. 46, pp. 277–290, 2015.

[57] Y. Sun *et al.*, "Validation of anatomical landmarks-based registration for image-guided surgery: an in-vitro study," *J. Cranio-Maxillofacial Surg.*, vol. 41, no. 6, pp. 522–526, 2013.

[58] S.-H. Kang, M.-K. Kim, J.-H. Kim, H.-K. Park, S.-H. Lee, and W. Park, "The validity of marker registration for an optimal integration method in mandibular navigation surgery," *J. Oral Maxillofac. Surg.*, vol. 71, no. 2, pp. 366–375, 2013.

[59] H. K. Gumprecht, D. C. Widenka, and C. B. Lumenta, "First Experience with the BrainLab VectorVision Neuronavigation System," in *Minimally Invasive Techniques for Neurosurgery*, Springer, 1998, pp. 207–213.

[60] H. K. Gumprecht, D. C. Widenka, and C. B. Lumenta, "Brain Lab VectorVision neuronavigation system: technology and clinical experiences in 131 cases," *Neurosurgery*, vol. 44, no. 1, pp. 97–104, 1999.

[61] R. Buchalla, S. Hopf-Jensen, O. Rubarth, and W. Börm, "Frameless navigated biopsy with the BrainLAB® VarioGuide system: a technical note," *J. Neurol. Surg. Part A Cent. Eur. Neurosurg.*, vol. 74, no. 05, pp. 321–324, 2013.

[62] B. K. P. Horn, H. M. Hilden, and S. Negahdaripour, "Closed-form solution of absolute orientation using orthonormal matrices," *J. Opt. Soc. Am. A*, vol. 5, no. 7, p. 1127, 1988, doi: 10.1364/josaa.5.001127.

[63] B. K. P. Horn, "Closed-form solution of absolute orientation using unit quaternions," *J. Opt. Soc. Am. A*, vol. 4, no. 4, p. 629, 1987, doi: 10.1364/josaa.4.000629.

[64] J. A. Marvel and K. Van Wyk, "Simplified framework for robot coordinate registration

for manufacturing applications," *2016 IEEE Int. Symp. Assem. Manuf. ISAM 2016*, pp. 56–63, 2016, doi: 10.1109/ISAM.2016.7750718.

[65] W. B. Heard, *Rigid Body Mechanics: Mathematics, Physics and Applications*. 2008.

[66] J. B. West and J. M. Fitzpatrick, "The distribution of target registration error in rigid-body, point-based registration," *Lect. Notes Comput. Sci. (including Subser. Lect. Notes Artif. Intell. Lect. Notes Bioinformatics)*, vol. 1613, no. 9, pp. 460–465, 1999, doi: 10.1007/3-540-48714-x_46.

[67] J. B. West, J. M. Fitzpatrick, S. A. Toms, C. R. Maurer, and R. J. Maciunas, "Fiducial point placement and the accuracy of point-based, rigid body registration," *Neurosurgery*, vol. 48, no. 4, pp. 810–817, 2001, doi: 10.1227/00006123-200104000-00023.

[68] S. Umeyama, "Least-Squares Estimation of Transformation Parameters Between Two Point Patterns," *IEEE Transactions on Pattern Analysis and Machine Intelligence*, vol. 13, no. 4. pp. 376–380, 1991, doi: 10.1109/34.88573.

[69] F. Šuligoj, "SPATIAL PATIENT REGISTRATION IN ROBOTIC NEUROSURGERY Thesis," no. October, 2018, doi: 10.13140/RG.2.2.15823.74402.

[70] D. W. Eggert, A. Lorusso, and R. B. Fisher, "Estimating 3-D rigid body transformations: A comparison of four major algorithms," *Mach. Vis. Appl.*, vol. 9, no. 5–6, pp. 272–290, 1997, doi: 10.1007/s001380050048.

[71] K. S. Arun, T. S. Huang, and S. D. Blostein, "Least-Squares Fitting of Two 3-D Point Sets," *IEEE Trans. Pattern Anal. Mach. Intell.*, vol. PAMI-9, no. 5, pp. 698–700, 1987, doi: 10.1109/TPAMI.1987.4767965.

[72] J. M. Fitzpatrick, "The role of registration in accurate surgical guidance," *Proc. Inst.*

Mech. Eng. Part H J. Eng. Med., vol. 224, no. 5, pp. 607–622, 2010, doi: 10.1243/09544119JEIM589.

[73] J. M. Fitzpatrick, “Fiducial registration error and target registration error are uncorrelated,” *Med. Imaging 2009 Vis. Image-Guided Proced. Model.*, vol. 7261, p. 726102, 2009, doi: 10.1117/12.813601.

[74] F. Meng, F. Zhai, B. Zeng, H. Ding, and G. Wang, “An automatic markerless registration method for neurosurgical robotics based on an optical camera,” *Int. J. Comput. Assist. Radiol. Surg.*, vol. 13, no. 2, pp. 253–265, 2018, doi: 10.1007/s11548-017-1675-5.

[75] C. T. Hsieh, “An efficient development of 3D surface registration by Point Cloud Library (PCL),” *ISPACS 2012 - IEEE Int. Symp. Intell. Signal Process. Commun. Syst.*, no. November 2012, pp. 729–734, 2012, doi: 10.1109/ISPACS.2012.6473587.

[76] K. Ono, R. Ono, and Y. Hanada, “3D surface registration using estimated local shape variation,” *1st Annu. IEEE Conf. Control Technol. Appl. CCTA 2017*, vol. 2017-Janua, pp. 1362–1367, 2017, doi: 10.1109/CCTA.2017.8062648.

[77] Y. Fan, X. Xu, and M. Wang, “A surface-based spatial registration method based on sense three-dimensional scanner,” *J. Craniofac. Surg.*, vol. 28, no. 1, pp. 157–160, 2017, doi: 10.1097/SCS.0000000000003283.

[78] F. Meng, F. Zhai, B. Zeng, H. Ding, and G. Wang, “An automatic markerless registration method for neurosurgical robotics based on an optical camera,” *Int. J. Comput. Assist. Radiol. Surg.*, 2018, doi: 10.1007/s11548-017-1675-5.

[79] J. Rost, S. S. Harris, J. D. Stefansic, K. Sillay, and R. L. Galloway, Jr., “Comparison between skin-mounted fiducials and bone-implanted fiducials for image-guided

neurosurgery," *Med. Imaging 2004 Vis. Image-Guided Proced. Disp.*, vol. 5367, p. 766, 2004, doi: 10.1117/12.537768.

[80] C. R. Mascott, J. C. Sol, P. Bousquet, J. Lagarrigue, Y. Lazorthes, and V. Lauwers-Cances, "Quantification of true in vivo (application) accuracy in cranial image-guided surgery: Influence of mode of patient registration," *Neurosurgery*, vol. 59, no. 1 SUPPL. 1, pp. 146–156, 2006, doi: 10.1227/01.NEU.0000220089.39533.4E.

[81] D. Paraskevopoulos, A. Unterberg, R. Metzner, J. Dreyhaupt, G. Eggers, and C. R. Wirtz, "Comparative study of application accuracy of two frameless neuronavigation systems: Experimental error assessment quantifying registration methods and clinically influencing factors," *Neurosurg. Rev.*, vol. 34, no. 2, pp. 217–228, 2011, doi: 10.1007/s10143-010-0302-5.

[82] A. I. Kholyavin and V. B. Nizkovolos, "Precision Stereotactic Frameless Neuronavigation," *Biomed. Eng. (NY).*, vol. 50, no. 4, pp. 249–252, 2016, doi: 10.1007/s10527-016-9631-1.

[83] A. Salma, O. Makiese, S. Sammet, and M. Ammirati, "Effect of registration mode on neuronavigation precision: An exploration of the role of random error," *Comput. Aided Surg.*, vol. 17, no. 4, pp. 172–178, 2012, doi: 10.3109/10929088.2012.691992.

[84] G. R. Sutherland, P. B. McBeth, and D. F. Louw, "NeuroArm: An MR compatible robot for microsurgery," *Int. Congr. Ser.*, vol. 1256, no. C, pp. 504–508, 2003, doi: 10.1016/S0531-5131(03)00439-4.

[85] L. Liu *et al.*, "Frameless ROSA® Robot-Assisted Lead Implantation for Deep Brain Stimulation: Technique and Accuracy.," *Oper. Neurosurg. (Hagerstown, Md.)*, vol. 0, no. 0, pp. 1–8, 2019, doi: 10.1093/ons/opz320.

[86] N. J. Brandmeir, “The comparative accuracy of the ROSA stereotactic robot across a wide range of clinical applications and registration techniques,” *J. Robot. Surg.*, 2017, doi: 10.1007/s11701-017-0712-2.

[87] P. S. Morgan *et al.*, “The application accuracy of the Pathfinder neurosurgical robot,” *Int. Congr. Ser.*, vol. 1256, no. C, pp. 561–567, 2003, doi: 10.1016/S0531-5131(03)00421-7.

[88] G. Bhutani, “Modeling design and development of frameless stereotaxy in robot assisted neurosurgery,” HBNI, Mumbai, India, 2015.

[89] G. Bhutani, T. A. Dwarakanath, and D. N. Badodkar, “Modeling, Design, Identification of DH Parameters and Calibration of Surgical Coordinate Measuring Mechanism,” in *Machines, Mechanism and Robotics*, Springer, 2019, pp. 233–245.

[90] G. Bhutani, T. A. Dwarakanath, K. D. Lagoo, A. Moiyadi, and P. P. K. Venkata, “Neuro-registration and navigation unit for surgical manipulation,” in *Proceedings of the 1st International and 16th National Conference on Machines and Mechanisms (iNaCoMM2013)*, 2013, pp. 18–20.

[91] M. A. Liss and E. M. McDougall, “Robotic surgical simulation,” *Cancer J. (United States)*, vol. 19, no. 2, pp. 124–129, 2013, doi: 10.1097/PPO.0b013e3182885d79.

[92] A. Bernardo, “Virtual Reality and Simulation in Neurosurgical Training,” *World Neurosurg.*, vol. 106, pp. 1015–1029, 2017, doi: 10.1016/j.wneu.2017.06.140.

[93] M. I. P. H. Cobb, J. M. Taekman, A. R. Zomorodi, L. F. Gonzalez, and D. A. Turner, “Simulation in Neurosurgery—A Brief Review and Commentary,” *World Neurosurg.*, vol. 89, pp. 583–586, 2016, doi: 10.1016/j.wneu.2015.11.068.

[94] R. A. Robison, C. Y. Liu, and M. L. J. Apuzzo, “Man, mind, and machine: The past

and future of virtual reality simulation in neurologic surgery," *World Neurosurg.*, vol. 76, no. 5, pp. 419–430, 2011, doi: 10.1016/j.wneu.2011.07.008.

[95] T. Haidegger, T. Xia, and P. Kazanzides, "Accuracy improvement of a neurosurgical robot system," *Proc. 2nd Bienn. IEEE/RAS-EMBS Int. Conf. Biomed. Robot. Biomechatronics, BioRob 2008*, pp. 836–841, 2008, doi: 10.1109/BIOROB.2008.4762912.

[96] M. S. Eljamel, "Validation of the PathFinder neurosurgical robot using a phantom," no. August, pp. 372–377, 2007, doi: 10.1002/rcs.

[97] P. Eldridge, "Use of the NeuroMate stereotactic robot in a frameless mode for functional neurosurgery †," no. March, pp. 107–113, 2006, doi: 10.1002/rcs.

[98] G. Minchev *et al.*, "A novel miniature robotic guidance device for stereotactic neurosurgical interventions: preliminary experience with the iSYS1 robot," pp. 1–12, 2016, doi: 10.3171/2016.1.JNS152005.

[99] S. Eggener, "Edward Hospital." https://www.uchicagomedicine.org/forefront/surgery-articles/they-did-surgery-on-a-grape-and-we-did-a-q-and-a-with-a-surgeon-about-it (accessed Dec. 26, 2019).

[100] "Robotic Pumpkin Surgery." https://www.youtube.com/watch?v=mjbgd8U5Bec (accessed Dec. 26, 2019).

[101] W. Walz, *Experimental Neurosurgery in Animal Models Series Editor*. .

[102] L. Ramrath, S. Vogt, W. Jensen, U. G. Hofmann, and A. Schweikard, "Computer- and robot-assisted stereotaxy for high-precision small animal brain exploration / Computer- und robotergestützte Stereotaxie für hochpräzise Exploration des Kleintierhirns," *Biomed. Tech. Eng.*, vol. 54, no. 1, pp. 8–13, 2009, doi:

10.1515/bmt.2009.002.

[103] H. J. Marcus, A. Hughes-Hallett, T. P. Cundy, G. Z. Yang, A. Darzi, and D. Nandi, “da Vinci robot-assisted keyhole neurosurgery: a cadaver study on feasibility and safety,” *Neurosurg. Rev.*, vol. 38, no. 2, pp. 367–371, 2015, doi: 10.1007/s10143-014-0602-2.

[104] X. Du, P. N. Brett, P. Begg, A. Mitchell-innes, C. Coulson, and R. Irving, “A hand-guided robotic drill for cochleostomy on human cadavers,” pp. 13–18, 2018.

[105] M. H. Yoo, H. S. Lee, C. J. Yang, and S. H. Lee, “A Cadaver Study of Mastoidectomy Using an Image-Guided Human – Robot Collaborative Control System,” doi: 10.1002/lio2.111.

[106] R. Bertolo, J. Garisto, J. Dagenais, D. Sagalovich, and J. H. Kaouk, “Single Session of Robotic Human Cadaver Training: The Immediate Impact on Urology Residents in a Teaching Hospital,” *J. Laparoendosc. Adv. Surg. Tech.*, vol. 28, no. 10, pp. 1157–1162, 2018, doi: 10.1089/lap.2018.0109.

[107] G. Minchev *et al.*, “A novel miniature robotic guidance device for stereotactic neurosurgical interventions: Preliminary experience with the iSYS1 robot,” *J. Neurosurg.*, vol. 126, no. 3, pp. 985–996, 2017, doi: 10.3171/2016.1.JNS152005.

[108] G. Fattori *et al.*, “Automated fiducial localization in CT images based on surface processing and geometrical prior knowledge for radiotherapy applications,” *IEEE Trans. Biomed. Eng.*, 2012, doi: 10.1109/TBME.2012.2198822.

[109] M. Wang and Z. Song, “Automatic localization of the center of fiducial markers in 3D CT/MRI images for image-guided neurosurgery,” *Pattern Recognit. Lett.*, 2009, doi: 10.1016/j.patrec.2008.11.001.

[110] F. Cardinale *et al.*, "A new tool for touch-free patient registration for robot-assisted intracranial surgery: application accuracy from a phantom study and a retrospective surgical series," *Neurosurg. Focus*, vol. 42, no. 5, p. E8, 2017, doi: 10.3171/2017.2.FOCUS16539.

[111] M. Wang and Z. Song, "Automatic localization of the center of fiducial markers in 3D CT/MRI images for image-guided neurosurgery," *Pattern Recognit. Lett.*, vol. 30, no. 4, pp. 414–420, 2009, doi: 10.1016/j.patrec.2008.11.001.

[112] G. Fattori *et al.*, "Automated fiducial localization in CT images based on surface processing and geometrical prior knowledge for radiotherapy applications," *IEEE Trans. Biomed. Eng.*, vol. 59, no. 8, pp. 2191–2199, 2012, doi: 10.1109/TBME.2012.2198822.

[113] F. Suligoj, M. Svaco, B. Jerbic, B. Sekoranja, and J. Vidakovic, "Automated Marker Localization in the Planning Phase of Robotic Neurosurgery," *IEEE Access*, 2017, doi: 10.1109/ACCESS.2017.2718621.

[114] U. Spetzger, G. Laborde, and J. M. Gilsbach, "Frameless neuronavigation in modern neurosurgery," *Minim. Invasive Neurosurg.*, vol. 38, no. 4, pp. 163–166, 1995, doi: 10.1055/s-2008-1053478.

[115] D. A. Orringer, A. Golby, and F. Jolesz, "Neuronavigation in the surgical management of brain tumors: Current and future trends," *Expert Rev. Med. Devices*, vol. 9, no. 5, pp. 491–500, 2012, doi: 10.1586/erd.12.42.

[116] J. M. Fitzpatrick, "The role of registration in accurate surgical guidance," *Proc. Inst. Mech. Eng. Part H J. Eng. Med.*, vol. 224, no. 5, pp. 607–622, Sep. 2009, doi: 10.1243/09544119JEIM589.

[117] I. Rozet and M. S. Vavilala, “Risks and Benefits of Patient Positioning During Neurosurgical Care,” *Anesthesiol. Clin.*, vol. 25, no. 3, pp. 631–653, 2007, doi: 10.1016/j.anclin.2007.05.009.

[118] M. Kawaguchi, “Essentials of Neurosurgical Anesthesia & Critical Care,” pp. 283–287, 2012, doi: 10.1007/978-0-387-09562-2.

[119] Z. A. Hartley R, *Multiple view geometry*. Cambridge, 2004.

[120] opencv dev team, “Camera calibration With OpenCV — OpenCV 2.4.13.6 documentation.” https://docs.opencv.org/2.4/doc/tutorials/calib3d/camera_calibration/camera_calibration.html#theory (accessed Mar. 19, 2018).

[121] Alexander Mordvintsev & Abid K, “Pose Estimation — OpenCV-Python Tutorials 1 documentation,” *OpenCV*, 2013. http://opencv-python-tutroals.readthedocs.io/en/latest/py_tutorials/py_calib3d/py_pose/py_pose.html (accessed Mar. 19, 2018).

[122] A. Kaushik, T. A. Dwarakanath, and G. Bhutani, “Autonomous neuro-registration for robot-based neurosurgery,” *International Journal of Computer Assisted Radiology and Surgery*, 2018.

[123] E. C. S. Chen, B. Ma, and T. M. Peters, “Contact-less stylus for surgical navigation: registration without digitization,” *Int. J. Comput. Assist. Radiol. Surg.*, vol. 12, no. 7, pp. 1231–1241, 2017, doi: 10.1007/s11548-017-1576-7.

[124] G. Taguchi and S. Konishi, *Taguchi Methods: Signal-To-Noise Ratio for Quality Evaluation*. American Supplier Institute, 1991.

[125] A. Pagani, J. Koehler, and D. Stricker, “Circular markers for camera pose estimation,”

WIAMIS 2011 12th Int. Work. Image Anal. Multimed. Interact. Serv., no. January 2011, 2011, [Online]. Available: https://repository.tudelft.nl/islandora/object/uuid:6b009c1c-e00d-4f0d-94c6-07925bd162bc?collection=research.

[126] Minitab Software, “Minitab Software.” www.minitab.com (accessed Sep. 17, 2019).

[127] R. C. Team, “R: A language and environment for statistical computing,” 2013.

[128] J. M. M. Pérez and J. Pascau, *Image Processing with ImageJ*. Packt Publishing, 2013.

[129] J. B. West *et al.*, “Fiducial Point Placement and the Accuracy of Point-based, Rigid Body Registration,” vol. 48, no. 4, pp. 1–8, 2015, [Online]. Available: papers3://publication/uuid/3F18169E-3AAD-4AD5-A5F2-9DFE1761340D.

[130] Dabur, “Pudin-Hara tablet.” https://www.dabur.com/in/en-us/ayurvedic-herbal-products/pudin-hara (accessed Jun. 07, 2019).

[131] A. Jahanbakhshi, Y. Abbaspour-Gilandeh, and T. M. Gundoshmian, “Determination of physical and mechanical properties of carrot in order to reduce waste during harvesting and post-harvesting,” *Food Sci. Nutr.*, vol. 6, no. 7, pp. 1898–1903, 2018, doi: 10.1002/fsn3.760.

[132] F. Sepehrband *et al.*, “Brain tissue compartment density estimated using diffusion-weighted MRI yields tissue parameters consistent with histology,” *Hum. Brain Mapp.*, vol. 36, no. 9, pp. 3687–3702, 2015, doi: 10.1002/hbm.22872.

[133] T. E. D. W. Barber and A. Brockway, “T H E DENSITY OF TISSUES IN AND ABOUT THE HEAD Knowledge of the density of a material is basic to formulation of a model of response of a structure to impact loading . If the human head response to acceleration is to be predicted , the density of tissues,” pp. 85–92, 1970.

[134] S. K. JLN Sastry, SD Pandey, Anurag Vats, Sasibhushan Vedula, “Symptomatic management of functional dyspepsia: evaluation of efficacy and safety of pudin hara pearls and pudin hara liquid,” pp. 1–5, 2016, doi: 10.7897/2277-4343.073114.